Manufacturing and Design Validation of New Stent Grafts That Contain Complex Geometries

by

Moataz Mohsen Ahmed Elsisy

Bachelors of Mechanical Design Engineering, Cairo University, 2012

Masters of Mechanical Design Engineering, Cairo University, 2016

Submitted to the Graduate Faculty of the

Swanson School of Engineering in partial fulfillment

of the requirements for the degree of

Doctor of Philosophy

University of Pittsburgh

2021

UNIVERSITY OF PITTSBURGH

SWANSON SCHOOL OF ENGINEERING

This thesis was presented

by

Moataz Mohsen Ahmed Elsisy

It was defended on

October 26, 2021

and approved by

Youngjae Chun, Ph.D, Associate Professor, Department of Industrial Engineering

Paul Leu, Ph.D, Associate Professor, Department of Industrial Engineering

Bopaya Bidanda, Ph.D, Professor, Department of Industrial Engineering

Bryan W. Tillman, MD, Ph.D, Associate Professor, Department of the Ohio State College of Medicine

Dissertation Director: Youngjae Chun, Ph.D, Associate Professor, Department of Industrial Engineering

Manufacturing and Design Validation of New Stent Grafts That Contain Complex Geometries

Moataz Mohsen Ahmed Elsisy

University of Pittsburgh, 2021

Both shape memory alloy and superelastic properties of Nitinol material have attracted substantial attention in a wide range of medical applications. A low-energy Nd:YAG laser joining technique shows a high potential to create large diameter Nitinol endovascular devices that contain complex geometry, because of its versatility and controllability to produce complex geometry. The purpose of this thesis is to investigate the effects of laser joining process parameters regarding the mechanical performance of Nitinol stents. Two new endovascular devices have been fabricated using the optimized laser joining process, which have demonstrated successful device delivery and retrieval

The first device is addressing traumatic vascular injuries which require new endovascular devices to rapidly control the excessive internal hemorrhage in the torso. A retrievable stent graft could regulate the internal bleeding temporarily, as fast as possible with the most feasible performance. The stent graft is manufactured using a substantially long Nitinol backbone and covered selectively based on anatomic measurements, with expandable polytetrafluoroethylene (ePTFE). In this study, designing and manufacturing methods were explored, and their impact on the stent graft performance. Geometric and heat treatment parameters were investigated to show their effect on the radial force of the backbone. The resistance force for retrieval and deployment were measured, and analyzed to be manipulated through ePTFE covering. In vitro measurements for bleeding were measured using swine aorta to show the functionality of the stent graft. Finally,

the stent graft showed substantial effectiveness for hemorrhage control in vivo, using a swine model.

The second device is a novel stent graft for abdominal organ perfusion with cardiac flow isolation. In this thesis, the effectiveness of the device design has been validated via the assessment of the device performance. The radial force of stent structure was first numerically analyzed using finite element method, then was quantified experimentally. The blood perfusion parameters were investigated to demonstrate their effect on the blood delivered to the abdominal organs, maintaining the organs healthy for donation. In vivo porcine test results have demonstrated smooth delivery and successful placement of the device showing cardiac flow separation with sufficient strength of Nitinol backbone.

Table of Contents

Preface xix

1.0 Background 1

1.1 History of Nitinol 1

1.2 Nitinol Properties and Behavior 2

1.2.1 Shape Memory Effect 2

1.2.2 Superelasticity 3

1.2.3 Surface Properties 5

1.2.4 Hemocompatibility 5

1.3 Manufacturing Processes Used In Nitinol Endovascular Devices 6

1.3.1 Drawing Process for Nitinol Wires and Tubes 6

1.3.2 Laser-Cutting Process for Stent Fabrication 8

1.3.3 Joining and Welding Processes for Nitinol 8

1.3.4 Thermal Annealing 9

1.3.5 Electropolishing 10

1.4 Examples of Nitinol Endovascular Devices 10

1.4.1 Stent Grafts 10

1.4.2 Percutaneous Heart Valve Frame 12

1.4.3 Vena Cava Filter 14

1.4.4 Atrial Septal Defect (ASD) Occluder 15

2.0 Research Scope and Objectives 17

3.0 Manufacturing Process Optimization of Laser Welding Joints 20

3.1 Introduction 20

3.2 Materials and Methods 22

3.2.1 Preparation of Micro Laser-Welded Nitinol Joint Samples 22

3.2.2 Evaluation on Disconnecting Force of Nitinol Joints.....22

3.3 Results..... 24

3.3.1 Laser Welding Joints 24

3.3.2 Disconnecting Force of Nitinol Joints.....25

3.4 Discussion 28

3.5 Conclusion 30

4.0 Mechanical Property Assessment of Long Stent Graft to Control Hemorrhage in Torso..... 31

4.1 Introduction 31

4.2 Methods and Results 36

4.2.1 In Vitro Radial Force Measurement of Nitinol Backbone 36

4.2.2 Assessment of Thermal Annealing Effect. 40

4.2.3 In Vitro Device Deployment and Retrieval Tests for Evaluating Resistance.....43

4.2.4 In Vitro Leakage Test for Different Type of Stent grafts.....49

4.3 Trauma stent graft development..... 52

4.3.1 Materials 52

4.3.2 Stent Graft Fabrication Processes 53

4.3.2.1 Nosecone Configuration Optimization 54

4.3.2.2 Polymeric Ends Fixation 56

4.3.2.3 A Manufactured Prototype 57

4.4 In Vivo Tests 59

4.5 Discussion 62

4.6 Conclusion 66

5.0 Design Validation of a Novel Organ Perfusion Stent (OPS) 67

5.1 Introduction 67

5.2 Methods and Results 70

5.2.1 Radial force measurement 70

5.2.1.1 Computational modeling of the radial force via finite element analysis (FEA) 70

5.2.1.2 Measurement of the radial force 74

5.2.2 In vitro flow dynamics study 76

5.2.2.1 Effect of perfusion length on cardiac flow rate 78

5.2.2.2 Flow rate measurements of perfusion to the abdominal organs 79

5.2.2.3 Leakage of perfusion fluid to the cardiac flow 82

5.3 Device Development 83

5.3.1 First Prototype 84

5.3.2 Second Prototype 85

5.3.3 Final Prototype 86

5.4 In Vivo Test 87

5.5 Discussion 89

5.6 Conclusion 93

6.0 Scientific Contributions 94

7.0 Conclusions 98

Bibliography 101

List of Tables

Table 1 Summary of laser parameters used for disconnecting force study 24

Table 2 Summary of outcomes of the research conducted..... 92

List of Figures

Figure 1 Single Crystal model of deformation of Nitinol. A) Shape memory effects are exploited by temperature change. The material can recover its shape by heating above Austenite finish temperature. B) Superelastic effects occur in two ways transformations in the Austenite phase only. 3

Figure 2 Stress-Strain response of Nitinol. A) Comparison between Nitinol and steel. Nitinol shows hysteresis effect between loading and unloading. B) Loading and unloading of Nitinol and living tissues. Nitinol demonstrates similar trend with the living tissues 4

Figure 3 Schematic illustration for drawing of Nitinol superelastic wire for continuous production..... 7

Figure 4 A) Innova™ Stent Delivery System (Boston Scientific). B) VIABAHN® Endoprosthesis (Gore Medical) 12

Figure 5 A) CoreValve ReValving System profile [43]. B) In situ Coronal MRI image CoreValve prosthesis, after six months' implantation [40]. C) Fluoroscopic guidance for implanting the CoreValve prosthesis [40]. 13

Figure 6 A) Abdominal plain film. The Simon Nitinol filter is well positioned in the inferior vena cava [58]. B) Optease vena cava filter (Cordis) [59]. C) Denali vena cava filter (Bard) [59]..... 15

Figure 7 A) Amplatzer septal occluder made of two round disks from 0.005-in. Nitinol wire, that tightly woven into with a 4-mm connecting waist (arrowheads)[63]. B) Adaptor tube (arrowheads) used for the occluder delivery. [63]. C) Mechanisms of leakage-proof closure with the two retention discs, which are angled inward. The left atrial

retention disc slightly bigger than the right, to ensure over-fitted clamping against around the defect [60]. D) Good positioning and complete closure of the Amplatzer, are shown using Levo-phase of pulmonary arteriogram [63]..... 16

Figure 8 Experimental setup for disconnecting force measurement of the laser-welding joints. A-D) are the progress of the applying force on the joints, beginning at A) with no force, up to C) which shows the detachment of the two wires. Figure E) shows how the disconnecting force is measured as the difference between the force at test start and the force on disconnecting time. 23

Figure 9 SEM images for laser welded spots between two parallel Nitinol wires. A) One spot. B) Two spots. C) Three spots. 25

Figure 10 Effect of laser parameters on disconnecting force of the laser-welded joint. A) Disconnecting force for several laser powers, 0.6, 0.8, 0.9, and 1kW. B) Disconnecting force for different laser frequencies, 1, 8, and 15Hz. C) Disconnecting force for different laser spot sizes, 0.3, 0.4, and 0.6mm. 26

Figure 11 Effect of laser joint configuration on disconnecting force of the laser-welded joint. Disconnecting force for several wire diameters, 0.3, 0.35, 0.4, and 0.45mm. 27

Figure 12 A) Disconnecting force for one-, two-, three-, and four- laser spots welding joints B) Disconnecting force for zero-, one-, two-, and three-, laser spots on the back of welding joints, while having 3-spots in the front side of the joint. 28

Figure 13 Schematic of the incompressible injury of the aorta artery. (A) The Aortic injury, causing the patient to bleed to death. (B) Using the novel stent graft, the blood flow is controlled inside the aorta artery, supplying blood to the organs in the abdominal region..... 33

Figure 14 A) Mechanical setup for radial force using mechanical testing system by pulling Dacron strap surrounding the stent. B) Stents with different distances between two consecutive welds, 17 mm, 23 mm, and 30 mm. C) Stents with different deployed diameters, 15 mm, 20 mm and 25 mm. 37

Figure 15 Radial force measurements for different geometric parameters. A) Radial force for several wire diameters, 0.012", 0.014", 0.015" and 0.0175" with respect to diameter reduction %. B) Radial force for different welding distances, 17 mm, 23 mm, and 30 mm with respect to diameter reduction%. C) Radial force for stents with different deployed diameters, 15 mm, 20 mm, and 25 mm with respect to diameter reduction %. 39

Figure 16 Radial force measurements for stents with different heat treatment conditions. A) Radial force for different annealing temperatures, 450 °C, 500 °C, and 600 °C with respect to diameter reduction%. B) Radial force for several annealing time, 10 min, 15 min, 20 min, 25 min, and 30 min with respect to diameter reduction %. C) Radial force for different number of annealing cycles with respect to diameter reduction %. 42

Figure 17 A) Experimental setup for resistance force measurement during deployment and capturing the stent graft in different sheaths. B) Different configurations of ePTFE with respect to the metallic backbone, bare, internal, and external. 44

Figure 18 Resistance force for retrieval and deployment of the stent graft in the sheath. A) & B) are graphs that represent the retrieval and deployment resistive forces versus the stent graft length of bare stent in 8 Fr., 9 Fr., and 10 Fr. sheaths. 45

Figure 19 Resistance force for retrieval and deployment of the stent graft in the sheath. A) & C) are graphs that represent the retrieval and deployment resistive forces versus the stent graft length of internally attached ePTFE stent grafts in 9 Fr., and 10 Fr. sheaths. B) & D) are graphs that represent the retrieval and deployment resistive forces versus the stent graft length of externally attached ePTFE stent grafts in 9 Fr., and 10 Fr. sheaths. 46

Figure 20 Resistance force for retrieval and deployment of stent graft on 9 Fr. sheath. A) & B) are the resistance forces versus stent length for stent grafts with different configurations of ePTFE, bare, internal, and external. C) Resistance force versus stent graft length for different capturing speeds, 250, 500, and 750 mm/min..... 48

Figure 21 A) Experimental setup for leakage quantification between stent graft and swine aorta. The setup consists of a pulsatile pump, water bath and a tank of glycerin-water solution. Pressure sensor is attached to measure the solution pressure and recorded by pressure transducer. B) Close look for the swine aorta. C) An image for the stent graft deployed inside the swine aorta. 50

Figure 22 leakage measurement for swine aorta using different pressures and flow rates for uncontrolled, 20 mm, and 25 mm. A) Leakage measurements for different pressures, 85, 72.5, 60, and 52.5 mmHg with flow rate 2500 cc/min. B) leakage measurements for different flow rates, 900, 1200, and 1500 cc/min with pressure 25 mmHg. 51

Figure 23 Qualitative representation of the leakage in the tubes with different diameter, which shows a 15mm stent graft provides seal of (A) an 8mm hole against pulsatile flow, (B) 75% of the stent graft, and (C) even 50% smaller. 52

Figure 24 The first prototypes of nosecone attachment to the stent graft. (A) Image shows the 1st and 2nd prototypes of the nosecone attachment, either by extending the Nitinol wires, or welding extra Nitinol wires to the upper section. (B) Stent graft prototype using the 2nd prototype method of attaching the nosecone. (C) Post surgery image of the upper section of the stent graft, including the nosecone. The backbone diameter is shrank from the top and the ePTFE is separated. 55

Figure 25 The new prototype for the upper section of the stent graft and nosecone. (A) The stent backbone after removing the upper bends. (B) The nosecone is connected to the stent graft via a Nitinol wire, welded to the lower section of the stent graft. 56

Figure 26 Images show the new fixations of the inside-ePTFE to the metallic backbone. Small pieces of thin ePTFE layer are glued to both the Nitinol structure, as well as the ePTFE cover. (A) The fixation of the start of thoracic covering. (B) The fixation of the end of thoracic covering. 57

Figure 27 A prototype that contains a nosecone, two PTFE covered regions, bare metal region for perfusion and an extension wire for easy delivery and retrieval process. 58

Figure 28 In vivo images to a swine subject for hemorrhage control using the stent graft. A) An image shows the hemorrhage, occurred in the thoracic region of the aorta artery. B) An image shows the hemorrhage control using the stent graft. 60

Figure 29 (A) Gross image of the stent graft deployed inside an injured artery. (B) The stent graft after the surgery, showing the laser welded joints, without any fracture, also, ePTFE is still fixed to the metallic backbone..... 61

Figure 30 Schematic drawing showing the functionality of OPS inside the aorta artery. (A) Schematic shows the low oxygen flow to the main arteries in the abdominal region,

causing ischemic injury. (B) OPS is deployed inside the aorta artery, to isolate the abdominal arteries from the cardiac flow, and divide the artery into 2 zones. (C) A perfusion conduit is connected to zone 1, which is connected to an external source of oxygenated blood, to deliver the necessary blood supply to the organs..... 69

Figure 31 Finite element analysis of radial force of metallic backbone. A) Stent CAD, showing the diamond shape of the stent. B) The boundary conditions applied to the stent. The stent is fixed from the bottom, and pressure is applied to the center of the stent. C) Table mentions the values of parameters used in the simulation. D) The stress-strain response of superelastic Nitinol. 72

Figure 32 Computational results for finite element model. A) The radial force versus diameter reduction % for different stent lengths. B) The maximum Von-Mises stress versus diameter reduction % for different stent lengths. C-F) are the pictures of stent deformation when a local pressure is applied on the middle of the stent, for 5, 7.5, 10, and 12.5 cm. 73

Figure 33 Experimental measurements of radial force of the Nitinol backbones. A) Stents with different lengths of the upper seal, perfusion length, and lower seal. B) Upper seal with four different lengths, 5, 7.5, 10, and 12.5 cm. C) Lower seal with four different lengths 2.5, 5, 7.5, and 10 cm. D) An image for the experimental setup of the testing machine for radial force measurements. E) & F) Dacron tape used to apply radial force on the upper and lower seal, respectively. 75

Figure 34 Experimental results of the radial force. A) The radial force versus diameter reduction % for upper seal. B) The radial force versus diameter reduction % for lower seal..... 76

Figure 35 Schematic drawing for the experimental setup for flow rate measurements. The Aortic model used for in vitro flow rate measurements. The flow is injected from the left using a pulsatile pump. The model has six outputs, SMA, two renal arteries, and two iliac arteries. 78

Figure 36 Cardiac flow effect after inserting the OPS inside the aorta model. A) Cardiac flow rate without OPS. B) Cardiac flow rate after OPS placement with different perfusion lengths. 79

Figure 37 Effect of perfusion sheath on the perfusion flow rate to the abdominal organs. A) Flow rate through abdominal arteries for different perfusion sheath sizes. B) Flow rate through abdominal arteries for different lengths of perfusion sheath..... 81

Figure 38 Effect of perfusion region parameters on the perfusion flow rate to the abdominal organs. A) Flow rate through abdominal arteries for different perfusion length. B) Flow rate through abdominal arteries for different locations of perfusion output. . 82

Figure 39 Leakage flow rate from the perfusion region to cardiac region. A) Leakage flow rate versus different sealing length for different perfusion flow rates. B) Effect of the sealing length on leakage flow rate for 800 (ml/min) perfusion flow rate. 83

Figure 40 First prototype of dual chamber. (A) Using laser-welding, Nitinol wires were used to fabricate stent, with dual chambers in the middle. (B) Metallic rods used to show the lumens inside the stent. One lumen exists at both upper and lower sections of the stent, but two lumens in the middle section. (C) Magnified image to the middle regions, showing separated lumens. 85

Figure 41 Second prototype of organ perfusion stent. (A) The metallic backbone is depicted with a welded tapered tube, for perfusion sheath docking. (B) The stent graft is covered with ePTFE, ready for in-vivo experiment..... 86

Figure 42 (A) Schematic drawing showing the functionality of OPS inside the aorta artery, (A) fully deployed device showing three sections with a nosecone and extension wire, (B) collapsed device into a 10Fr delivery sheath, and (C) magnified perfusion region. 87

Figure 43 (A) Baseline angiography of a branched segment of aorta. Following placement of the dual chamber stent, the center lumen excludes the branches (B), whereas the outer chamber (C) isolates perfusion of the branches from a perfusion lumen extending outside the body (Arrowhead). 88

Preface

I will like to express my sincere appreciation to my wife, Ayat, who gave me the hope, when I was down.

1.0 Background

1.1 History of Nitinol

Shape memory behavior was first discovered in gold–cadmium (AuCd) alloy by Dr. Olander in 1932. The deformed AuCd alloy material in low temperature regains its original shape with the applied heat [1]. Many other alloys, such as CrMn, FePt, BaTiO, and CuMn, were synthesized to achieve similar phase transformation behavior [2]. By the late 1950s at the US Naval Ordnance Laboratory, Buehler and his colleagues discovered the shape memory behavior in nickel–titanium (NiTi) alloy while they worked on intermetallic compounds for heat shielding of missiles [2–4]. Nitinol is referred to as NiTi in Ordnance Laboratory and became popular in various fields including aerospace, medical, and other industries due to its inexpensive cost for manufacturing and reliable performance. Nitinol has another unique property, superelasticity, in addition to shape memory behavior. Kurdiumov discovered superelastic behavior of metallic alloys in 1948 by investigating the elastic response of alloys that exhibit phase transformation upon varied stress levels applied on materials [5].

Currently available commercial products include buckling-resistant antennas, pipe-coupling devices, and eyeglass frames, which utilize superelastic behavior of Nitinol [6]. There are more advanced types of applications that use shape memory behavior, which include light structure and engine rotors for aircrafts, biomedical robots, and micro-actuators. More recently, Nitinol has been widely used in various medical applications. Dr. Andreasen has developed the first Nitinol biomedical application for an orthodontic device utilizing the superelastic behavior of Nitinol. Other applications include implantable medical devices, such as endovascular and

orthopedic devices [7–9]. Nitinol is specifically beneficial in transcatheter-based devices such as stents, percutaneous heart valves, and vascular occluders, and filters since these devices can be easily collapsed and inserted to a small diameter delivery catheter in low temperature, then deployed to its original shape and dimension in body temperature showing superelastic property after the device delivery.

1.2 Nitinol Properties and Behavior

1.2.1 Shape Memory Effect

Shape memory effect (SME) is the capability of the material, upon heating, to recover the permanent strain that occurs from the deformation in the martensitic phase [2]. Nitinol has a transformation (Tf) temperature between two different phases, austenite (i.e., above Tf) and martensite (i.e., below Tf). Each phase has a different crystal structure that provides the material either to have shape memory effect and superelasticity. The transformation of this alloy could be altered via manipulation of compositional variation of Ni and Ti followed by heat treatment. When the material is below the transformation temperature (i.e., martensite finish temperature, Mf), it deforms easily with the capability of reaching a high level of strains, martensite phase. When the temperature is above the transformation temperature (i.e., austenite finish temperature, Af), the material exhibits superelastic behavior, austenite phase. Since the temperature is the main parameter for the phase transformation, it is sometimes called thermomechanical transformation. The schematic of phase transformation for the materials is shown in Figure 1. When the material

is deformed in martensitic phase, it could recover its deformation through heating to reach the austenite phase as shown in Figure 1A [5].

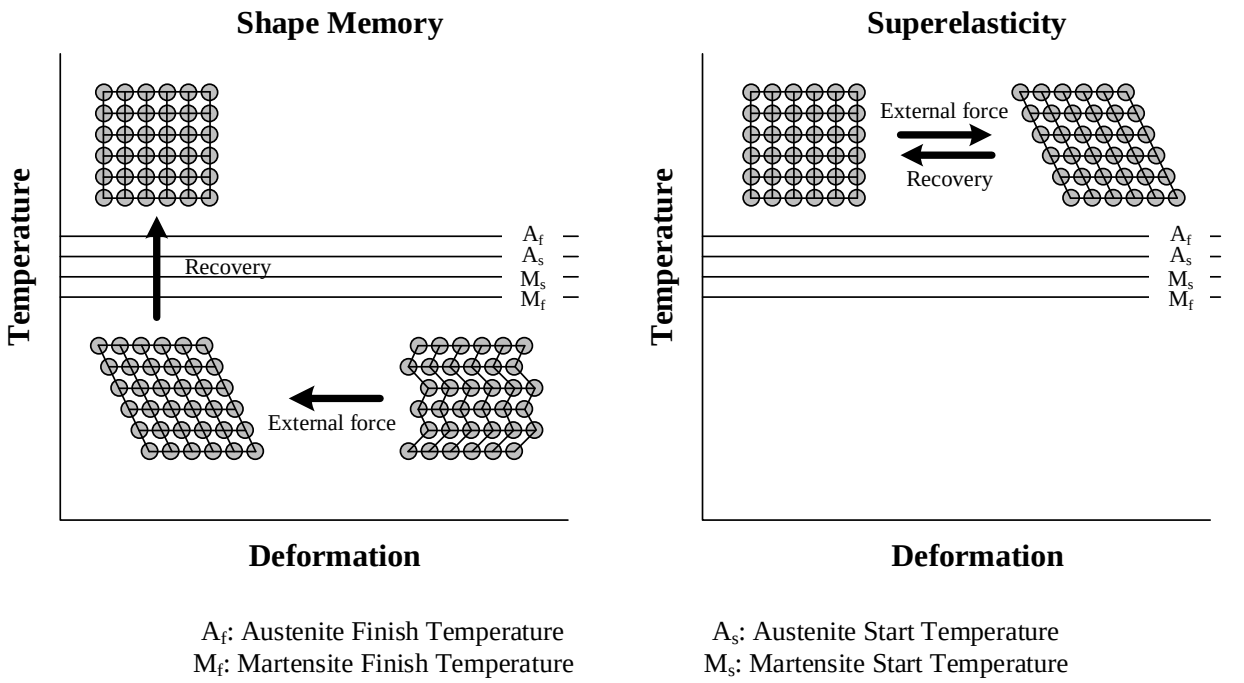

Figure 1 Single Crystal model of deformation of Nitinol. A) Shape memory effects are exploited by temperature change. The material can recover its shape by heating above Austenite finish temperature. B) Superelastic effects occur in two ways transformations in the Austenite phase only.

1.2.2 Superelasticity

Elasticity is the capability of recovering from the deformation when the load is removed without generating plastic deformation, like the spring effect. Superelastic material is regarded as a very efficient spring. Nitinol compositions can be manipulated in order to attain specific transformation temperatures between phases. Superelasticity happens only to Nitinol, when the material temperature lies above the austenite transformation threshold level as shown in Figure

1B. Nitinol gains relatively high merits over other traditional metals due to the stress-strain response, where Nitinol could reach high levels of strains with fracture. Nitinol's superelasticity could exceed the elastic limit of 10%; however, steel and copper fail to precede the elastic limit of 0.5% and 0.1%, respectively [8]. The stress-strain relation of Nitinol, compared to steel, is shown in Figure 2A. Another advantage of Nitinol for the biomedical application is the exhibition of a similar response trend upon loading and unloading to biological tissues for their deformation as shown in Figure 2B. This phenomenon is called pseudoelasticity, where the material can have a plateau upon large deflections through loading, or recovered deformations through unloading, without noticeable change during loading.

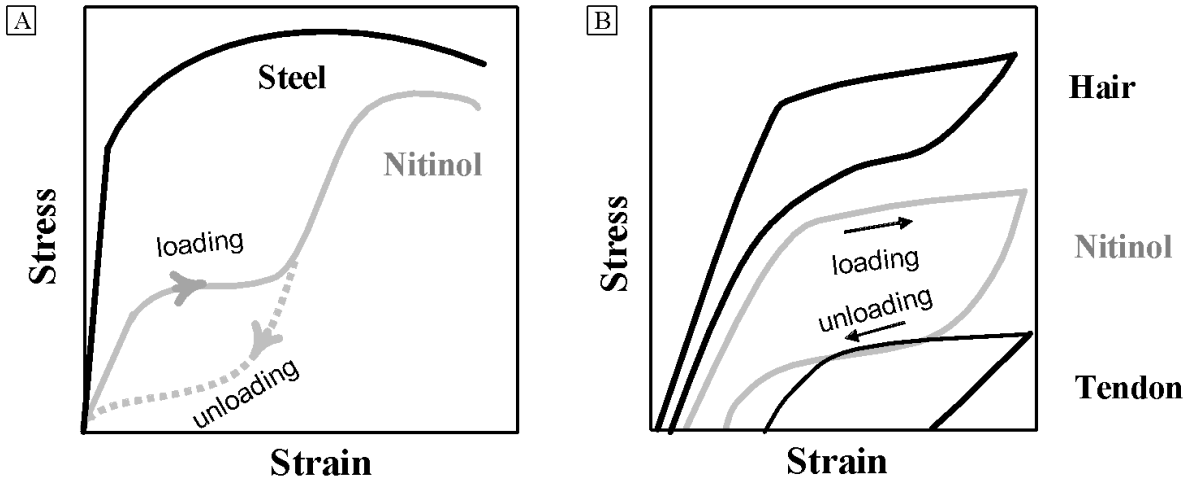

Figure 2 Stress-Strain response of Nitinol. A) Comparison between Nitinol and steel. Nitinol shows hysteresis effect between loading and unloading. B) Loading and unloading of Nitinol and living tissues. Nitinol demonstrates similar trend with the living tissues

1.2.3 Surface Properties

Biological response of the living organisms to the materials governs the material ability to be implanted in the body. Surface conditions such as roughness and chemical composition Nitinol endovascular devices have significant influence on the biological response. Higher roughness tends to decrease the hydrophilicity of the surface, which increases protein adsorption (contaminations on the surface) that occurs on the hydrophobic surfaces [10, 11]. Manufacturing processes, such as electropolishing, reduces the roughness of the Nitinol surface to minimize the protein adsorption. Also, the chemical composition of the surface can cause inflammatory response due to nickel allergy, upon being implanted inside the body. When Nitinol's surface is exposed to the atmosphere or various surface treatments, thin titanium oxide layer is generated, keeping nickel beneath the oxide layer [12]. Most metals including Nitinol have high surface energy, which exhibit hydrophilicity. Hydrophilic surface could decrease the protein adsorption during the implantation.

1.2.4 Hemocompatibility

Endovascular device's surface should be compatible with blood to minimize thrombosis formation on the device. Nitinol typically shows minimal thrombogenic response, similar to the excellent hemocompatible metallic biomaterials (e.g., stainless steel and titanium) [13, 14]. Nitinol devices that are placed in the blood vessel for a long time have demonstrated better performance of hemocompatibility by minimum protein adsorption, least possible of platelets adhesion, or blood clot formation on the implanted devices. Numerous surface modification strategies including

surface coatings, heat treatment, chemical treatment, and electropolishing have been investigated to improve the hemocompatibility in Nitinol surface [15, 16].

1.3 Manufacturing Processes Used In Nitinol Endovascular Devices

Along with the growth of Nitinol usage in biomedical devices, manufacturing processes have been developed to produce high-quality Nitinol alloy because the composition of nickel and titanium is critical for determining the property of Nitinol. The ratio between the two metals is typically 50:50%, and any change in this ratio alters the shape memory and superelastic properties. Any change in nickel or titanium percentage, even by 1%, could shift the transformation temperature with 100 °C [17, 18]. Higher amount of nickel modifies the properties of Nitinol to be more superelastic at lower temperatures. Various manufacturing processes and the produced material properties are described in this section, since the manufacturing processes affect the material percentage that determines the Nitinol's property.

1.3.1 Drawing Process for Nitinol Wires and Tubes

Continuous production of Nitinol wires using the strain annealing ensures the homogeneity of thermomechanical properties of the whole product. Figure 3 shows the schematic of continuous production of Nitinol wires. The main parts are (1) load control unit that regulates the tension during the drawing process, (2) furnace that controls the drawing temperature, and (3) speed control pulley that manipulates the drawing speed. Mechanical properties, final austenite temperature, and straightness are manipulated by temperature, tension, and speed in the drawing

process [18]. The drawing is performed under a stress of 35–100 MPa with a temperature range of 450 °C–550 °C.

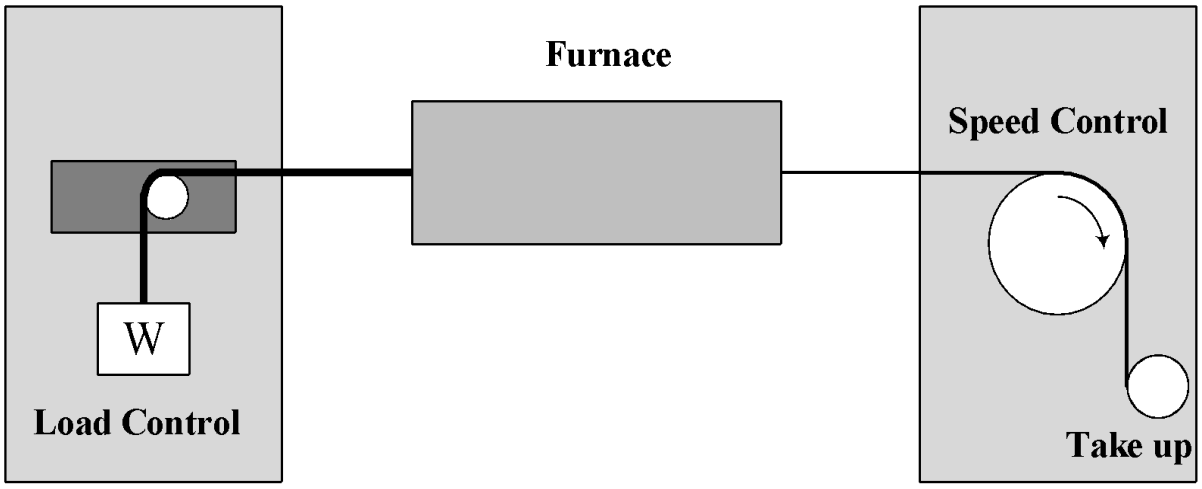

Figure 3 Schematic illustration for drawing of Nitinol superelastic wire for continuous production.

Nitinol wires undergo several steps through the drawing process. Raw material should have 50.5%–51.0% of nickel to produce superelastic wires. Nonmetallic inclusions, micro- and macro-segregations should be avoided before the drawing process [18]. Pre-annealing is performed to form thin oxide layer to work as lubricant through the process; however, if the oxide layer becomes too thick, it will cause cracks in the wire surface [19]. An alternative to the oxide layer as a lubricant is molybdenum disulfide, which shows a good lubrication performance in the Nitinol drawing process [19]. The drawing is performed using multi-passes in inert gas medium through monocrystalline dies. The final pass in drawing is the most important step to produce the desired dimensions and specific superelastic properties. Finally, any lubricant residue is eliminated from the drawn Nitinol wire.

1.3.2 Laser-Cutting Process for Stent Fabrication

Laser cutting is a process of applying a high-intensity light beam that swiftly heats the targeted area, which melts or/and vaporizes the material through its thickness. Palmaz-Schatz stent was the first approved stent for use in the United States in 1994, which was fabricated using a laser cutting process [20]. Laser cutting offers a couple of advantages over other manufacturing processes, including reliable dimensional accuracy, very small resolution, ease of automation, higher productivity, cut capability for most materials, and suitable for complex structures. Nitinol laser cutting can be exploited using continuous wave and pulsed wave using different processes including Nd: YAG laser [21], fiber laser [22, 23], and ultrashort pulse laser [24]. The primary laser cutting parameters are cutting speed, laser power, pulse type–duration, and gas (oxygen, inert gas, or air). The main objective of choosing the laser machine and its parameters is to achieve good surface quality with high dimensional accuracy, as well as minimum heat-affected zone that typically causes brittleness of Nitinol surface, in addition to lesser consistent kerf width (distance between cut slot edges). The early laser-cut stents were fabricated using Nd: YAG laser; however, low efficiency and lifetime affect the kerf width consistency [25]. Recently, fiber laser and short-pulsed laser are commonly used for manufacturing the stent due to their reliability, efficiency, and long lifetime.

1.3.3 Joining and Welding Processes for Nitinol

Joining and welding processes of Nitinol were recently investigated to overcome the drawbacks from laser cutting of the devices. The main problem from the laser cutting is the formation of a wide heat-affected zone (relatively to joining process) that alters the microstructure

and mechanical properties in Nitinol. To minimize the heat-affected zone, wire-to-wire joining was proposed to fabricate the devices. In addition, the laser cutting process is limited by the dimensions of the tube to be cut in order to fabricate the device, and laser or other types of welding could be one of the best options for the devices that have dimensions exceeding the limits of the fabrication of Nitinol tube. Laser-cut process used in stent fabrication typically removes more than 90% of materials, increasing the manufacturing cost, especially for larger devices. Nitinol-to-Nitinol laser welding can be performed using Nd: YAG laser [26, 27], CO2 laser [28], and tungsten inert gas welding [29]. Thermomechanical properties are usually maintained after the welding process. Nd: YAG laser welding preserves up to 75% of tensile strength of Nitinol as well as 7% deformation for the superelastic welded parts [30]. Welding Nitinol to dissimilar metal is quite challenging due to the formation of the brittle intermetallic compounds; however, Nitinol was successfully welded to stainless steel [27, 31]. There are other types of joining techniques for Nitinol such as crimping and swaging.

1.3.4 Thermal Annealing

The thermal annealing is performed in order to set the transformation temperature of the Nitinol, which is essential to reconstruct the microstructure of the heat affected zone, resulting from the prior fabrication processes. On the one hand, the Nitinol material is typically thermally annealed in the temperature around 500 °C to achieve superelastic properties in a desired temperature [32]. On the other hand, the Nitinol alloys are typically annealed in the temperature between 350 °C and 450 °C for better shape memory behavior. Both thermal annealing temperature and time significantly affect the formation of the oxide layer on the Nitinol surface, which govern the thermomechanical and hemocompatible properties of the material [33]. Thermal annealing is

also used for shape setting through the relaxation of the material at the desired equilibrium shape. Shape setting could be carried out at temperature around 500 °C using mandrel in order to have the desired geometry of the devices [34].

1.3.5 Electropolishing

Electropolishing is the final process for Nitinol endovascular devices, which is a standard finishing process for stents, heart valve frames, or any other implantable devices. This process is typically used for creating a smooth surface with a corrosion-resistive coating layer on the outer surface of the metal or alloys [35, 36]. The improved surface smoothness is beneficial for endovascular devices due to its enhanced biocompatibility property as implantable devices. Electropolishing reduces the free surface energy to remove any contamination from foreign materials outside the body; thus, thrombosis formation could be minimized [37]. In addition, the electropolishing finishing process has been proven to reduce the nickel concentration on the surface of Nitinol alloys [38].

1.4 Examples of Nitinol Endovascular Devices

1.4.1 Stent Grafts

Stent is a mesh scaffold used to widen the narrowed blood vessel due to atherosclerosis or plaque formation, typically inside the coronary, intracranial, or peripheral arteries [39–41]. The stents are also used for blocking dilated arteries (i.e., aneurysm) or for inserting a new conduit in

the aneurysm locations in order to prevent potential rupture of aneurysms. Intravascular stenting technique was first investigated by Charles Dotter in 1969 [42]. This technique was developed to reconstruct vascular patency using transcatheter procedure, in a way other than percutaneous balloon angioplasty, which temporarily dilates the narrowed blood vessel with the inflated balloon to break the plaques or to push away the fatty substances to the wall [43]. Most of the devices in this era were coil spring-shaped stents. More than one decade later, Julio Palmaz developed a tube-shaped balloon expandable stainless steel stent for small artery applications [20]. Balloon inflation is needed to deploy the stainless steel stent to generate permanent plastic deformation in the stent because stainless steel is ductile in the range of expansion from the delivery catheter size to the target artery size [44, 45].

Although balloon expandable stents have been widely used in earlier stent history, there are potential vessel wall damages that lead to severe restenosis (i.e., tissue ingrowth) due to the over-expanded balloon dilation to place the stent [46]. Therefore, self-expandable stents were widely investigated to replace the balloon expandable stents, which is simple to deploy, generating minimal intima damages [47]. One of the best metallic materials for self-expanding stents is Nitinol as described in the earlier section. There are primarily two types of Nitinol stents: (1) laser-cut stent from thin wall Nitinol tube for small diameter applications (e.g., coronary artery, neurovascular, or peripheral arterial stents) and (2) wire braided or bent stent for large diameter applications (e.g., thoracic or abdominal aortic aneurysm stent grafts). Figure 4 shows representative commercially available Nitinol stent products for peripheral artery treatments. Figure 4A represents the Innova™ (Boston Scientific) stent, which can be used for proximal popliteal artery and superficial femoral artery. Figure 4B shows VIABAHN® (Gore Medical) stent graft, where the metallic backbone is covered by thin polymer, typically either expanded

polytetrafluoroethylene (ePTFE) or Dacron polyester. This type of stent is used to graft the disease tissue and also to protect aortic–thoracic aneurysms from rupture [48, 49].

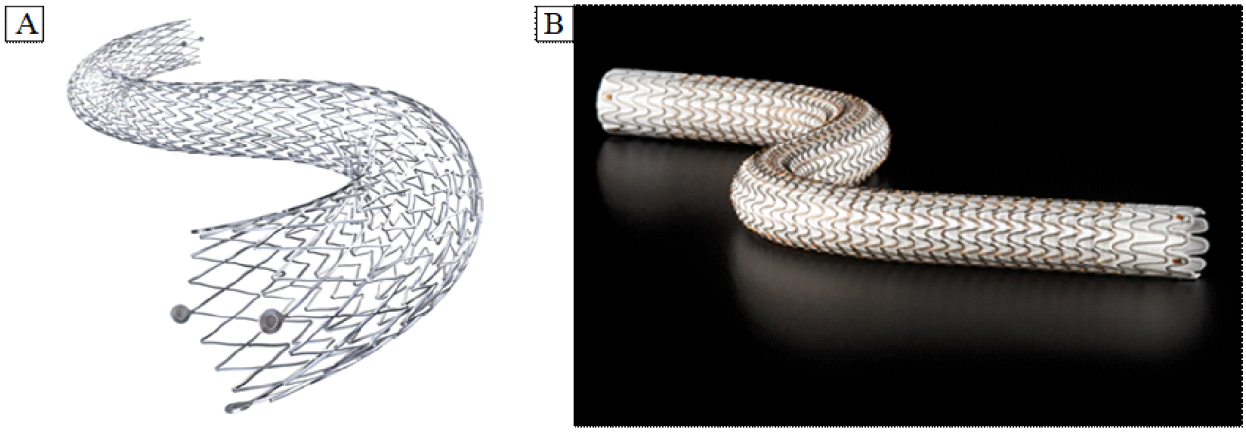

Figure 4 A) Innova™ Stent Delivery System (Boston Scientific). B) VIABAHN® Endoprosthesis (Gore Medical)

In addition, Nitinol stent is non-ferromagnetic, which is MRI compatible. Patients who have stents in the body do not have problems taking MRI in the future after the placement of the stents [50]. The common approach used for the stent delivery is keeping the stents in the cooler martensitic phase for crimping and then inserting into the catheter. Once the catheter reaches the desired location inside the body, it is removed to deploy the stent with Nitinol's own superelasticity.

1.4.2 Percutaneous Heart Valve Frame

Symptomatic aortic stenosis (AS) is considered one of the main valvular heart disease, which is an important source of cardiovascular morbidity and death worldwide [51]. Aortic stenosis is the narrowing of the valve that delivers high pressure oxygenated blood from the heart

to the aortic artery, which carries the blood to the main abdominal organs and the lower part of the body. The standard treatment of aortic valve stenosis is open chest aortic valve replacement; however, most of the patients are elderly who may not survive due to the open-surgery complications. Thus, one-third of the patients are rejected for surgery [52]. Less invasive techniques were adapted to overcome the open-chest complications. Percutaneous aortic valve replacement has developed as a new promising technique in recent years as a minimally invasive operation for symptomatic (AS) treatment [53, 54]. Figure 5A shows a representative commercially available Nitinol heart valve is CoreValve RevalvingTM System that is integrated with porcine pericardial trileaflet valve sewn to the Nitinol backbone using ePTFE sutures [55]. The placement of the valve is performed under fluoroscopic guidance as shown in Figure 5B. Figure 5C shows the implanted heart valve after a few months, which shows that the Nitinol valve replaced the aortic valve well.

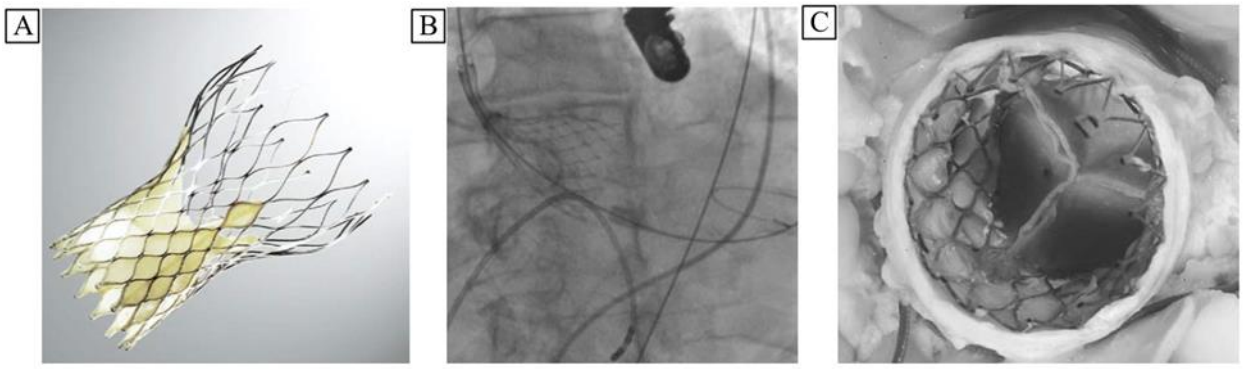

Figure 5 A) CoreValve ReValving System profile [43]. B) In situ Coronal MRI image CoreValve prosthesis, after six months' implantation [40]. C) Fluoroscopic guidance for implanting the CoreValve prosthesis [40].

1.4.3 Vena Cava Filter

The vena cava is a large vein that carries the deoxygenated blood to the heart. The human body has two venae cavae: the superior vena cava that carries the blood from head and upper body and the inferior vena cava that carries blood from the lower body. Clots formed in these veins could travel to various locations and may cause fatal complications in the brain or lungs with the clots or fragmentation from clots (i.e., clot embolization) [56]. Due to the device's large deployed diameter, it is always challenging to deploy endovascular devices [57]. However, with the aid of shape memory metal like Nitinol, the filter can be cooled and inserted as straight wire, then when the filter is left in the body temperature, the filter automatically recovers its shape. Figure 6A shows the filter inside the body, with full recovery and good positioning [58]. Figure 6B shows the commercially available Optease vena cava filter (Cordis), which is used as a temporary filter. The filter consists of six diamond shaped laser-cut Nitinol struts. The filter contains a self-centering portion and the upper hook for easy retrieval of the filter. Another commercial Nitinol filter is the Denali vena cava filter (Bard, Figure 6C).

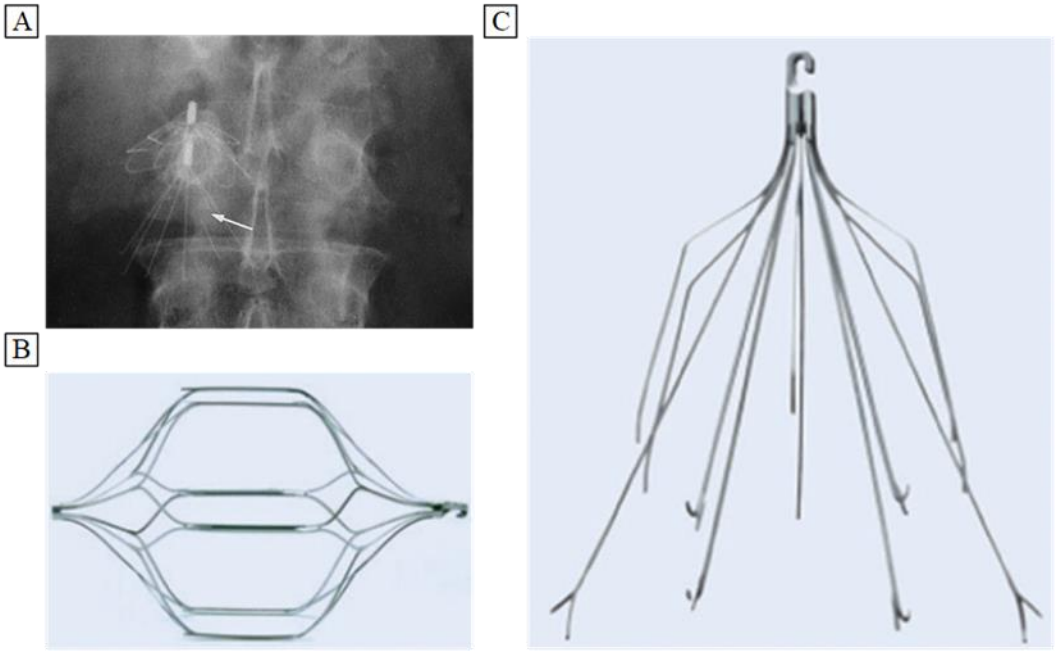

Figure 6 A) Abdominal plain film. The Simon Nitinol filter is well positioned in the inferior vena cava [58]. B) Optease vena cava filter (Cordis) [59]. C) Denali vena cava filter (Bard) [59].

1.4.4 Atrial Septal Defect (ASD) Occluder

Atrial septal defect (ASD) is a hole that occurs in the septum, the wall that separates between the upper chambers of the heart. This defect allows the oxygenated blood, which comes from the lungs in the left atria, to induce a leakage to the poor-oxygenated blood in the right atria. Even though open-heart surgical operation is widely accepted to repair the defect, exploiting minimally invasive alternatives has been recently developed to overcome any complication found in the open-heart surgery [60]. The ASD occluder was named the Amplatzer, which consists of two round disks of Nitinol mesh. The mesh was made from 0.004- to 0.005-inch Nitinol wire, which is tightly woven into two flat buttons, and the disks were linked using connecting waist [61], as shown in Figure 7A. The whole device can be delivered via either 6Fr or 7Fr sheath (Figure 7B), depending on the diameter wire and expanded size of the occluders [62]. The two flat retention

meshes extend to the radial direction beyond the central waist (Figure 7C) to work as secure anchors. The Nitinol mesh is covered with Dacron. The Amplatzer is deployed with ultrasound and fluoroscopic guidance to ensure optimal positioning [60]. Figure 7D shows Cineradiography frames of the ASD occluder implanted inside human body.

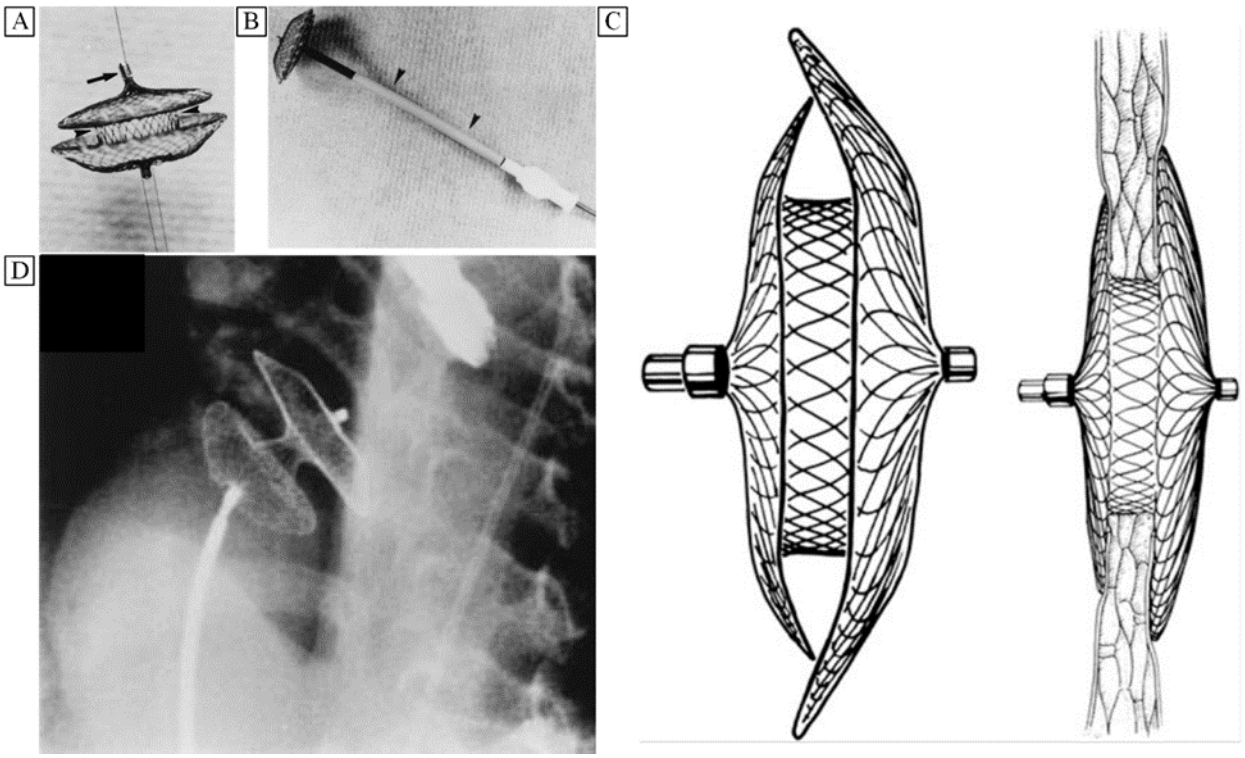

Figure 7 A) Amplatzer septal occluder made of two round disks from 0.005-in. Nitinol wire, that tightly woven into with a 4-mm connecting waist (arrowheads)[63]. B) Adaptor tube (arrowheads) used for the occluder delivery. [63]. C) Mechanisms of leakage-proof closure with the two retention discs, which are angled inward. The left atrial retention disc slightly bigger than the right, to ensure over-fitted clamping against around the defect [60]. D) Good positioning and complete closure of the Amplatzer, are shown using Levo-phase of pulmonary arteriogram [63]

2.0 Research Scope and Objectives

In this study, the main emphasis is exploring the manufacturing process parameters to optimally fabricate the metallic backbone of the stent graft to be used in endovascular application. In this work, the use of a micro-laser welding process was focused to make the stent backbone by joining Nitinol wires. The contribution assigned to be achieved in the laser welding process, are as follows:

- Systematically evaluation of the disconnecting force of the welding joint with respect to the laser welding process parameters (i.e., laser power, frequency, time duration, and spot size), used for a stent graft backbone manufacturing that has complex geometry. Also, investigate the joint configuration impact on the disconnecting force.

After reaching the optimal welding parameters, the mechanical design of the stent graft was investigated in terms of radial force, and resistance accompanied with the device deployment and retrieval. The radial force is crucial for the device performance, which will be studied regarding geometric parameters and thermal treatment conditions. As a retrieval device, the resistance of stent graft movement inside the catheter is critical. The main contributions in this section are:

- Comprehensively studying the radial force of the metallic backbone was comprehensively studied in terms of geometric parameters, including wire diameter, laser welding distance, as well as deployed diameter.
- Examining the effect of heat treatment conditions such as, annealing temperature and annealing time, on the backbone radial force.

- Studying the Various forms of configurations for the polymer covering onto a Nitinol backbone to accommodate the retrieval and deployment resistance level, especially for the long stent graft.

Using the results from the optimization of the laser welding manufacturing process, as well as the outcomes from the design dimensions, and thermal treatment conditions, to fabricate stent graft for two medical applications. First device will be Rescue stent, which rapidly controls excessive internal hemorrhage in the torso region. The contributions, achieved via in vivo swine models are:

- Rapid control of the internal hemorrhage in the torso region providing sufficient blood flow to the entire body including organs.
- Customizing an extremely long stent graft to control hemorrhage in the torso, which can be fully deployed and retrieved in very short time.

The other device, fabricated from the optimization process, is the organ perfusion stent (OPS). This device will be used to address the problem of abdominal organs shortage by targeting the donation after cardiac death (DCD). The stent graft is used inside swine model to achieve the following contributions:

- Introducing a new stent graft fabricated via the optimized micro laser welding parameters, which can be successfully delivered through a typical transcatheter procedure, isolating the cardiac flow without any biocompatibility issues, and retrieved after use.
- Presenting a new stent graft that will significantly increase the number of available organs from the donors after cardiac death, by reducing any potential organ ischemic complications

The focus is to optimize the manufacturing conditions and geometric design parameters of the metallic backbone of stent graft, to fabricate fully functional, as well as retrievable devices for torso region. Specifically, the rest of the work is arranged as follows,

- Chapter 3 will investigate the optimization process for manufacturing parameters regarding laser welding of the Nitinol wires to fabricate the stent graft. The optimization objective is emphasizing on the disconnecting force of welding joints.
- Chapter 4 will study the mechanical assessment of the stent graft performance used to control internal traumatic vascular injuries, with respect to geometric parameters, heat treatment conditions, and polymer-metal configuration.
- Then, chapter 5 will discuss the design validation of a newly developed stent graft for the abdominal organ perfusion with cardiac blood flow isolation, achieved in the area of endovascular devices through research investigation will be mentioned in Chapter 6.
- Finally, Chapter 7 will discuss the conclusion of this thesis, list of papers as first author or co-author, the conferences, and the awards through this PhD program.

3.0 Manufacturing Process Optimization of Laser Welding Joints

3.1 Introduction

Several manufacturing technologies are available for creating Nitinol-based endovascular devices, for example, laser machining, compression molding, photochemical etching, micro-electro-discharge machining and electroforming. The laser machining of the cylindrical Nitinol tube is one of the most common manufacturing methods in developing stents or other similar endovascular devices with mesh structure. Briefly, the hollow tube is cut into the final device geometry in order to create stents using a laser machining technique, then, any surplus material is eliminated by post processing such as electropolishing and mechanical polishing. While the laser machining process is a gold standard technique used for stent fabrication, one of the major drawbacks of the laser machining is the formation of a heat affected zone (HAZ), in which microstructure and mechanical properties are unfavorably changed and, the microstructure gradient and stress are created within the structure which deteriorates fatigue resistance properties [64]. Additionally, impurities and dross that are typically produced in this process due to the elimination of the surplus materials, necessitate the subsequent finishing processes [65].

Typical subtractive manufacturing process with a laser (or waterjet-guided laser) is highly recommended and widely used for several Nitinol devices for treating small arteries, such as coronary, peripheral, carotid, or cerebral arteries. However, laser machining (cutting) has several challenging issues for creating larger endovascular applications. For example, both thoracic and abdominal aortic stent grafts have up to one-inch diameters. Because these devices are used in high blood flow regions, the devices contain relatively thick Nitinol struts (i.e., typically wire) in

order to exert higher radial force to prevent the device migration. The laser machining process is not considered as an effective technique to create these large devices, because they require a large diameter extruded Nitinol tube with a relatively high thickness, which drastically increase the manufacturing cost or sometimes not possible with widely used extrusion machines. Additionally, more than 90% of Nitinol tubes will be discarded after the laser cutting, which is considered a very non-efficient way of manufacturing. Therefore, Nitinol wires are typically used for large diameter endovascular devices. The wires used in these devices are connected via thin-wall metal tube or with polymeric covering membranes (e.g., e-PTFE or Dacron polyester) to secure the Nitinol wires in place. However, the use of Nitinol tubes or polymeric covering adds the bulkiness of the whole structure, increasing the size, and stiffness of delivery catheter size, which generate difficulty to deliver the device into the desired location. Therefore, the ideal manufacturing process will be a direct wire-to-wire connection without adding any additional structures for the minimally invasive medical devices.

In this study, multiple laser-welded Nitinol joints have been created by changing laser parameters, to study the effect of the laser power, frequency, and spot size. The outcomes would be beneficial for the manufacturing of Nitinol-based endovascular devices by providing optimized parameters of the laser-welding process for Nitinol. The joining strength of the welds was investigated to study the capability of expanding the stent up to one-inch diameter. The weld strength is quantified by measuring the disconnecting force of the joints by either detachment or fracture of the welds.

3.2 Materials and Methods

3.2.1 Preparation of Micro Laser-Welded Nitinol Joint Samples

To prepare laser-welded Nitinol joint samples, two Nitinol wires (Nitinol Devices & Components, Inc., CA) with diameter of 200μm and length of 8cm were cut and placed parallel to each other under optical microscope to ensure no gap remained between the two wires. The two Nitinol wires were welded together using Nd: YAG laser source in the laser welding machine (PulsePoint Studio plus 100 Laser Welder, Neutec /Rio Grande™, NM). The laser beam hit the middle of parallel wires and created a joint that attaches the two wires. Once two Nitinol wires were welded, thermal treatment and subsequent quenching process was performed. This process is a conventional post-treatment method used for Nitinol materials in medical implants (e.g., stent) for obtaining superelastic behavior [34]. All samples fabricated by a micro laser welding were thermally treated in 500°C for 20 min and then rapidly quenched in 20°C DI water for 1 min.

3.2.2 Evaluation on Disconnecting Force of Nitinol Joints

A mechanical test system (FLC-5E, Starrett, MA) was used to measure the disconnecting force after the laser joining process both before and after thermal annealing. Figures 8A-D show the pulling (disconnecting) progress of the Nitinol wires. The load cell, attached to the mechanical testing system, measures the forces employed on the samples during the pulling. The disconnecting force is determined by the difference between the recorded force at the pulling start, and the recorded force at the disconnecting time, which is indicated by abrupt drop of the force as shown in Figure 8E.

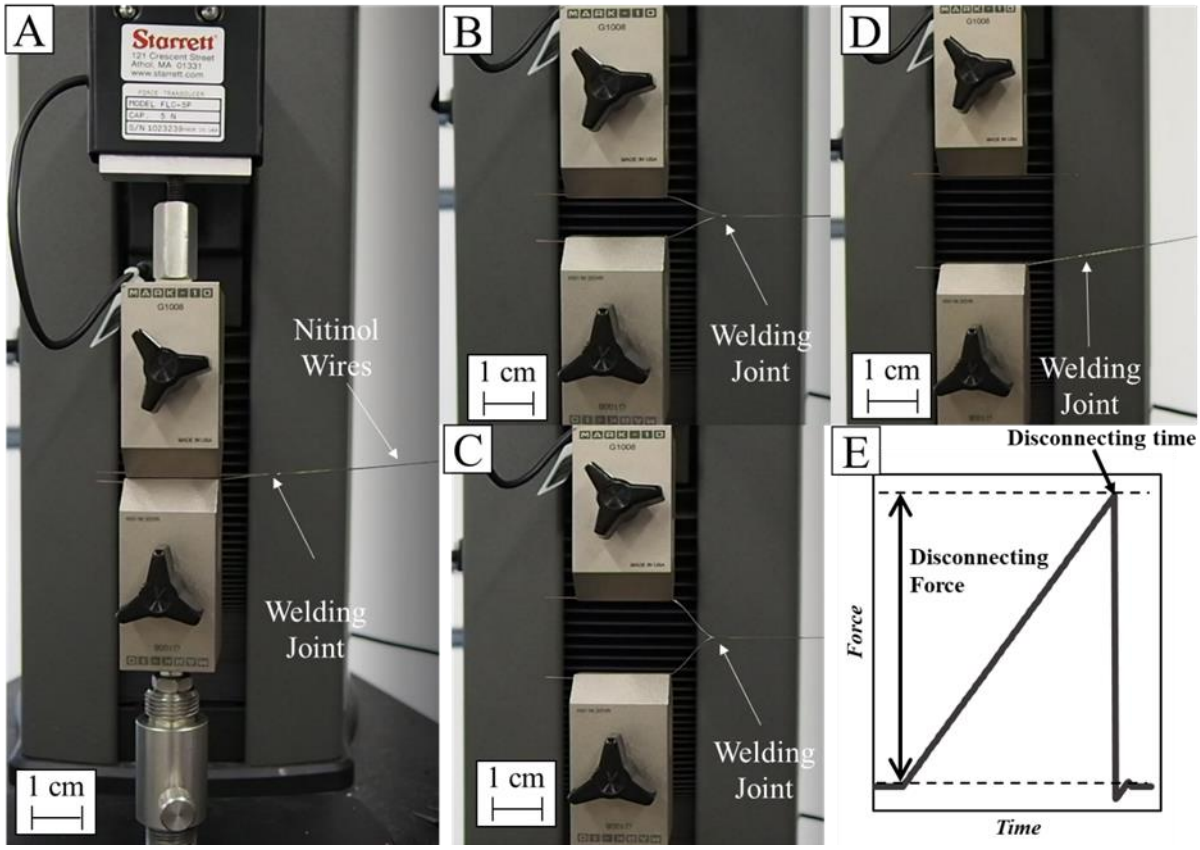

Figure 8 Experimental setup for disconnecting force measurement of the laser-welding joints. A-D) are the progress of the applying force on the joints, beginning at A) with no force, up to C) which shows the detachment of the two wires. Figure E) shows how the disconnecting force is measured as the difference between the force at test start and the force on disconnecting time.

The effect of laser parameters, power, frequency, and spot size was investigated on the disconnecting force of Nitinol wires. Welding joints were produced using laser powers, 0.6, 0.8, 0.9, and 1kW, while keeping the frequency 1Hz, spot size 0.4mm, and 1ms time duration. The frequencies 1, 8, and 15Hz, were used to determine the frequency influence on the disconnecting force, the power was 1kW, spot size was 0.4mm, and time duration was 1ms. Also, the impact of spot sizes 0.3mm, 0.4mm, and 0.6mm was studied on the disconnecting force of welding joints,

while fixing the power on 1kW, frequency on 1Hz, and time duration on 1ms. The parameters used in the study are summarized in the following table,

Table 1 Summary of laser parameters used for disconnecting force study

Parameter	**Power (kW)**	**Frequency (Hz)**	**Spot Size (mm)**
Values	0.6, 0.8, 0.9, and 1.0	1, 8, and 15	0.3, 0.4, and 0.6

The effect of the Nitinol wire thickness was investigated on the disconnecting force of the welding joints. The force was measured for wires thicknesses, 0.3, 0.35, 0.4, and 0.45mm, in addition to the laser parameters were power 1kW, frequency 1Hz, 0.4mm spot size, and 1ms time duration. The impact of the number of laser spots was examined by changing the number of spots from one spot, into 2-spots, 3-spots, and 4-spots. Also, one laser spot was added in the backside of the welding joint, as well as 2-spots, and 3-spots. For the number of spots study, the laser power was 1kW, the frequency was 1Hz, the spot size was 0.4mm, and the time duration was 1ms.

3.3 Results

3.3.1 Laser Welding Joints

Figure 9 shows representative SEM images of the laser-welded joints that connect the two parallel Nitinol wires. Figures 9A-C represent the SEM images for 1-spot, 2-spots, and 3-spots welding for Nitinol wires depending on the type and length of connected regions. The welding

zone has a dot- like shape that slightly retracts on both sides in the middle of the joint forming an arc in each side.

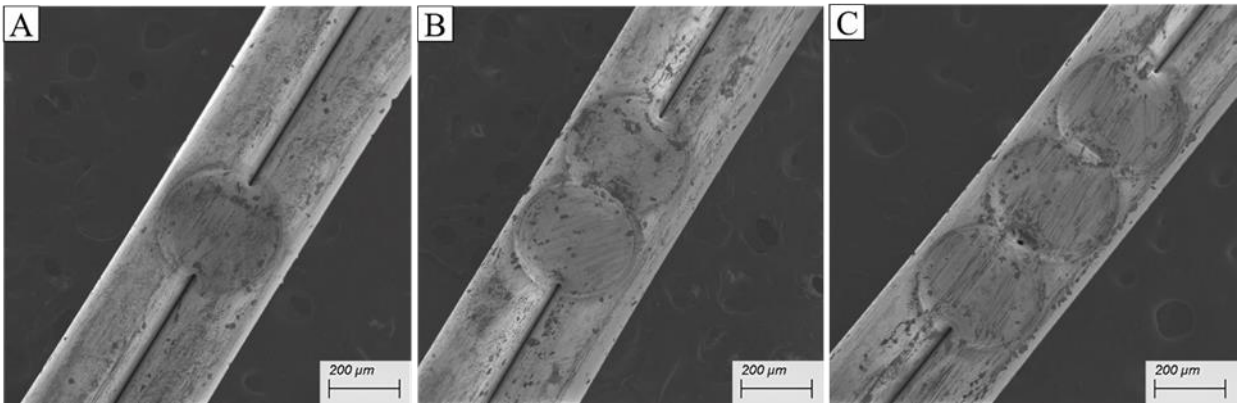

Figure 9 SEM images for laser welded spots between two parallel Nitinol wires. A) One spot. B) Two spots. C) Three spots.

3.3.2 Disconnecting Force of Nitinol Joints

The disconnecting force of the welding spot is a quantitative aspect to determine the strength of the joint, and govern the collective strength of the device, constructed from these welding joints. For different power values, the disconnecting force increased with higher levels of power, to hit the maximum at 1kW, as shown in Figure 10A. Also, the annealing process increased the disconnecting force for all power levels. Frequency change showed less impact on disconnecting force as shown in Figure 10B, reaching the maximum at 1Hz frequency with a small margin. Joints after annealing demonstrated slight increase for frequencies, 1, 8, and 15Hz. Figure 10C demonstrates that the spot size is affecting the disconnecting force, where 0.6mm spot size showed the highest disconnecting force value.

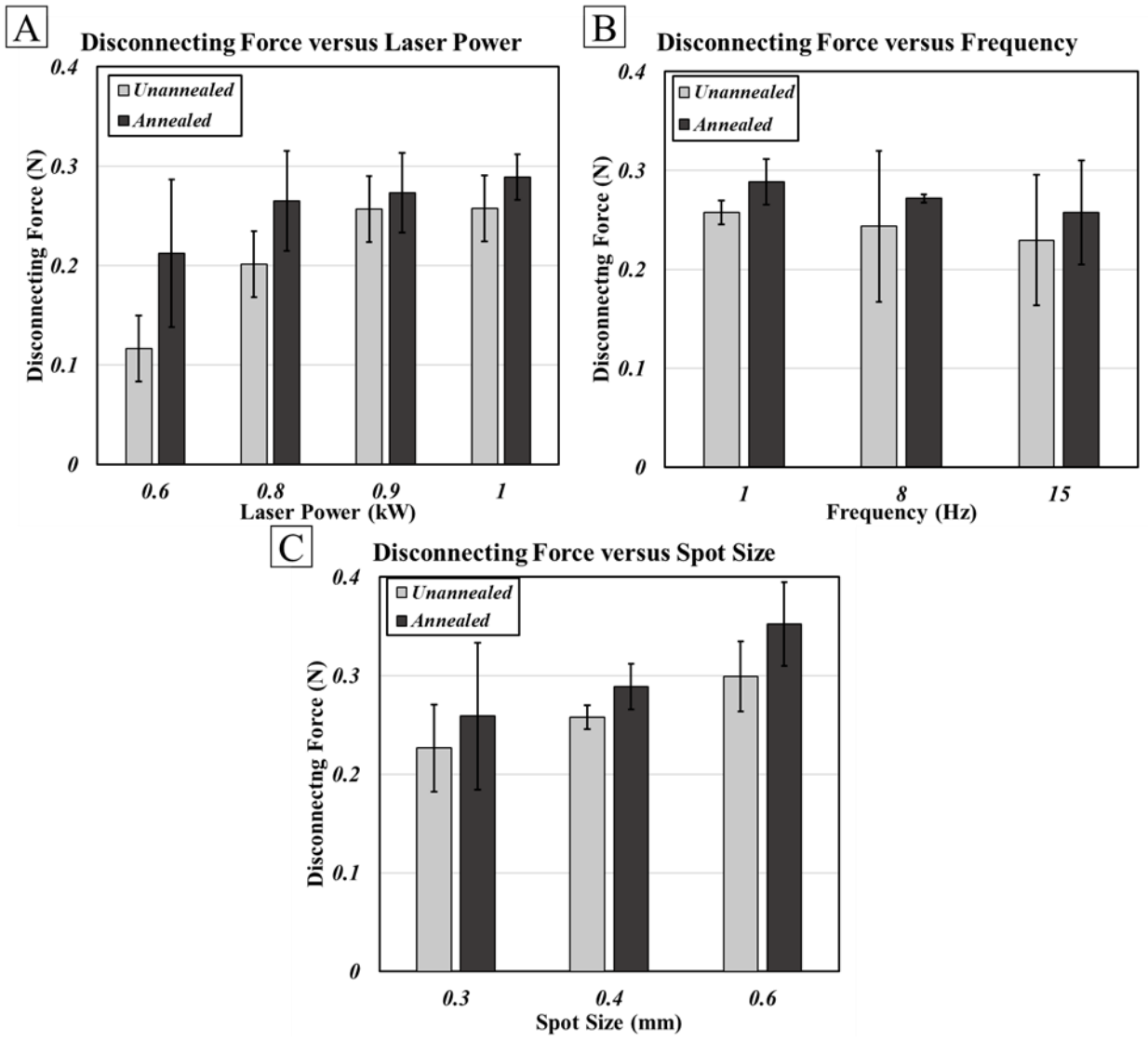

Figure 10 Effect of laser parameters on disconnecting force of the laser-welded joint. A) Disconnecting force for several laser powers, 0.6, 0.8, 0.9, and 1kW. B) Disconnecting force for different laser frequencies, 1, 8, and 15Hz. C) Disconnecting force for different laser spot sizes, 0.3, 0.4, and 0.6mm.

The effect of Nitinol wire thickness was studied on disconnecting force, and the maximum disconnecting force was found for 0.4mm wire thickness, however, after annealing the maximum disconnecting force jumped to 0.45mm wire thickness, as shown in Figure 11.

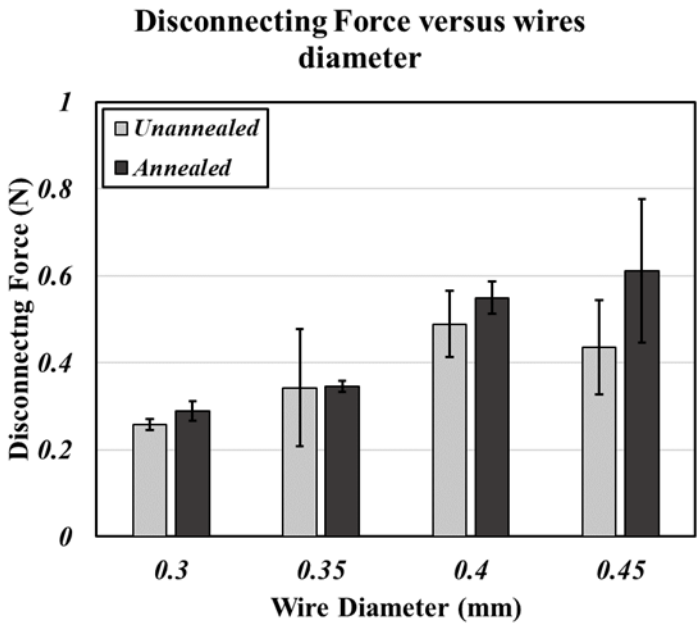

Figure 11 Effect of laser joint configuration on disconnecting force of the laser-welded joint. Disconnecting force for several wire diameters, 0.3, 0.35, 0.4, and 0.45mm.

The welding configuration was investigated to illustrate its role on the strength of the welding joint. In Figure 12A, with increasing the number of laser spots, the disconnecting force increased to be maximum for 3-spots case before annealing, and 4-spots case after annealing. Also, laser spots were added in the back side of the primary welding joints, and the disconnecting force raised by significant force value, to be maximum at 2-backspots before annealing, and the highest disconnecting force was the 3-backspots case, as shown in Figure 12B.

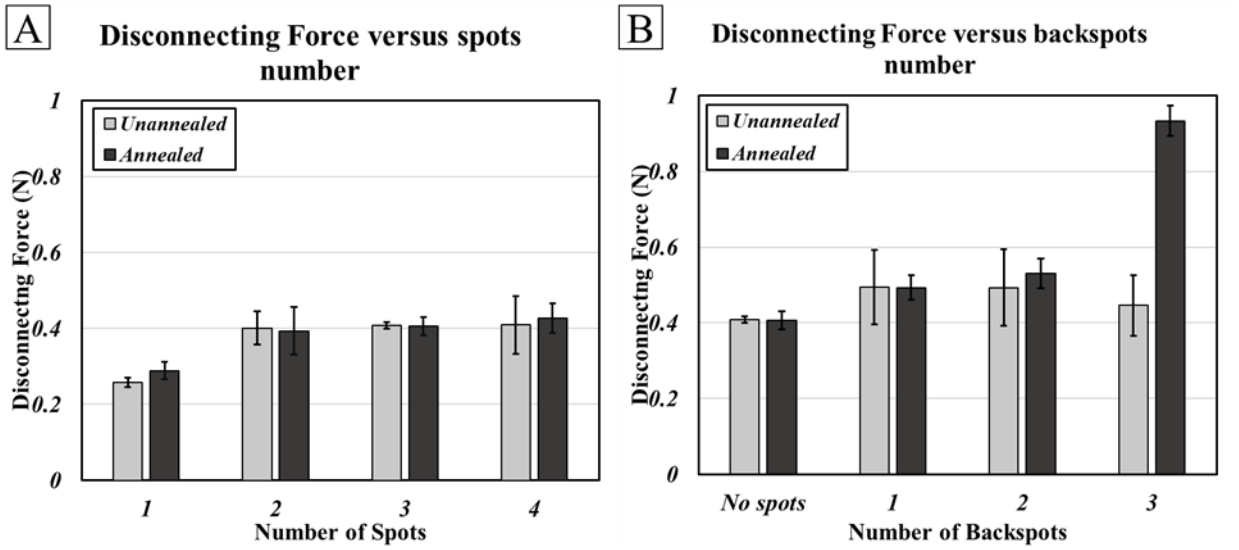

Figure 12 A) Disconnecting force for one-, two-, three-, and four- laser spots welding joints B) Disconnecting force for zero-, one-, two-, and three-, laser spots on the back of welding joints, while having 3-spots in the front side of the joint.

3.4 Discussion

An appropriate manufacturing technique is needed for Nitinol medical implants (or prosthetics) to create precise size, and geometry control with minimal thermal, as well as structural distortion. One ideal candidate manufacturing process of Nitinol stents (and other medical devices) would be the micro laser welding for joining Nitinol, which shows high and reliable controllability for welding low-profile components, due to the precise control of welding parameters such as laser power, spot diameter, frequency, and time duration. Zhou et al., showed that the tensile strength, fracture mode and ductility of the laser-welded joints highly depend on the processing parameters of peak power and the pulse frequency. Among the examined values of peak power (i.e., 0.6, 0.7, 0.8 and 0.9kW) and pulse frequency (i.e., 1, 5, 10 and 15Hz), the results of their research showed

higher peak power and lower pulse frequency created higher tensile strength and ductile failure mode similar to the base alloy [66].

The disconnecting force results have shown that the welding parameters impact the strength of the welding joints. More power increased the disconnecting force, as the additional power melts extra metal through wire depth, which enhanced the stiffness of the joint. The laser frequency didn't affect the disconnecting force significantly, however, the annealing process raised the disconnecting force, not only in the frequency study, but also, for the power study. The annealing process removes the stress concentration due to the welding process that improves material ductility, which leads to boost the necessary force for welding joint detachment. Spot size showed influence on the disconnecting force, which increased with larger spot size. The effect of spot size occurred due to the diameter of the welded joint increasing with bigger spot size, which augmented the distance required by the crack propagation to induce broken joints.

The welding joint configuration, number of laser spots, affected the needed force for joints to be detached. The disconnecting force jumped almost double, once the number of spots increased from one-spot. The results showed that the disconnecting force saturated after using 2 spots, where the two spots were disconnected totally. However, the disconnecting behavior changed in 3-spots and 4-spots cases, the spots didn't disconnect, but the wires were broken in the middle of the spot's location. Before annealing, applying spots in the backside of the welding joint improved significantly the disconnecting force, since it increased the molten metal between the wires. The maximum disconnecting force occurred at the 2-backspot case, as more spots increased the brittleness of the welding joint that is broken in lower values of force. On the other hand, after annealing, the disconnecting force jumped to roughly double for 3-backspot cases, as the heat

treatment improved the heat affected zone from welding, which reduced the stress concentration, and the joint brittleness has declined that resulted in improved disconnecting force.

3.5 Conclusion

The disconnecting force was studied in terms of laser parameters and joint configuration. The optimal conditions for disconnecting force were 1kW power, 1Hz frequency, and 0.6mm spot size. The welding joint configuration was optimized to have 3 or 4 spots, associated with 3 spots in the back surface of the joint. The annealing heat treatment has increased the disconnecting force of the welding joint, in almost every case investigated.

4.0 Mechanical Property Assessment of Long Stent Graft to Control Hemorrhage in Torso

4.1 Introduction

Hemorrhage control in the torso part is one of the substantial aspects in the patient's survival. Many devices and treatment options have been developed to control internal bleeding, which help the surgeons in regulating the hemorrhage in the injured region with reasonable performance at the earliest possible time. There is an immediate need for developing a new stent graft to rapidly control excessive internal hemorrhage either in wounded soldiers near the battlefield or in injured civilians. The schematic for aortic injury is shown in Figure 13A. The desired features of a new long stent graft, used for massive traumatic hemorrhage of the great vessels with limited experience and limited imaging, would be rapid delivery, the ability to control hemorrhage along the entire vessel even when the injury site is not known, and the ability to remove the stent graft at the time of a more focused permanent repair.

A new stent graft has recently developed, for internal hemorrhage control in the torso region. This new endovascular device is designed considering the anatomy of animals (currently swine but human in the future) [67, 68]. The device, shown schematically in Figure 13B, contains a considerably long backbone structure that is selectively covered with thin stretchable polymeric membrane. With the new design and fabrication methods, this new stent graft could substantially decrease malperfusion of the cardiac blood flow to the entire circulatory system in the body. The prototypes have demonstrated rapid control of the internal hemorrhage in the torso region providing sufficient blood flow to the entire body including organs. This stent graft is intended for an ultrashort duration of implantation for emergent, but brief control of life-threatening

hemorrhage, as a patient is transported between hospitals or even with a hospital, with an expected duration of less than one hour. Patients can bleed out in less than 15 minutes, which is why this stent graft is necessary and will only be in place until a qualified vascular specialist can permanently repair the injury (and remove the stent graft).

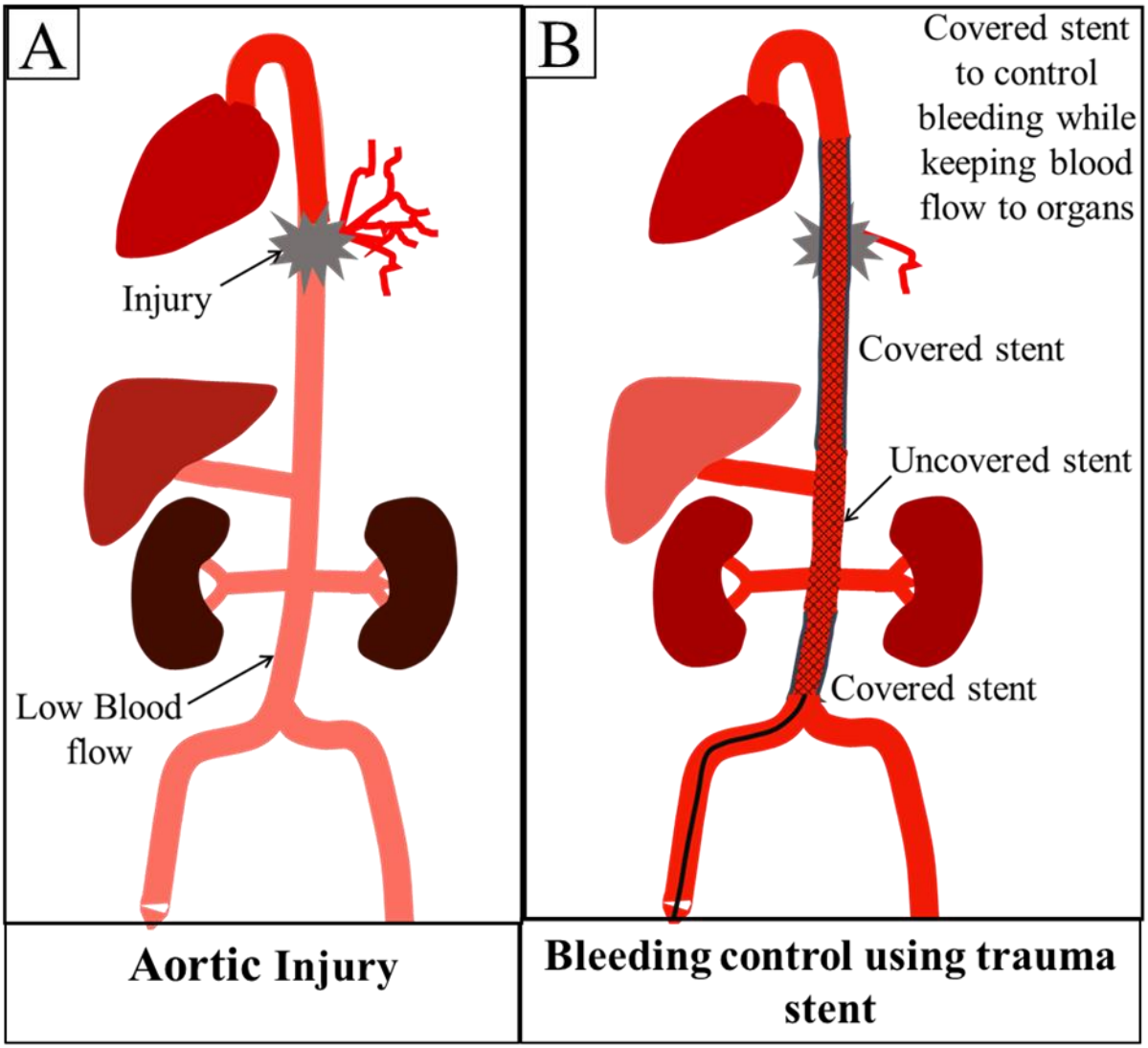

Figure 13 Schematic of the incompressible injury of the aorta artery. (A) The Aortic injury, causing the patient to bleed to death. (B) Using the novel stent graft, the blood flow is controlled inside the aorta artery, supplying blood to the organs in the abdominal region.

In this section, mechanical property assessment methods are used to guide the design and manufacture processes of new stent grafts, which encompass unusual features, such as extreme long, or complex structures. So, results, shown from the mechanical measurements, will be universally applied to various endovascular devices that contain complex geometries. Various types of mechanical property assessment are critical to demonstrate the newly developed stent grafts' mechanical performance, such as radial force, deployment/retrieval resistance, or leakage.

In the past few decades, it has become increasingly popular to treat many vascular diseases using endovascular devices due to the nature of minimally invasive procedures [72, 73]. One of the most important endovascular devices are stent grafts, also known as "covered stents", which are widely used for repairing damaged blood vessels and diseased arteries or veins [42,71]. The representative diseases that can be treated by stent grafts include aneurysm [72], vascular coarctation [73], arteriovenous fistula [74], and pseudoaneurysm [75]. Recently, a new stent graft has been developed to control non-compressible hemorrhaging in the torso region for civilians or soldiers injured by penetrating trauma [76]. Commercial stent grafts have been classified as balloon-expandable [77, 78] and self-expandable stent grafts [79, 80], depending on the deployment mechanism with the metallic materials used. The type of stent grafts is primarily dependent on the location, anatomy, and the difficulty level of deployment, as well as the length and diameter of blood vessel to be treated, such as thoracic [81] abdominal [72,82] aorta, iliac [83,84], and visceral [85] arteries. Typically commercially available stent grafts have a wide range of diameters up to 46 mm and length range from 40 mm to 250 mm [86, 87]. Even the longest of these current stent grafts remains well below the length that would be needed to cover the length of the aorta.

In most clinical settings, two or more short stent grafts are connected to each other by overlapping in order to cover the desired length within the vessel. The delivery is sequentially carried out, where each stent graft is deployed, then the preceding one is deployed with keeping overlapped portions. This deployment procedure is considered relatively complicated and not well suited for emergencies when time is limited and the exact location of the injury may not be known [88,89]. A longer aortic stent graft allows all potential areas of injury to be covered until the exact site of the injury can be identified and repaired.

While there exist many studies on the mechanical behaviors of the typical short stent grafts (< 200 mm in length), there is a lack of study on the mechanical performance of long stent grafts. One of the essential parameters for assessment of stent graft's functionality is the radial force exerted by stent grafts to the vessels, which is associated with (1) the device migration and (2) the leakage between the vessel wall and the deployed device.

Therefore, mechanical behavior study on the new long stent graft would be beneficial for understanding the performance of the device considering deployment, leakage, migration, and retrieval process. In this thesis, comprehensive study results were presented on design, manufacturing, and test results of extremely long stent grafts that could be used as a future endovascular device to treat traumatic injury. The effect of the geometric parameters was explored on the radial force exerted by Nitinol stent grafts. Since Nitinol is a shape memory alloy, then the thermomechanical behavior is dependent on the thermal history. Therefore, the effect of the thermal annealing process on the mechanical response of the stent grafts was also investigated.

4.2 Methods and Results

4.2.1 In Vitro Radial Force Measurement of Nitinol Backbone

Effect of geometrical parameters on radial force of Nitinol backbone is quantitatively characterized using different types of prototypes. Radial forces were measured using a crimping experiment similar to published papers [90, 91]. The crimping was performed by a mechanical test system (FLC-5E, Starrett, MA) that pulls one end of the Dacron strap (Sailrite Enterprises, Inc., IN). The other Dacron end was fixed to a stainless steel rod and wrapped around the Nitinol backbone as shown in Figure 14A. The load cell, attached to the mechanical testing system, measures the forces employed on the prototypes to deform radially as the testing system pulls the Dacron strap. The load cell records the displacement with respect to the hoop force applied on the stent. Radial force is calculated as the hoop force multiplied by $2*\pi$. The relation of radial force and Nitinol wire diameter, distance between two successive welds, and stents deployed diameter, were calculated. Wire diameters 0.009", 0.0120", 0.0140", and 0.0155" was examined, while keeping the distance between welds 23 mm and the deployed diameter 20 mm. For distance between welds analysis, radial force was measured for 17 mm, 23 mm, and 30 mm distances between welds, for 0.0155" wire diameter and 20 mm deployed diameter as in Figure 14B. The effect of the deployed diameter was tested for 15 mm, 20 mm, and 25 mm diameters, Figure 14C, whereas the wire diameter is 0.0155" and the distance between welds is 23 mm. All these prototypes had heat treatment for 20 minutes, followed by the quenching process. The results were plotted as radial force with respect to the reduction percentage (%) of the initial stent diameter.

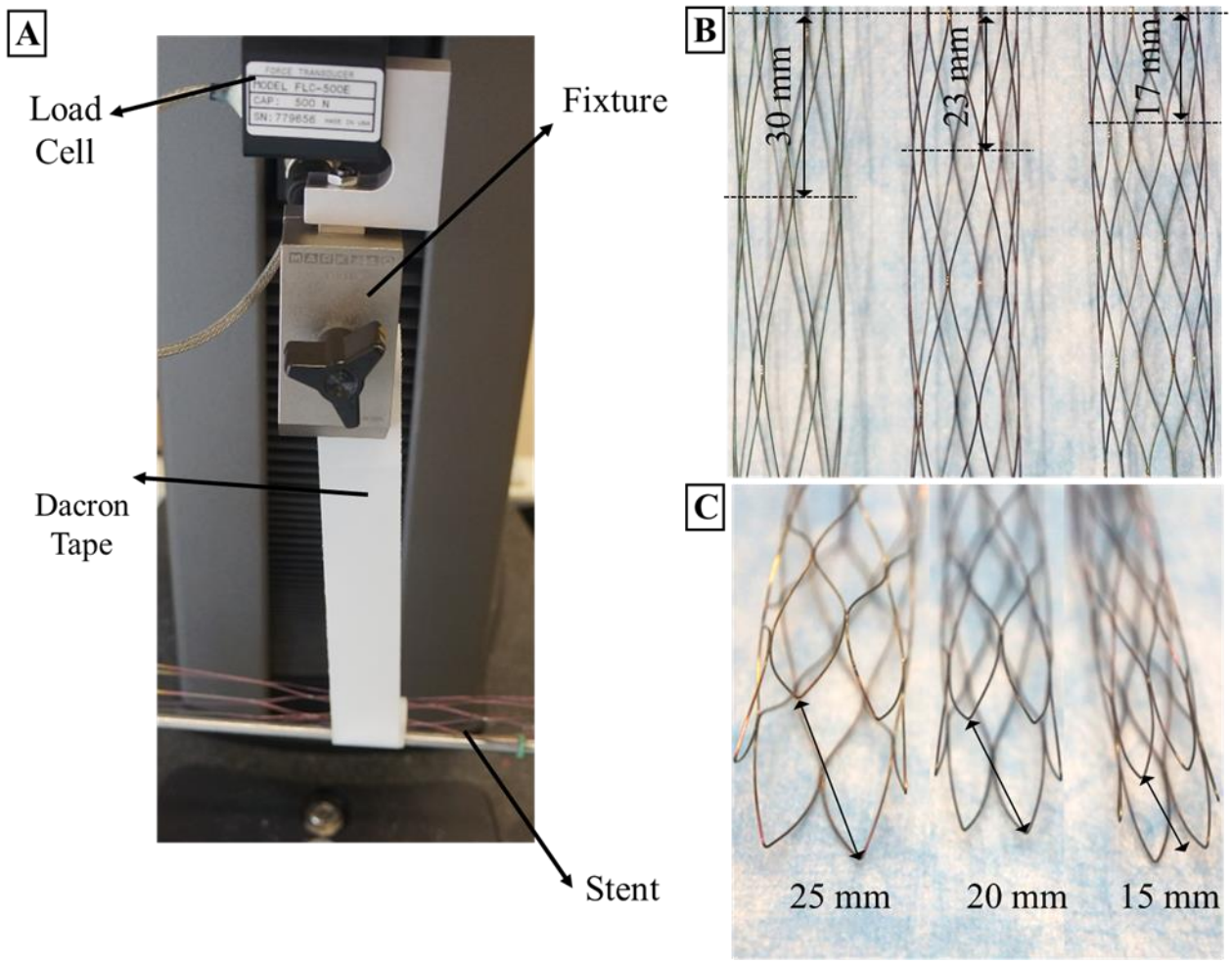

Figure 14 A) Mechanical setup for radial force using mechanical testing system by pulling Dacron strap surrounding the stent. B) Stents with different distances between two consecutive welds, 17 mm, 23 mm, and 30 mm. C) Stents with different deployed diameters, 15 mm, 20 mm and 25 mm.

Figure 15 shows the radial forces of the metallic backbones with varied geometric parameters, including Nitinol wire diameters, welding distances, and deployed diameters. The radial forces are increased with thickener wire diameter as the backbone diameter is reduced by crimping. The highest radial force was observed as 6.5 N for 0.0175” Nitinol wire thickness at 42% backbone diameter reduction as shown in Figure 15A. The distance between welds has the highest influence on increasing radial force by shrinking the welding distance as shown in Figure 15B. The welding distance “17 mm” has the highest radial force of 8.9 N. Figure 15C represents the outcome of increasing the deployed diameter, with highest radial force 6.8 N for 25 mm deployed diameter.

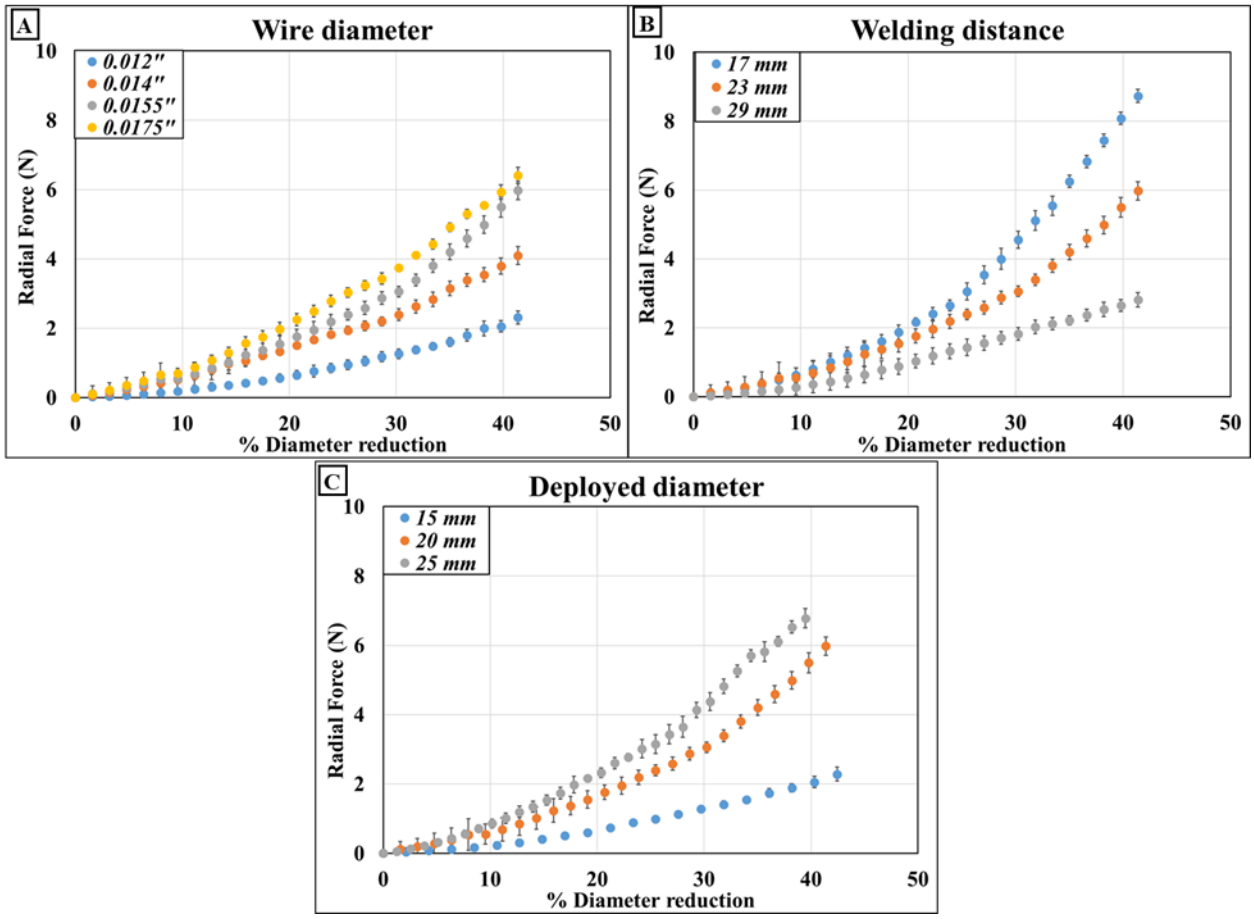

Figure 15 Radial force measurements for different geometric parameters. A) Radial force for several wire diameters, 0.012", 0.014", 0.015" and 0.0175" with respect to diameter reduction %. B) Radial force for different welding distances, 17 mm, 23 mm, and 30 mm with respect to diameter reduction%. C) Radial force for stents with different deployed diameters, 15 mm, 20 mm, and 25 mm with respect to diameter reduction %.

4.2.2 Assessment of Thermal Annealing Effect.

Welding changes the microstructure of the affected zone around the weld, named heat affected zone, which requires thermal annealing to reconstruct the microstructure. Shape setting is performed through thermal annealing, which causes material relaxation at the desired equilibrium shape. Also, the heat treatment temperature and duration affect the mechanical properties of Nitinol. Shape setting is usually carried out at a temperature around 500 °C using a mandrel that has the desired dimensions [19]. The effect of the annealing temperatures 450 °C, 500 °C, 600 °C was investigated on the radial force. The samples tested are 0.0155" wire diameter, 23 mm distance between welds, 20 mm deployed diameter and heated for 20 minutes. The effect of heating duration for 10, 15, 20, 25, and 30 minutes was examined on the radial force, while keeping the temperature at 500°C, 0.0155" wire diameter, 23 mm distance between welds, and 20 mm deployed diameter. Finally, the effect of the number of heat treatment cycles was tested on the radial force. Here, the cycle is the heating of a stent to the annealing temperature for a specific time, then quenching using water to room temperature. The radial force for 1 cycle, 2 cycles, and 3 cycles was measured for 500 °C annealing temperature, 20 minutes annealing time, 0.0155" wire diameter, 23 mm distance between welds, and 20 mm deployed. The results were plotted as radial force with respect to the reduction percentage (%) of the initial stent diameter.

The heat treatment conditions show great impact on the radial force of the metallic backbones. Three parameters, annealing temperature, annealing time, and number of cycles, are explored for evaluating the radial force of the Nitinol backbone. Figure 16A illustrates the effect of the annealing temperature on the radial force with respect to the diameter reduction % of backbones in the crimping process. The maximum radial force is observed as 7.3 N at annealing temperature 600 °C. Annealing time was investigated by varying the time from 10 min to 30 min.

For 10 min annealing time, the radial force was less than 1 N, however, the radial force increases significantly by increasing the annealing temperature as shown in Figure 16B. The radial force is saturated, when it reaches 20 min annealing time. Figure 16C shows that the number of cycles does not have significant differences in different test samples, presenting negligible influence on the radial force.

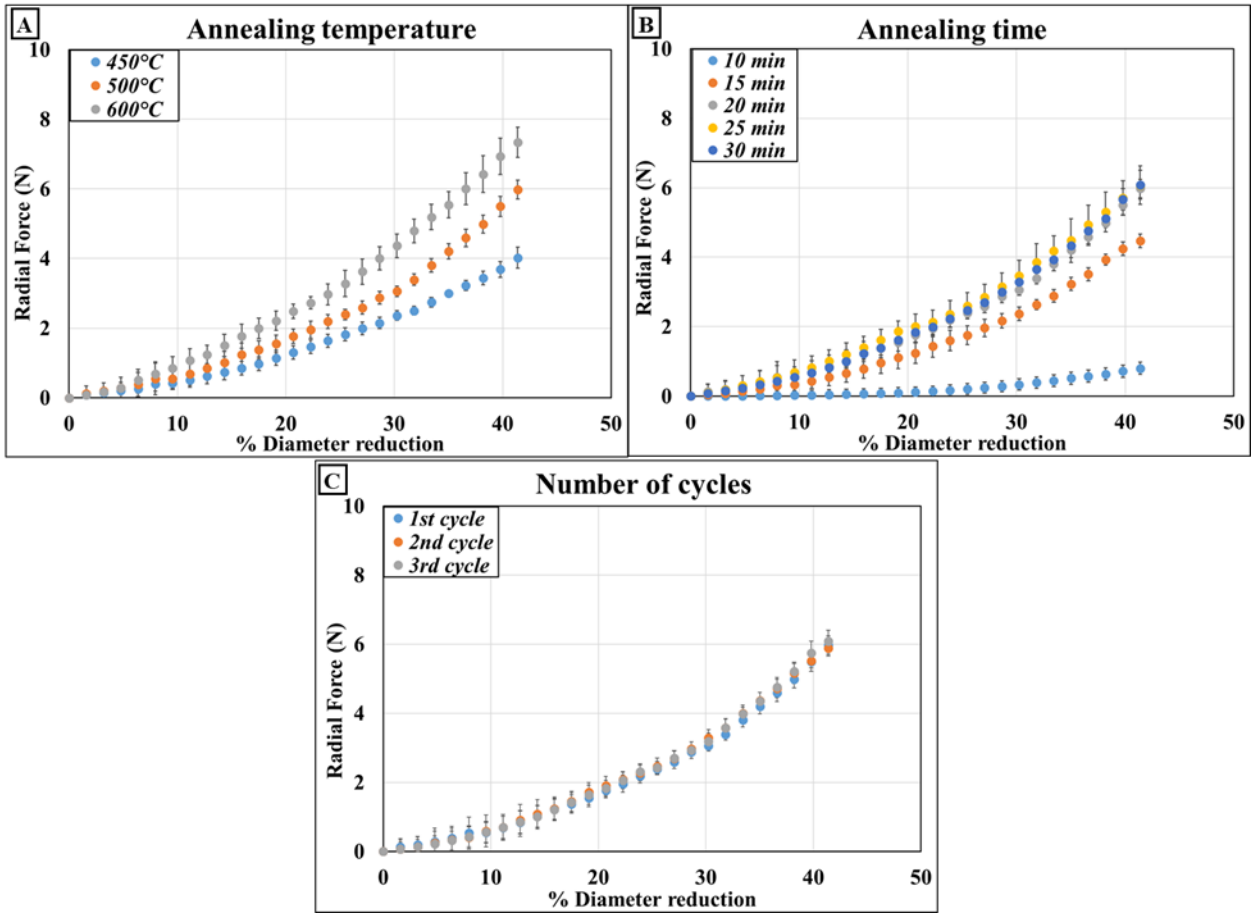

Figure 16 Radial force measurements for stents with different heat treatment conditions. A) Radial force for different annealing temperatures, 450 °C, 500 °C, and 600 °C with respect to diameter reduction%. B) Radial force for several annealing time, 10 min, 15 min, 20 min, 25 min, and 30 min with respect to diameter reduction %. C) Radial force for different number of annealing cycles with respect to diameter reduction %.

4.2.3 In Vitro Device Deployment and Retrieval Tests for Evaluating Resistance

Retrieval stent grafts represent a novel solution, as they would enable the surgeons to use stent graft as a temporary remedy for life threatening bleeding. One of the obstacles for fully retrieval of temporary stent grafts is the resistance exerted by the stent graft in the catheter. The setup for resistance measurement is shown in Figure 17A. The deployment (pushing the stent graft from the catheter) and the retrieval (pulling the stent graft into the catheter) were investigated with respect to the ePTFE attachment to the Nitinol backbone and the size of the catheter used. The pushing/ pulling forces were measured for the backbone only, ePTFE attached outside the backbone, and ePTFE attached inside the backbone as shown in Figure 17B. The prototypes were deployed and retrieved in a 10Fr sheath (OSCOR, Palm Harbor, US). The backbones used for measurement were 500 mm long, 0.0155" wire diameter, 23 mm distance between welds, and 20 mm deployed. The heat treatment of the stents was carried out at 500 °C for 30 minutes. The effect of the catheter size was investigated by recording the pushing/ pulling forces for 8Fr, 9Fr, and 10Fr catheters. The stent, used in these tests, was like previous tests in terms of geometrical dimensions and heat treatment parameters. The results were plotted as deployment/ retrieval force with respect to the deployed percentage (%) of the stent graft outside the catheter.

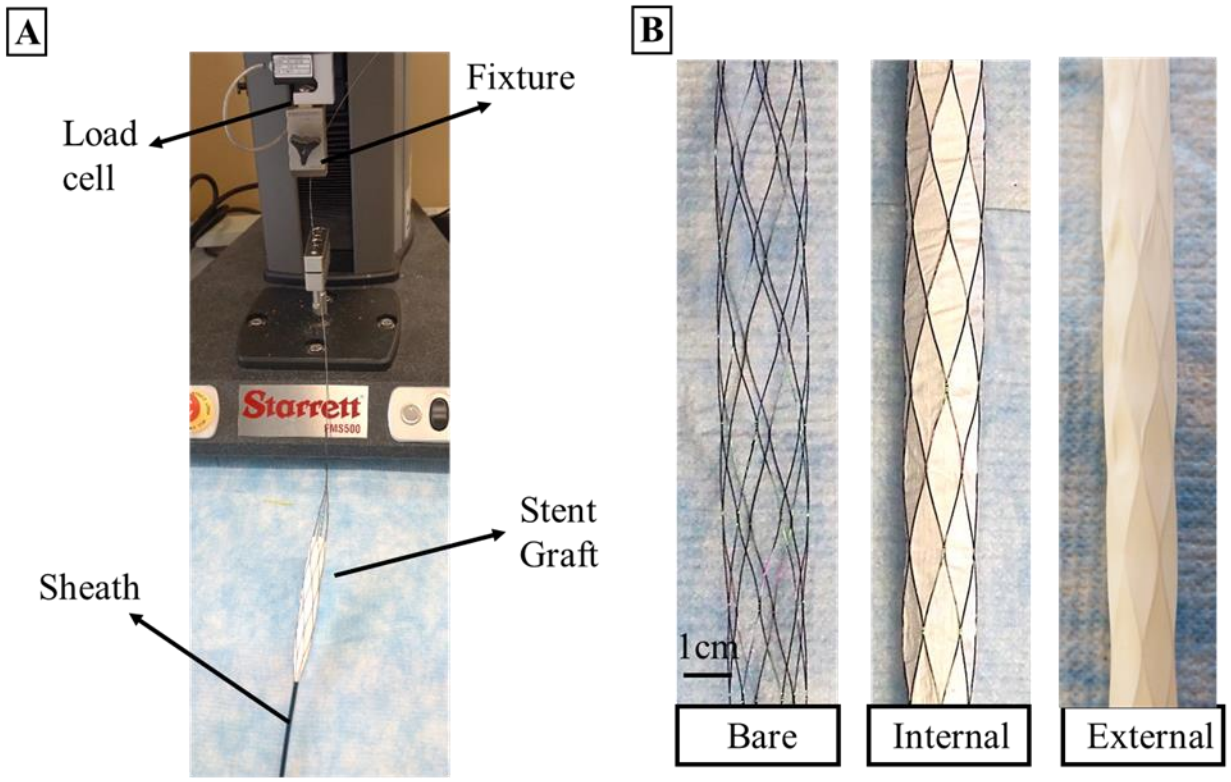

Figure 17 A) Experimental setup for resistance force measurement during deployment and capturing the stent graft in different sheaths. B) Different configurations of ePTFE with respect to the metallic backbone, bare, internal, and external.

As a retrievable endovascular device, the resistance occurring both during deployment and retrieval significantly affects the performance of the stent graft delivery. The ePTFE configuration and the sheath sizes, 8 Fr., 9 Fr., and 10 Fr. were investigated on the resistance forces of the deployment and retrieval of the stent graft. Figure 18 shows the resistance forces of the bare stent (no ePTFE) in different sheath sizes. The highest resistance force was for 8 Fr sheath, while 10 Fr. sheath had the lowest resistance forces.

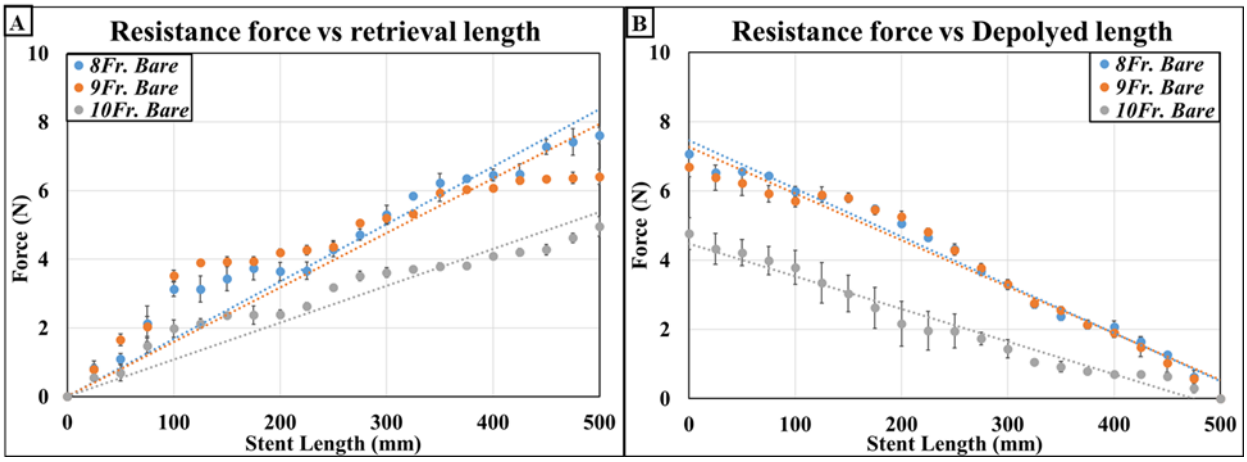

Figure 18 Resistance force for retrieval and deployment of the stent graft in the sheath. A) & B) are graphs that represent the retrieval and deployment resistive forces versus the stent graft length of bare stent in 8 Fr., 9 Fr., and 10 Fr. sheaths.

The resistance forces of retrieval and deployment for stent grafts with different ePTFE configurations are shown in Figures 19. The resistance forces for external ePTFE (Figure 19B & 19D) showed higher resistance forces, also, 9Fr. sheath revealed higher resistance forces compared to 10 Fr. sheath. The device covered with internal ePTFE or external ePTFE, cannot be retrieved inside 8Fr. sheath, due to high values of resistance. Once the device is pushed inside the sheath, the connection between the stent graft and connecting wire is broken. Thus, no information of the resistance inside 8Fr. sheath is presented in Figure 19.

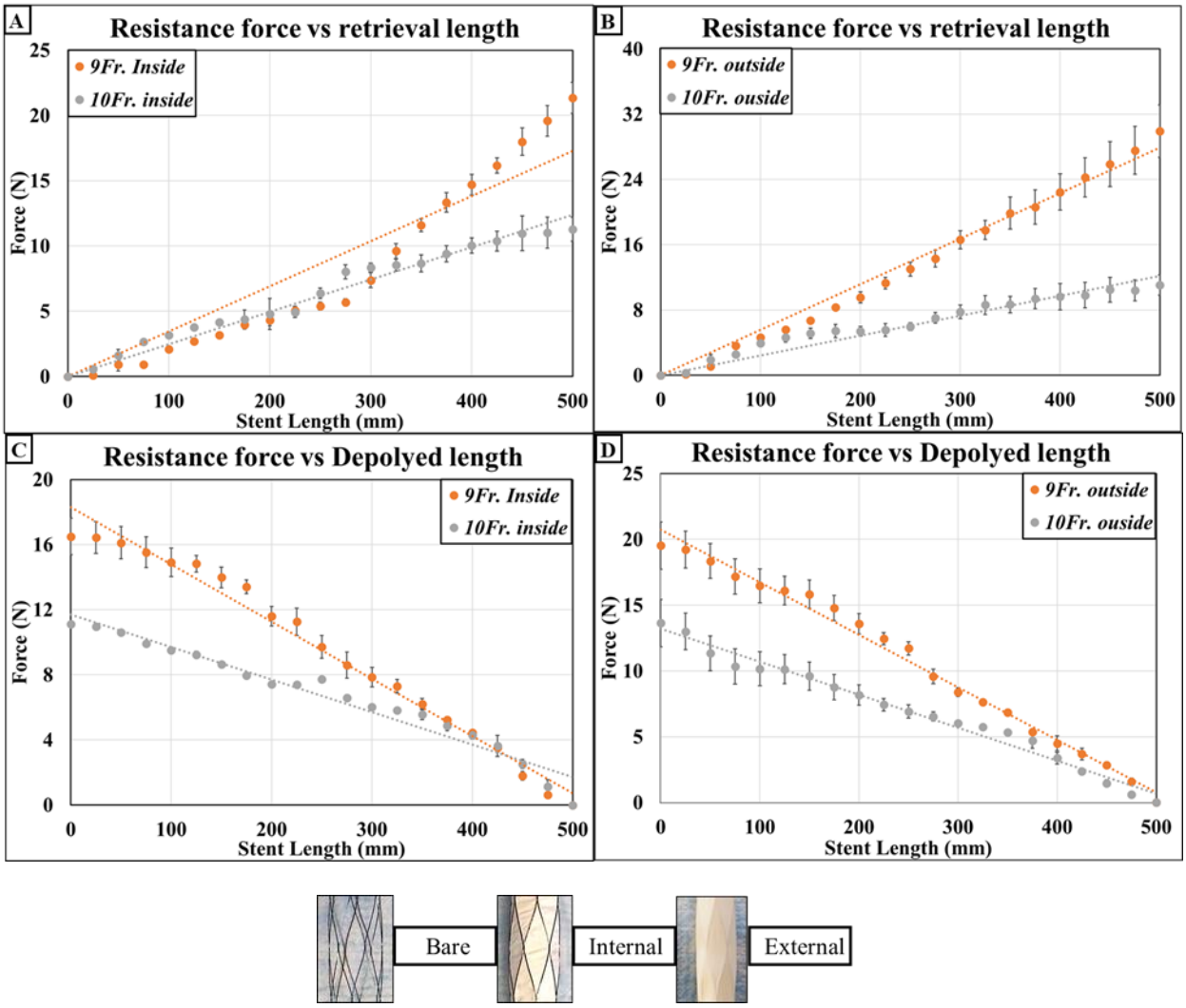

Figure 19 Resistance force for retrieval and deployment of the stent graft in the sheath. A) & C) are graphs that represent the retrieval and deployment resistive forces versus the stent graft length of internally attached ePTFE stent grafts in 9 Fr., and 10 Fr. sheaths. B) & D) are graphs that represent the retrieval and deployment resistive forces versus the stent graft length of externally attached ePTFE stent grafts in 9 Fr., and 10 Fr. sheaths.

Figures 20A & 20B compared the resistance forces of deployment and retrieval between different ePTFE configurations, bare (no ePTFE), internal ePTFE, and external ePTFE stent grafts. The bare case showed the lowest resistance force as less material is deployed or retrieved. For internal and external ePTFE cases, the same material is deployed or retrieved, however inside ePTFE showed less resistance forces. The outcome on resistance forces was investigated for using several retrieval speeds, and the slower speed 250 mm/min showed less resistance force, as shown in Figure 4.8C.

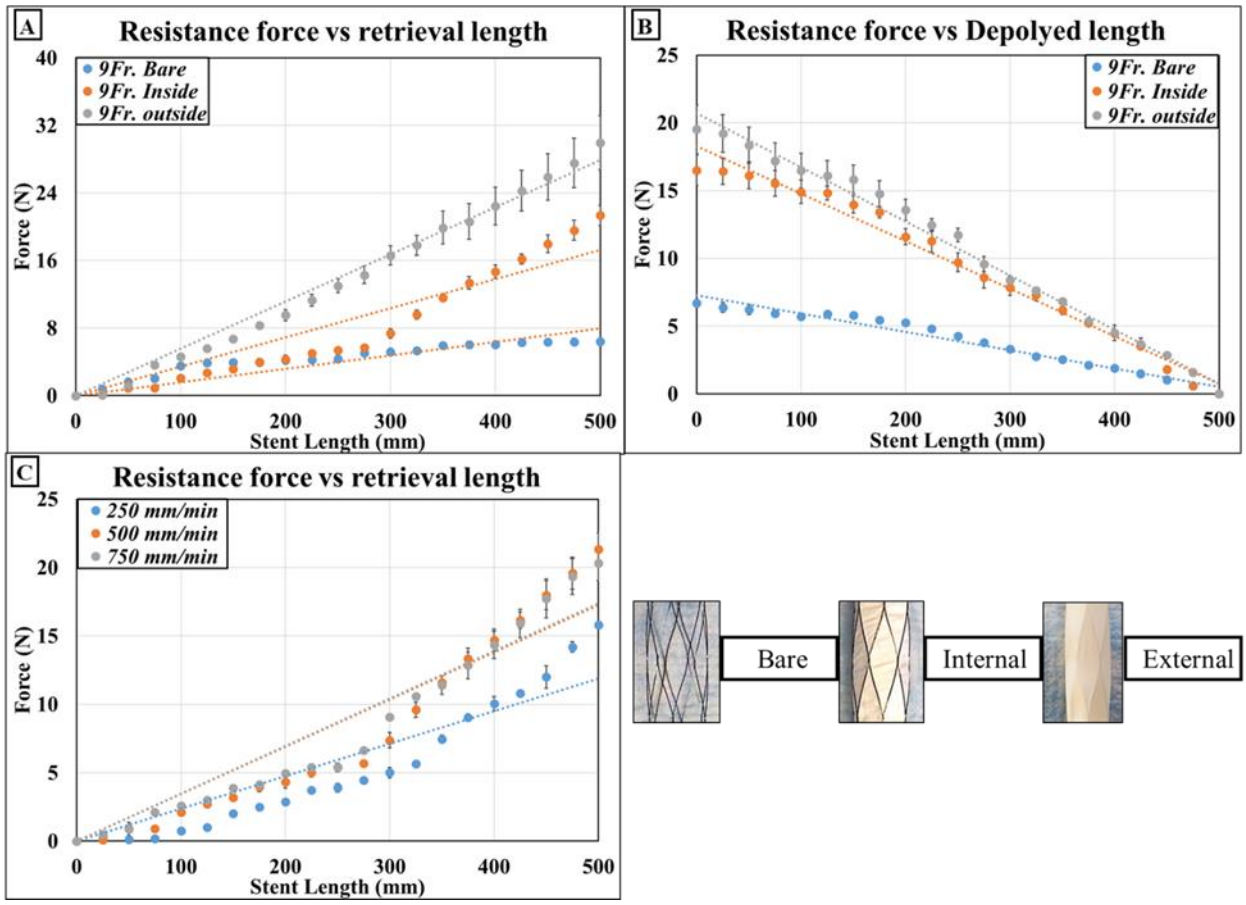

Figure 20 Resistance force for retrieval and deployment of stent graft on 9 Fr. sheath. A) & B) are the resistance forces versus stent length for stent grafts with different configurations of ePTFE, bare, internal, and external. C) Resistance force versus stent graft length for different capturing speeds, 250, 500, and 750 mm/min.

4.2.4 In Vitro Leakage Test for Different Type of Stent grafts

The ability of the stent graft to prevent leakage within a tubular structure is crucial for evaluating the performance of the stent graft. A swine aorta was extracted from Yorkshire pigs, and kept in 0.9% sodium chloride solution (Baxter, Deerfield, IL). The experimental setup is shown in Figure 21A. A mixture of glycerin and water (58.5:41.5% v/v; density, 1.16 g cm^3; dynamic viscosity μ, 4.0 cP) was used to simulate the viscosity of blood. The fluid was circulated using a pulsatile pump (Harvard Apparatus, Holliston, MA) at different pressures and flow rates. The flow rate was controlled by the pulsatile, and the solution pressure was measured using a pressure probe (PressureMATTM DPG, PendoTech, and Princeton, NJ). The solution was heated to 37°C using a water bath (ThermoFisher, Waltham, MA) to simulate the body temperature. The diameter of the distal end of the aorta was measured (left in Figure 21B), to manufacture a stent graft to cover the aorta internally. The aorta diameter was 20 mm. Two stent grafts were used to control the leakage through the aorta, the first device diameter was 20 mm, and the second diameter was 25 mm. The aorta used in the testing was 200 mm long, with internal diameters 20 mm on the top (proximal end to heart) of the aorta, 17 mm on the middle of aorta, and 13 mm on the bottom (distal end to heart) of the aorta. The aorta had several holes, as shown in Figure 21C. The aorta had 2 holes with 3 mm diameter, 1 hole with 5 mm diameter, and 2 holes with 6 mm. The leakage was recorded for uncontrolled leakage (without stent graft), and for the two stent grafts. The stent grafts used in all leakage tests are 300 mm long, 0.0155" wire diameter, 23 mm distance between welds and heat treatment 500 °C for 30 minutes. The backbones were covered with ePTFE externally as shown in Figure (21C).

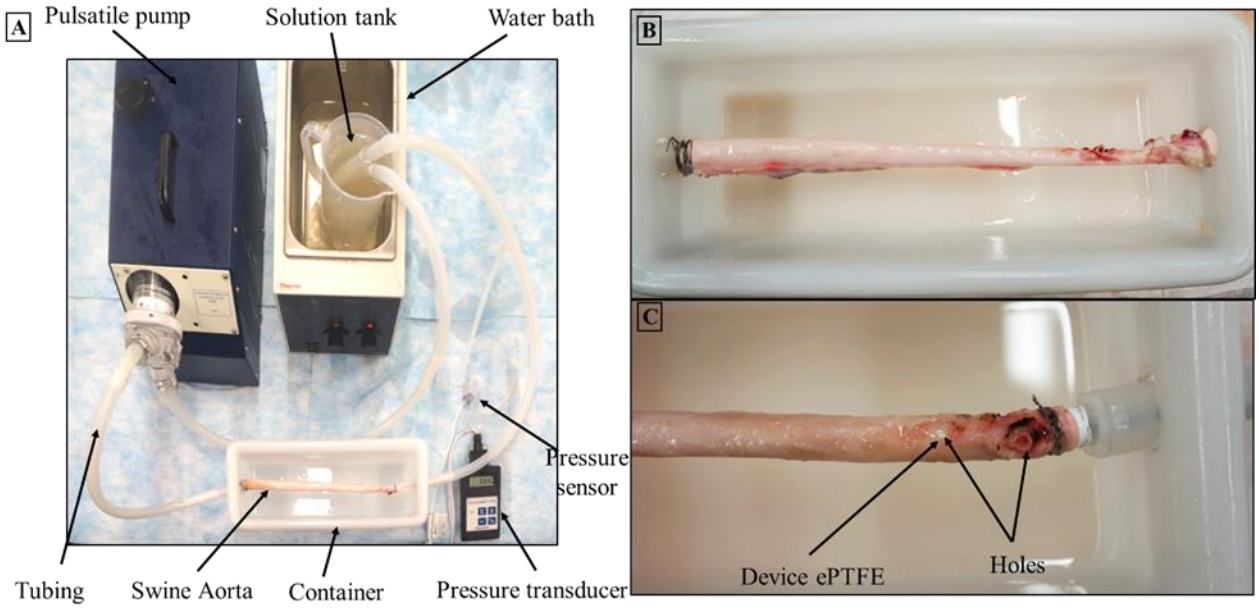

Figure 21 A) Experimental setup for leakage quantification between stent graft and swine aorta. The setup consists of a pulsatile pump, water bath and a tank of glycerin-water solution. Pressure sensor is attached to measure the solution pressure and recorded by pressure transducer. B) Close look for the swine aorta. C) An image for the stent graft deployed inside the swine aorta.

Leakage quantification is a critical parameter for successful device performance. The leakage was measured using an in vitro flow circulation that was equipped with the harvested swine aorta for evaluating the performance under different pressures and flow rates. The uncontrolled case, where no device is used, was compared with cases where 20 mm and 25 mm stent graft diameters are deployed inside the aorta. Figure 22A illustrates the results of leakage for pressures 85, 72.5, 60, and 52.5 mmHg, while keeping the flow rate at 2500 cc/min. The maximum leakage occurred in the uncontrolled cases, and with increasing the stent graft diameter, the leakage reduced. Also, the higher pressure of the fluid exerted showed a higher amount of leakage through the aorta. The effect of the flow rate was investigated, while fixing the pressure of the solution used. The leakage increased with higher flow rates, as well as the leakage decreased with using

larger stent graft diameter as shown in Figure 22B. This demonstrates that the stent graft can cover an injury and prevent simulated bleeding.

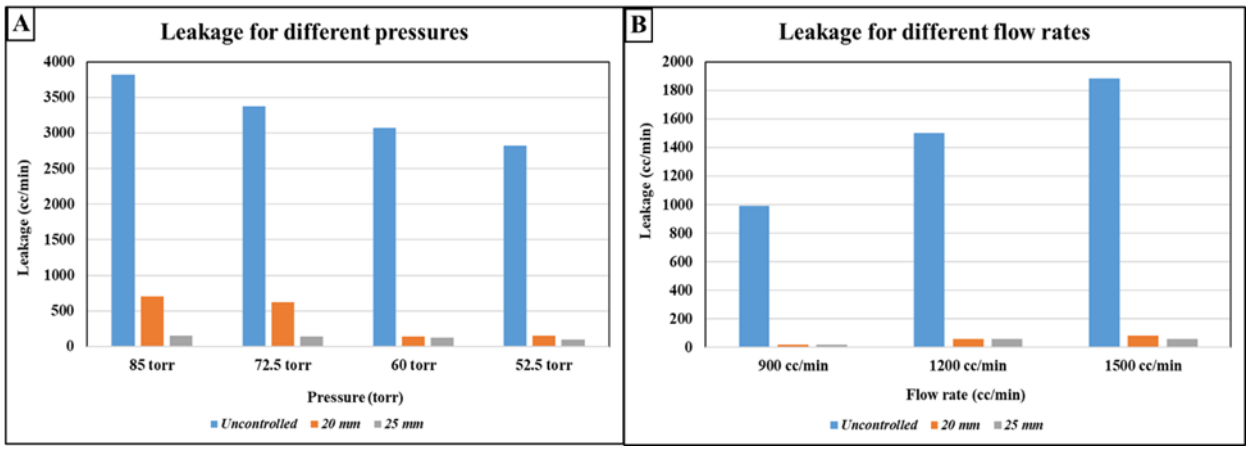

Figure 22 leakage measurement for swine aorta using different pressures and flow rates for uncontrolled, 20 mm, and 25 mm. A) Leakage measurements for different pressures, 85, 72.5, 60, and 52.5 mmHg with flow rate 2500 cc/min. B) leakage measurements for different flow rates, 900, 1200, and 1500 cc/min with pressure 25 mmHg.

Additionally, the potential leakage in different sizes of conduit has been evaluated as shown in Figure 23. These qualitative test results conducted with silicone tubing, show that the stent graft was able to prevent leakage even when the conduit was as much as 50% smaller than the stent graft size.

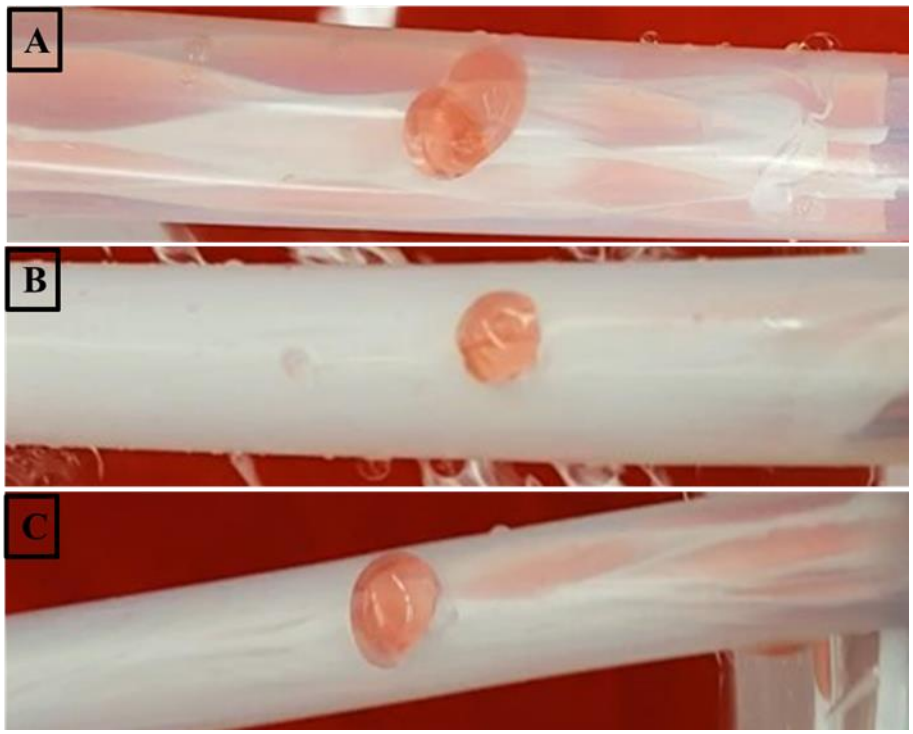

Figure 23 Qualitative representation of the leakage in the tubes with different diameter, which shows a 15mm stent graft provides seal of (A) an 8mm hole against pulsatile flow, (B) 75% of the stent graft, and (C) even 50% smaller.

4.3 Trauma stent graft development

4.3.1 Materials

The stent graft consists of 1) metallic stent backbone, 2) polymeric covering membrane, 3) extension wire, 4) nosecone, and 5) radiopaque marker. The backbone was fabricated from 0.0155" diameter superelastic Nitinol wire (NDC, Fremont, CA). A highly stretchable expanded polytetrafluoroethylene (ePTFE), (ZEUS, Inc., Orangeburg, SC, original wall thickness of 0.005") was used to cover the backbone. A super-stiff wire (Lunderquist® guidewire, COOK,

Bjaeverskov, Denmark) was used to extend the proximal end of the device both for device deployment and retrieval. A custom-built nosecone was directly connected to the backbone, which contains a floppy tip of guidewire and a tapered nosecone mimicking the dilator. A 20-micron thick Tantalum strip (GoodFellow, Coraopolis, PA) was used to fabricate radiopaque markers on the desired locations on the stent graft for the in vivo fluoroscopic guided endovascular procedure.

4.3.2 Stent Graft Fabrication Processes

Nitinol wires were joined by a precision micro laser-welding system (LZR-100; Sunstone Engineering, Payson, UT). Welding parameters were optimized, from previous results, in order to acquire the best material and mechanical properties of the structure for Nitinol wires with various thicknesses. The laser process parameters are 1.4 kW power, 0.7 mm spot size, 1ms time duration, 1Hz frequency, and rectangular wave. A machined aluminum mandrel based on the anatomy of the swine model was used to create the Nitinol backbone with the desired cylindrical geometry, where the external diameter of the mandrel corresponds to the deployed device diameter. The mandrel diameter was oversized by 25% to produce the oversized stent backbone for achieving sufficient radial force for the device. The mandrel with stent was heated up to 500°C by tube furnace (Lindberg/Blue M Moldatherm, Fisher Scientific, Pittsburgh, PA), then, the stent was rapidly cooled in water to 20°C in 30 seconds (quenching). Thermal treatment was performed to set the final shape of Nitinol wires with required superelastic properties, allowing relief of local stress concentration caused by welding.

Radiopaque markers were mechanically trimmed from the Tantalum strip with width of 1.0 mm and length of 10 mm. The markers were wrapped 5 times on the four different locations on Nitinol strut, such as a distal end, and proximal end. A nosecone was attached to the top end

(closer to the heart during stent graft delivery) after trimming from the delivery sheath dilator, and a floppy tip was subsequently connected on the top nose cone for smooth delivery. This system enables the sheath to navigate through the blood vessels smoothly without any pre-installed guidewire. An extra stiff Lunderquist guidewire was integrated with the device using a 4.0-5.0 size silk sutures (UNIFY®, AD surgical, CA) for the device delivery. The covering membrane, ePTFE (originally ID 0.394" +/- 0.03, wall thickness 0.005" +/-0.004) was stretched via ballooning and attached onto a Nitinol backbone using a biocompatible polymer adhesive internally or externally.

4.3.2.1 Nosecone Configuration Optimization

The nosecone has an essential role in delivering the stent graft, with maneuvering the collapsed device through the body arteries. The first prototype of nosecone was by extending the upper section of metallic backbone, and comprising them into small profile, as shown in Figure 24A, then attach the nosecone. However, due to profile comprising, the upper backbone diameter tends to have smaller diameter, and smaller radial force, which increases the leakage between the stent graft and artery lining. The nosecone attachment configuration was altered, into welding external Nitinol wires to the upper section, then attach the nosecone to the external wires, as depicted in Figure 24A. The metallic backbone was covered with ePTFE cover, as shown in Figure 24B, and the device, was used inside swine model. During the in vivo, the leakage continued through the upper section. After the surgery, the device was collected, and the external wires was bended from the aorta tortuosity and created a gap between the stent graft and the internal lining of the artery, as shown in Figure 24C. Also, by examining the device after the surgery, the polymeric cover was found separated from the metallic backbone, especially in the start of the upper section. The bleeding is assumed as consequence of the generated gap and the ePTFE delamination.

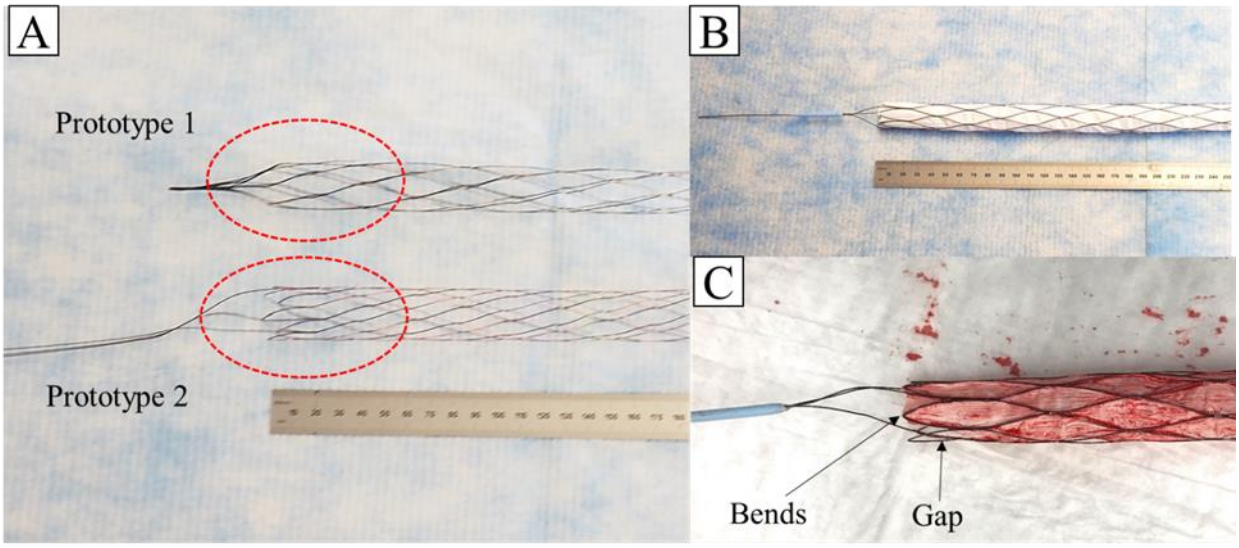

Figure 24 The first prototypes of nosecone attachment to the stent graft. (A) Image shows the 1st and 2nd prototypes of the nosecone attachment, either by extending the Nitinol wires, or welding extra Nitinol wires to the upper section. (B) Stent graft prototype using the 2nd prototype method of attaching the nosecone. (C) Post surgery image of the upper section of the stent graft, including the nosecone. The backbone diameter is shrank from the top and the ePTFE is separated.

Another issue appeared with older prototypes in the bends in the upper section of the device, shown in figure 24C. The bends are shaped by permanent plastic deformation of the Nitinol wires; however, after collapsing and deploying the device, these bends were distorted. To address these challenges, a new configuration was fabrication for the nosecone. First, the upper bends were removed completely, to avoid the bends distortion, as shown in Figure 25A. The nosecone was connected to external long 0.014" wire, which was welded to the lower section of the backbone, as shown in Figure 25B.

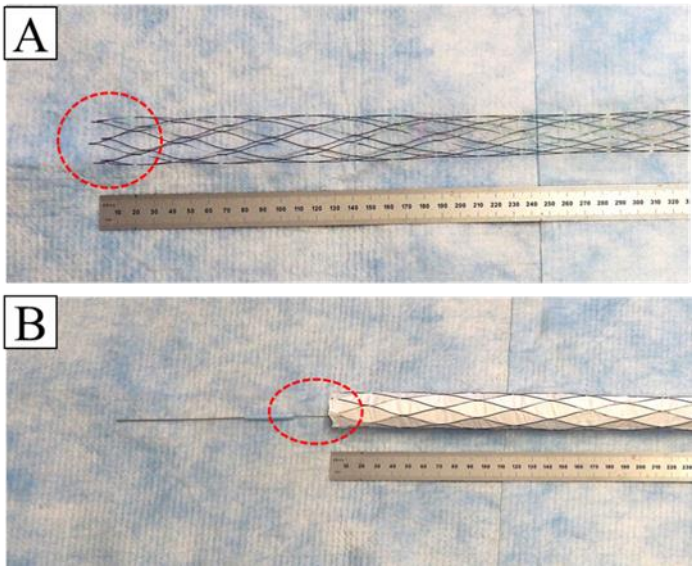

Figure 25 The new prototype for the upper section of the stent graft and nosecone. (A) The stent backbone after removing the upper bends. (B) The nosecone is connected to the stent graft via a Nitinol wire, welded to the lower section of the stent graft.

4.3.2.2 Polymeric Ends Fixation

The ePTFE fixation to the metallic backbone is crucial for the device's functionality, to ensure blood flow through the stent graft. After collecting the device after the swine studies, ePTFE cover was found detached from the Nitinol backbone, which compromised the device's performance. A new fixation was added to solve this problem, with gluing a thin 2mm width, and 50mm long to both Nitinol wire and the ePTFE cover. Figure 26A shows the polymeric fixation of the start of thoracic covering, while Figure 26B shows the fixation of the end of thoracic covering

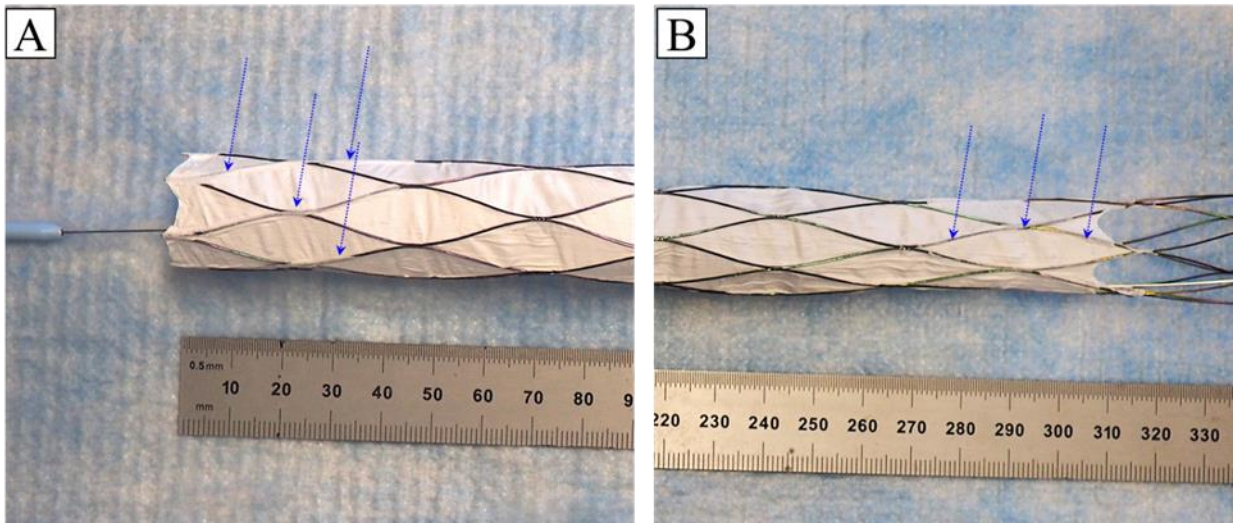

Figure 26 Images show the new fixations of the inside-ePTFE to the metallic backbone. Small pieces of thin ePTFE layer are glued to both the Nitinol structure, as well as the ePTFE cover. (A) The fixation of the start of thoracic covering. (B) The fixation of the end of thoracic covering.

4.3.2.3 A Manufactured Prototype

A functional prototype stent graft has been successfully manufactured using optimized conditions obtained from various in vitro mechanical experiments. Figure 27 shows the device image that is composed with a nosecone, first long PTFE covered region for thoracic covering, bare metal region for perfusion to organs, second short PTFE covered region for abdominal covering, and an extension wire for easy device delivery and retrieval process.

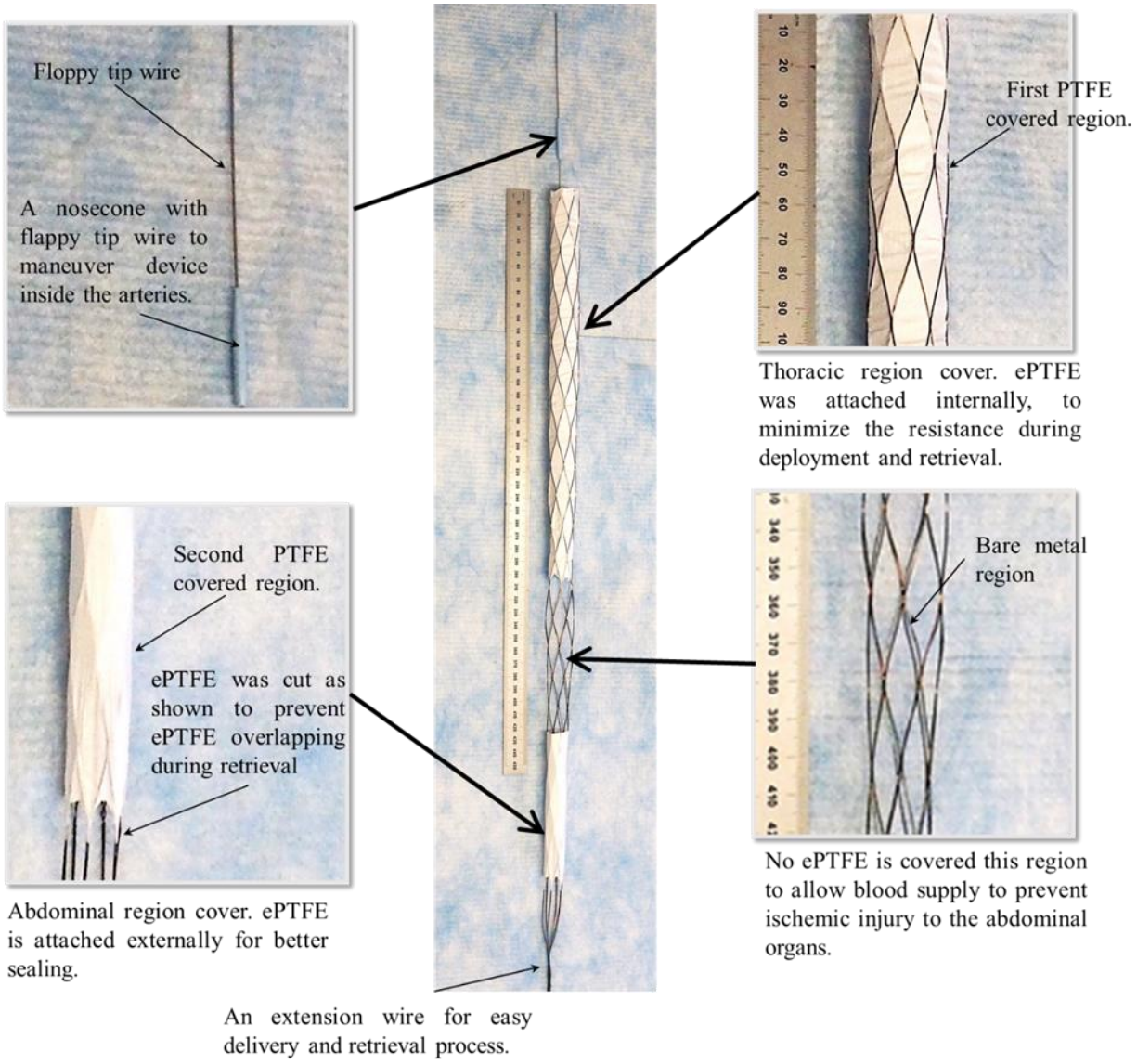

Figure 27 A prototype that contains a nosecone, two PTFE covered regions, bare metal region for perfusion and an extension wire for easy delivery and retrieval process.

4.4 In Vivo Tests

Yorkshire pigs 80 kg to 90 kg were obtained from Archer Farms, Inc. (Darlington, MD), and were placed under general endotracheal anesthesia, upon the approved IACUC protocol as part of University of Pittsburgh with inhaled isoflurane. Operative exposure was done to expose the aorta. In order to simulate the derangement of clotting after trauma, the animals were heparinized to overcome the rapid clotting occurring inside the porcine model. A 22 French dilator was used to make an injury in the aorta artery, then, a long 10 French sheath was used to deliver the device under fluoroscopic guidance. Several angiogram images were taken in different situations for the porcine model, an angiogram for injured thoracic aorta, and hemorrhage control for thoracic aorta. The injury was observed for 1 hour, and the leaked blood was qualitatively assessed. As a final step, the vascular sheath was advanced over the stent graft for collapsing and retrieval of the device. Figure 28A shows the bleeding occurred in the aorta, where the dark color represents the blood flow outside the artery walls. Figure 28B demonstrates the device deployment inside the artery, and the hemorrhage is controlled, as the blood flows normally through the artery.

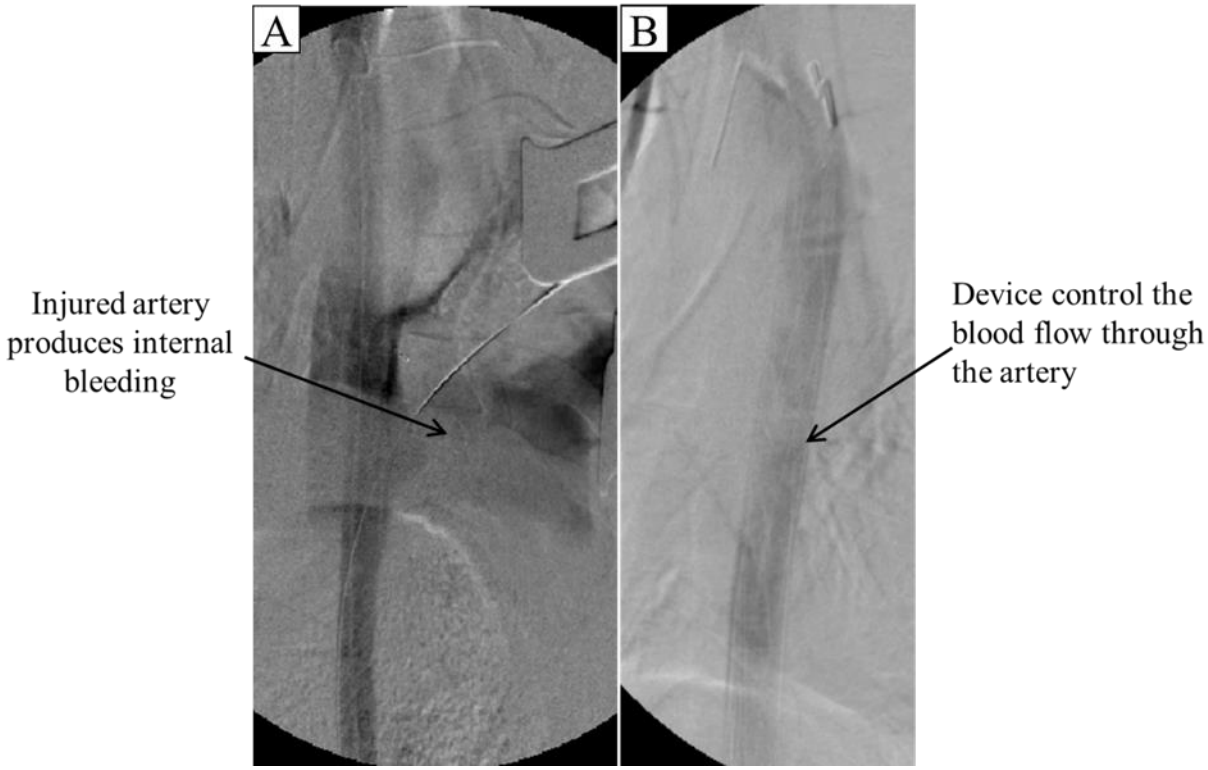

Figure 28 In vivo images to a swine subject for hemorrhage control using the stent graft. A) An image shows the hemorrhage, occurred in the thoracic region of the aorta artery. B) An image shows the hemorrhage control using the stent graft.

Figure 29A shows a gross look to the exposed injured artery. The ePTFE is depicted on the site of the injury, and no bleeding is shown around the injured artery. After the surgery observance, the device was removed from the swine, and checked for further investigation. The device was deployed in the lab, and the ePTFE was in good shape, attached to the metallic backbone as shown in Figure 29B. No broken welding was observed in the device.

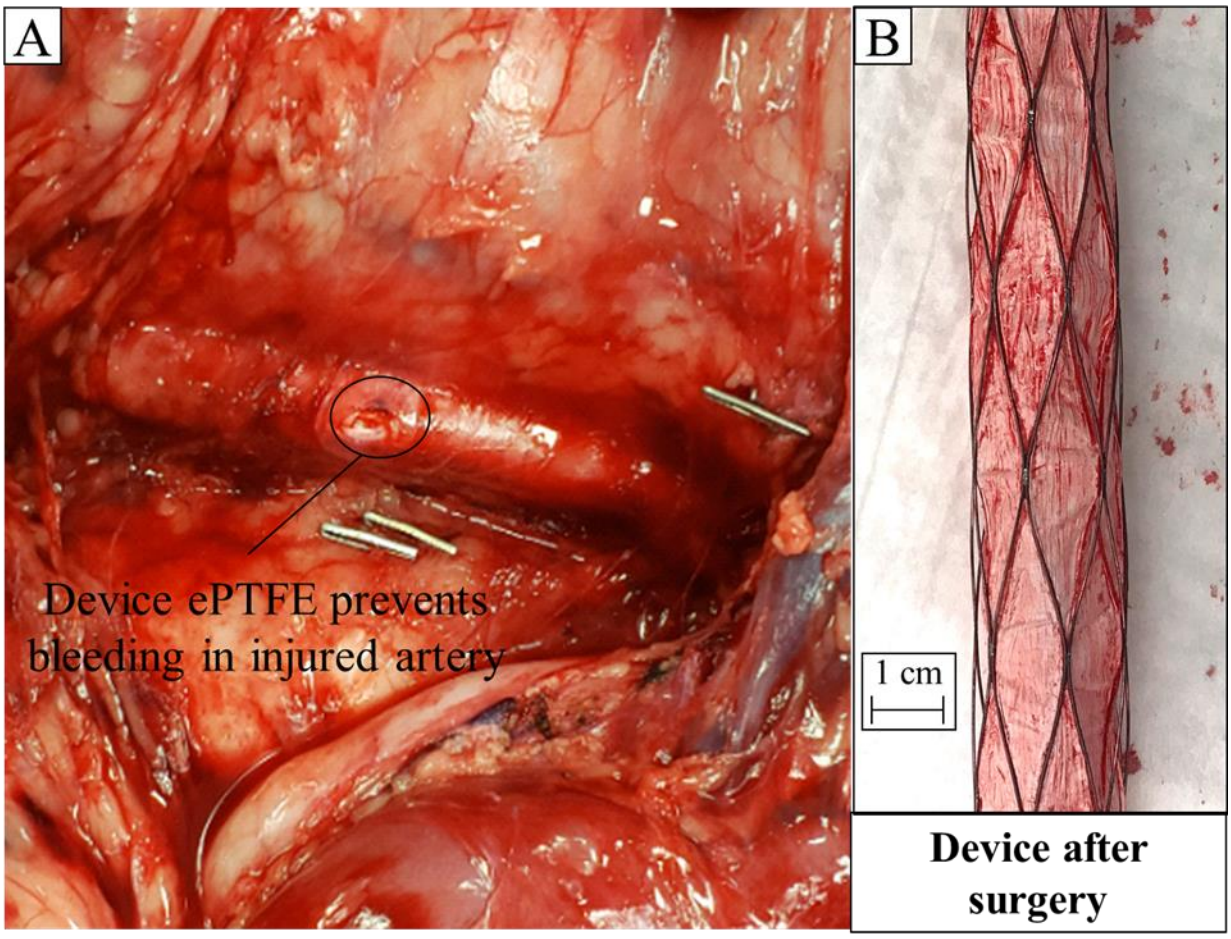

Figure 29 (A) Gross image of the stent graft deployed inside an injured artery. (B) The stent graft after the surgery, showing the laser welded joints, without any fracture, also, ePTFE is still fixed to the metallic backbone.

4.5 Discussion

The desired features of a new long stent graft, used for massive traumatic hemorrhage of the great vessels with limited experience and limited imaging, would be rapid delivery, the ability to control hemorrhage along the entire vessel even when the injury site is not known, and the ability to remove the stent graft at the time of a more focused permanent repair. This stent graft is intended for an ultrashort duration of implantation for emergent but brief control of life-threatening hemorrhage as a patient is transported between hospitals or even with a hospital, with an expected duration of less than one hour. Patients can bleed out in less than 15 minutes, which is why this stent graft is necessary and will only be in place until a qualified vascular specialist can permanently repair the injury (and remove the stent graft). Since the device is placed in the vascular system temporarily for only less than an hour, there would be no host tissue interactions with the stent graft.

While radial force is essential to prevent migration of a permanent stent graft, it was expected that less radial force would be needed for a temporary stent graft and in fact would improve the ability to more easily collapse the stent graft back into a sheath after use.

Radial force was evaluated using various geometric parameters of the metallic backbone, which can provide device's refinement strategies to customize the radial stiffness. The radial force assessment is associated with both the device migration and blood leakage performance; therefore, this study was first investigated. The radial forces of different Nitinol wire diameters (i.e., stent struts) showed that the radial force increased with larger Nitinol wire diameter. The radial force can be expressed as the radial stiffness multiplied by the deformation. By assumption that stent graft is roughly a cylinder tube, the radial stiffness was expressed to be directly proportional to tube thickness. As shown in [92], by increasing the wire diameter (in this case, the cylinder

thickness is equivalent to wire diameter), the radial stiffness increases, which increases the radial force.

The second parameter that determines the radial force of stent grafts is welding distance. The results demonstrated that the radial force increases by reducing the distance between welded joints, as the deformed length between welds decreases, which increases backbone's stiffness.

Oversized stent backbones can provide high radial force and potentially prevent device migration. Too many oversized devices could potentially create damages on the blood vessel wall or muscle, so it should be avoided. Therefore, fully deployed Nitinol backbones with various final diameters were tested for assessing radial force with different levels of oversizing effect. It was found that the backbones with larger deployed diameter exert higher values of radial force when the backbones crimped to the same diameter reduction percentage. Larger diameters need more radial displacement to achieve similar diameter reduction %, which requires more radial force applied on the larger diameter backbones.

Another unique parameter to determine the device's mechanical performance is thermal treatment that is used to fabricate shape-set Nitinol backbones. Shape-setting process of Nitinol governs the transformation temperature and final superelastic behavior at body temperature [33]. In order to relieve the stresses and preserve the final shape of the Nitinol wires, heat treatment should be higher than 450 °C and longer than 10 min. The thermal treatment conditions were studied to demonstrate the effect of shape-setting parameters on mechanical response of the metallic backbone. The annealing temperature alters the device's radial force, as the annealing temperature increases, the radial force increases. At higher temperature, more thermal energy is available to allow Ni and Ti atoms to diffuse [93], which affects the phase transformation temperatures and mechanical properties of material. For annealing temperature, the results showed

that 10 min and 15 min had lower radial force compared to other annealing times. These results can be understood as at the high temperatures and atoms diffusion, not enough time was allowed for nuclei to be precipitated [94], which affect the radial force. There is no significant effect for the number of cycles as the heat treatment conditions were identical.

The resistance force for deployment and retrieval of the stent graft is important for the device's performance assessment. The resistance forces were measured for bare metallic backbone without ePTFE covering, inside covering ePTFE, and outside covering ePTFE. The metallic backbones required less force for deployment and retrieval within different sheath sizes, as the metallic backbone radially compressed is the only material that is collapsed within the sheath. Therefore, the resistance force is relatively very low, as the friction is only generated between the internal surface of sheath and the Nitinol wire backbone only. There were increased resistance forces for the ePTFE covered backbones, either inside or outside covering, because the crimped ePTFE membranes along with the Nitinol backbone actually increase the total volume of the collapsed device. Additionally, the crimped ePTFE directly contact the luminal side of the delivery sheaths generating a much higher resistance. For these reasons, ePTFE covered backbones could not be deployed or retrieved with a smaller size sheath (i.e., 8Fr).

The resistance force for deployment and retrieval of the stent grafts decreased with using larger stent graft size, as the luminal space for the device inside the sheath becomes larger, which allows proceeding the stent graft easier. For inside and outside covering ePTFE attachment to metallic backbone, the outside covering ePTFE shows higher resistance both in deployment and retrieval. This can be understood as the contact area in case of inside covering ePTFE is the contact area of the metallic backbone, which was built up using thin Nitinol wires. However, for outside covering ePTFE, the contact area is for the cylinder-shape ePTFE, which is much larger compared

to the backbone contact area. Also, ePTFE is glued to the metallic backbone only on both ends in the case of outside covered ePTFE, which permits most of ePTFE to deform freely, so wrinkles formation was more common. These wrinkles increase the resistance significantly during pushing and pulling the stent graft within the sheath.

Leakage quantification is a crucial step to evaluate the device's functionality. In vitro tests with swine aorta were first conducted under several pressures while fixing the flow rate. Then, the device leakage was tested under different flow rates with a fixed pressure level. Physiological data such as pressure levels and flow rates obtained from swine tests were used in these tests. The mean blood pressure range was from 20 – 100 mmHg, and the average flow rate range was between 1 – 10 L/min. The results showed that the leakage increased for higher pressure and flow rate. The results indicated the importance of using oversized stent graft, especially on the ends. A 20 mm (no oversizing) and 25 mm (25% oversizing) diameter stent grafts were used, where the aorta maximum diameter is 20 mm. The minimum leakage was found for 25 mm diameter stent graft where, stent graft oversizing ratio is 25% which is the recommended oversizing ratio [95]. The stent grafts showed good control for the leakage, using the oversized stent graft.

Based on in vitro results for Nitinol structure, regarding geometric parameters, thermal conditions, and leakage results, a novel stent graft has been designed and fabricated for in vivo swine tests. There are no commercially available stent grafts covering the thoracic, visceral and abdominal aorta, simultaneously. As a result, the cumulative friction across an extremely long stent graft is a major consideration during deployment. In addition, commercial stents are designed for stepwise wire and catheter exchanges that are not practical for physicians inexperienced in endovascular procedure and certainly in emergency settings. The retrieval feature is also not available on any other commercial stent graft design. To address these challenging issues, a single-

body stent graft system has been studied and developed, which contains the integrated guidewire tip, nosecone, and delivery wire. Several unique design/fabrication techniques contribute significantly to the ease of deployment of this ultra-long design providing a distinct difference compared with commercial permanent stents or stent grafts. In vivo test results have shown the feasibility of using the device for bleeding control, developed in injured vascular systems. Gross look for the stent graft inside an injured artery, demonstrated safe handling for the hemorrhage with minimum leaked blood around the injured artery.

4.6 Conclusion

A novel extremely long stent graft has been manufactured using an optimized micro-laser welding technique and a unique attachment technique of the highly stretchable ePTFE tube. The radial force of the metallic backbone was comprehensively studied in terms of geometric parameters and heat treatment conditions. Wire diameter, laser welding distance, as well as deployed diameter can be manipulated to customize the radial force of the metallic backbone. Heat treatment conditions such as, annealing temperature and annealing time showed significant effect on the backbone radial force. Various forms of configurations for ePTFE covering onto a Nitinol backbone were utilized to accommodate the retrieval and deployment resistance level, especially for the long stent graft. In vitro leakage measurements demonstrated the capability of 25% oversized stent graft to control bleeding in swine aorta. Through in vivo tests in swine models, the novel developed stent graft, with retrieval compatibility, could be effective for torso hemorrhage control.

5.0 Design Validation of a Novel Organ Perfusion Stent (OPS)

5.1 Introduction

Shortage of healthy donors' organs are increasingly becoming the main problem facing organ transplantation for those, who are in severe need for their life. In the United States, there are around 120,000 patients on the waiting list for a solid organ transplant, 95% of them need organs from the abdominal region, such as liver, kidney, and pancreas [96]. The available organs are limited to 25% of the needed cases, which means that only 1 of 4 would receive one. Most of the transplanted organs (80%) are taken from deceased donors, however, the greatest hurdle is the existence of periods of insufficient blood flow, which causes organ injury [97]. Ideally, the organs are recovered from living donors or donation after brain death (DBD), as organ recovery is performed under perfect conditions for organ preservation. As the collective number of living donors and (DBD) has plateaued recently [98], the organ pool should be expanded to meet the current shortage of healthy organs.

In the past decade, some trials have been performed to recover organs from alternative donor groups, donation after cardiac death (DCD), where organs can be taken from patients with non-recoverable injuries [99][100]. After the family's consent for donation, DCD donors are disconnected from cardiopulmonary life support, consequently, the heart enters the agonal period as the heart begins to fail. In the agonal period, the blood pressure and oxygenation fall, as shown schematically in Figure 30A, which cause irreversible ischemia organ failure. The standards indicate that the organs should be discarded if the agonal period exceeds 30 minutes for liver and

40 minutes for kidney. Therefore, minimizing the ischemia time, where the organs are not supported with enough oxygenated blood, is crucial to increase the chances of organs recovery.

Many approaches were used to improve the quality of the recovered organs in DCD patients, either by using an extracorporeal membrane oxygenation (ECMO) to resuscitate DCD organs, or perfusion oxygenated blood to the organs during the agonal period. By using (ECMO) before the cardiac death, it would not allow the heart to die normally, as (ECMO) is considered life support equipment. Another form of (ECMO), is using a balloon that prevents the blood reach to the heart and brain, while using the life support machine; however, this presents a lot of ethical challenges that must be respected. The ethical problem arose as the blood perfusion can cause stress on the heart that can accelerate cardiac death [101–103], which is forbidden by the ethics of organ donation. Also, open surgery is not permitted, as no surgery can be done until the patient's heart has died.

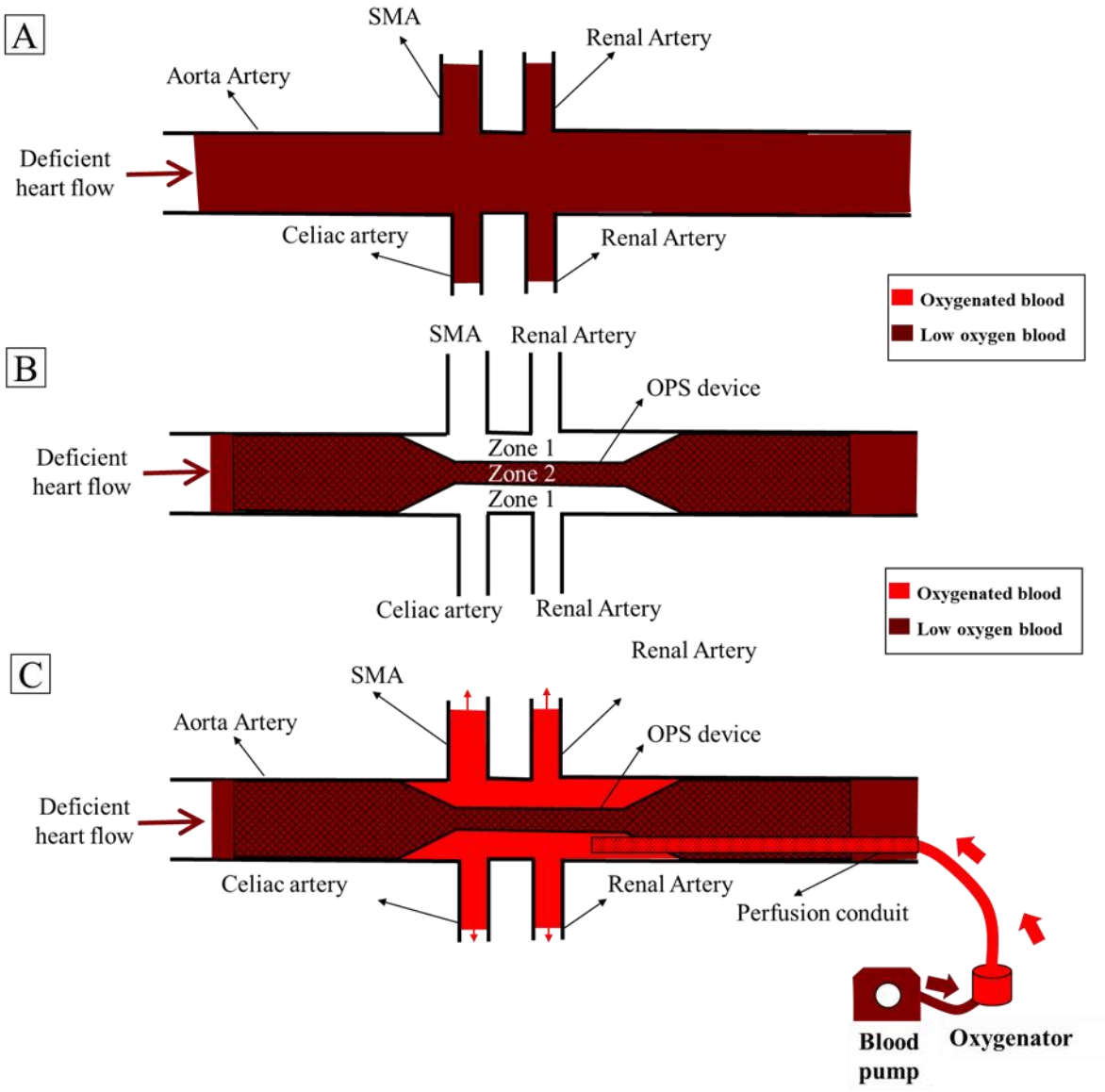

Figure 30 Schematic drawing showing the functionality of OPS inside the aorta artery. (A) Schematic shows the low oxygen flow to the main arteries in the abdominal region, causing ischemic injury. (B) OPS is deployed inside the aorta artery, to isolate the abdominal arteries from the cardiac flow, and divide the artery into 2 zones. (C) A perfusion conduit is connected to zone 1, which is connected to an external source of oxygenated blood, to deliver the necessary blood supply to the organs.

More recently, a unique device, dual chamber stent graft, has been developed, by this research group, to separate the abdominal (i.e., organs) blood flow from cardiac flow. As shown in Figure 5.1B, the device is used to isolate the cardiac flow from the abdominal organs, creating two zones, one for the cardiac flow, and the other for the organs perfusion. This device can effectively deliver the oxygenated blood from the ECMO only to the abdominal organs without increasing cardiac burden [104], by supplying the blood only to the abdominal organs as shown in Figure 30C. While the first demonstration has successfully been achieved using commercially available stent grafts, lower profile and fully retrievable stent graft is urgently needed to increase the number of available organs from the donation after cardiac death. A cylindrical shape of stent graft can be fabricated via a precise laser cutting of the metallic tubes and wrapping of ePTFE or Dacron polyester. However, dual chamber stent graft has complex geometry, therefore, a micro laser-welding technique would be one of the best fabrication methods for creating the metallic backbone.

5.2 Methods and Results

5.2.1 Radial force measurement

5.2.1.1 Computational modeling of the radial force via finite element analysis (FEA)

Finite element analysis was used to calculate the radial force, exerted by the Nitinol backbone, when the stent deforms radially. Computer-Aided design software (SolidWorks) was utilized to draw the patterns of stent structure as shown in Figure 31A. The stent models had 0.4 mm thickness, 25 mm diameter, and 50, 75, 100, and 125 mm lengths. The CAD model was

imported to a finite element software package (ANSYS) for structural analysis. Using ANSYS, the boundary conditions were applied to mimic the experimental setup for radial force, discussed in the next subsection. A pressure load of 65000 bar was applied on the central portion of the stent (25 mm length), and fixed support was applied at specific regions of the stent, as shown in Figure 31B. The Nitinol behavior was modeled using the built-in superelasticity module of ANSYS, where the material pseudoelasticity was modeled as shown in Figure 31C. The numerical values of Nitinol properties were adopted from [105]. This study was used to calculate the effect of the metallic backbone length on the radial force, as well as the Von-Mises stresses due to different values of diameter reduction %.

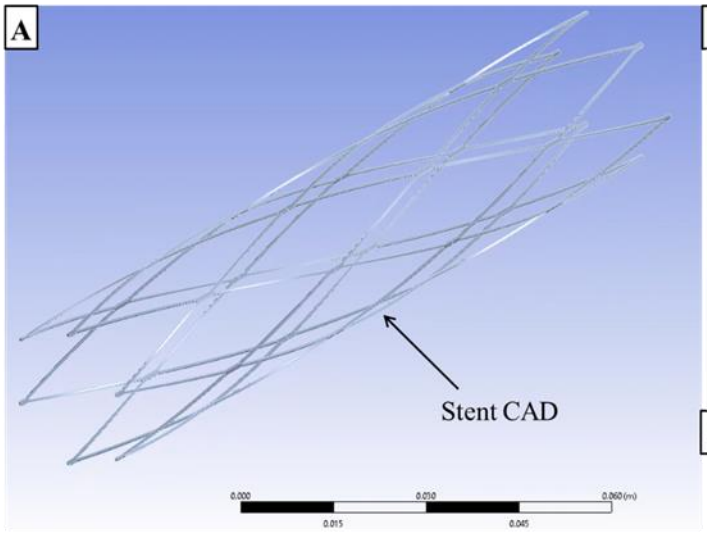

D

Material parameter	Value
E(GPa)	**60**
ν	**0.3**
σ^s_{AM} (MPa)	**346**
σ^f_{AM} (MPa)	**365**
σ^s_{MA} (MPa)	**83**
σ^f_{MA} (MPa)	**57**
ε_L	**0.063**
α	**0.09**

Figure 31 Finite element analysis of radial force of metallic backbone. A) Stent CAD, showing the diamond shape of the stent. B) The boundary conditions applied to the stent. The stent is fixed from the bottom, and pressure is applied to the center of the stent. C) Table mentions the values of parameters used in the simulation. D) The stress-strain response of superelastic Nitinol.

Computational analysis was used to calculate the effect of the metallic backbone (upper and lower seal) length on the radial force exerted by the seal, as well as the maximum Von-Mises stress due to diameter reduction. The finite element analysis showed that the radial force increased for longer seal length to be around 8 N for 125 mm seal length, at 38% diameter reduction as shown in Figure 32A. The radial force for 50 mm seal length is approximately half the radial force for 125 mm seal length. For Von-Mises stress results, the maximum stresses occurred for 75, 100 and 125 mm seal length, with values around 525 MPa as shown in Figure 32B. These results

showed that 125 mm seal length can provide higher radial force with similar values for maximum Von-Mises. Figures 32 C-F showed the stent deformation, when a local pressure is applied on the middle of the stent, with lengths 50, 75, 100, and 125 mm, respectively. For 50 mm seal length, the local pressure deforms the whole stent length, however, the deformation became more locally with increasing the stent length, until reaching 125 mm seal length, where the stent ends kept their initial shape.

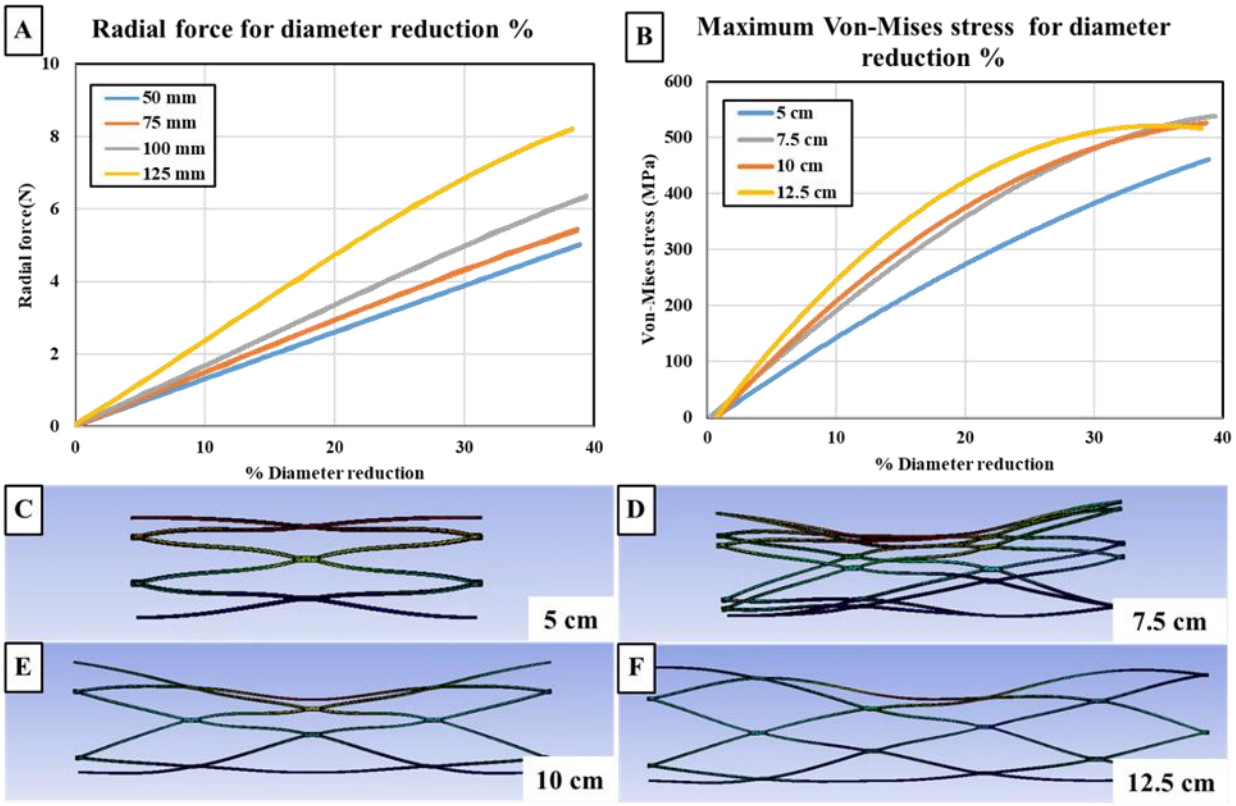

Figure 32 Computational results for finite element model. A) The radial force versus diameter reduction % for different stent lengths. B) The maximum Von-Mises stress versus diameter reduction % for different stent lengths. C-F) are the pictures of stent deformation when a local pressure is applied on the middle of the stent, for 5, 7.5, 10, and 12.5 cm.

5.2.1.2 Measurement of the radial force

Effect of the upper and lower seal length on the radial force of Nitinol backbone was characterized quantitatively using a mechanical test system (FLC-5E, Starrett, MA). Radial forces were measured by the means of crimping load applied on the central portion of the backbone, similar to the group work in published paper [68]. Using laser welding machine, several prototypes of Nitinol backbone were manufactured with 50, 75, 100, and 125 mm lengths for the upper seal, and 25, 50, 75, and 100 mm lengths for the lower seal as shown in Figure 33A. Closer looks for the upper and lower seals are shown in Figures 33B, and 33C, respectively. The central crimping of the backbone was done using a Dacron strap (Sailrite Enterprises, Inc., IN), which was fixed to a stainless steel rod, and wrapped around the Nitinol backbone as shown in Figure 33D. The other Dacron end was attached to the mechanical testing machine using a fixture with a 5N load cell. The load cell is connected to a machine computer to record the hoop force applied on the stent with respect to the displacement. The hoop force is multiplied by $2*\pi$ to calculate the radial force [90]. The experimental setup was used for upper seal, and lower seal, as shown in Figures 33E and 33F, respectively. The results were plotted as radial force with respect to the diameter reduction % for different upper and lower seal length.

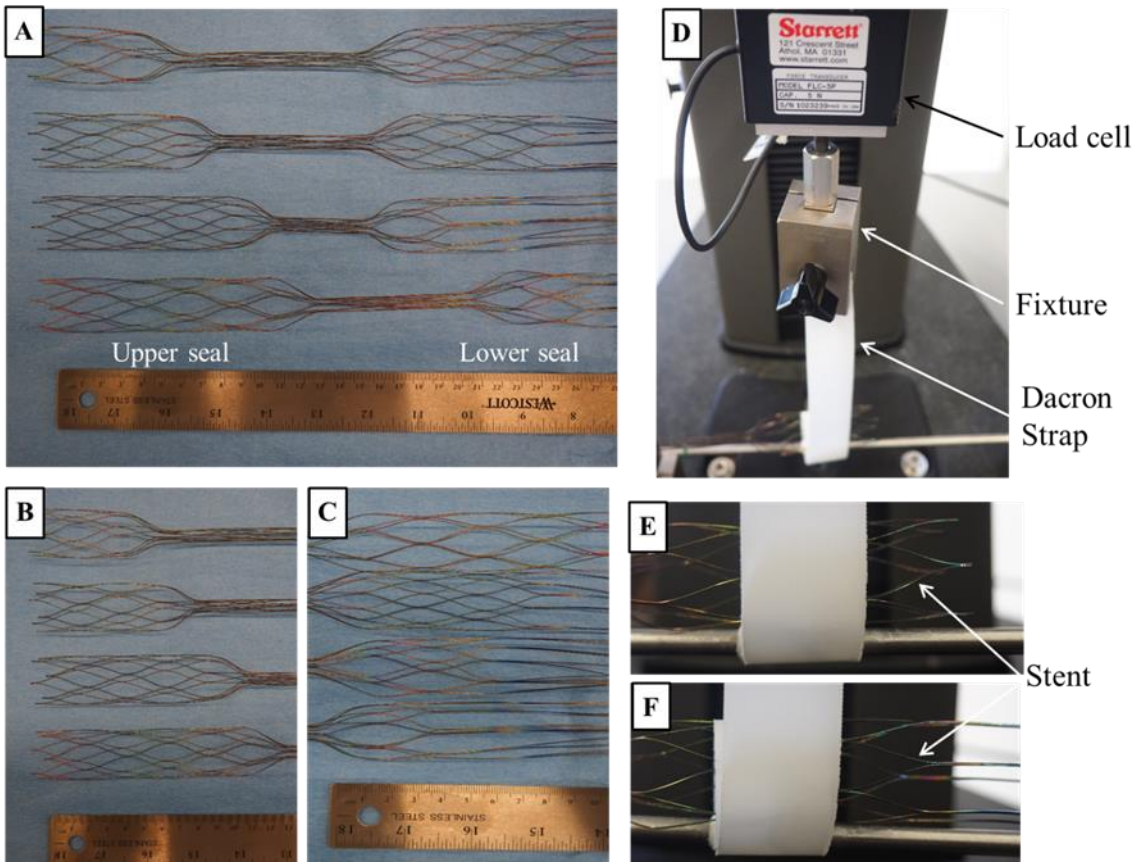

Figure 33 Experimental measurements of radial force of the Nitinol backbones. A) Stents with different lengths of the upper seal, perfusion length, and lower seal. B) Upper seal with four different lengths, 5, 7.5, 10, and 12.5 cm. C) Lower seal with four different lengths 2.5, 5, 7.5, and 10 cm. D) An image for the experimental setup of the testing machine for radial force measurements. E) & F) Dacron tape used to apply radial force on the upper and lower seal, respectively.

The radial force was measured using the testing machine for the upper and lower seal with different lengths. Figure 34A shows the radial force recorded for different diameter reduction % of the upper seal with lengths 50, 75, 100, and 125 mm. The radial force exposed, like computational results, linear trend for the relation between the radial force and diameter reduction%. The maximum radial force was 7 N for 100 mm and 125 mm upper seal length at 38% diameter reduction%. The radial force for the lower seal is demonstrated at Figure 34B, where the

maximum radial force was 7N for 75, and 100 mm seal length. The experimental results revealed that the radial force exerted by the lower seal is like the upper seal radial force, with shorter lengths for the lower seal. These findings were used for designing and manufacturing the prototype for the swine in vivo study.

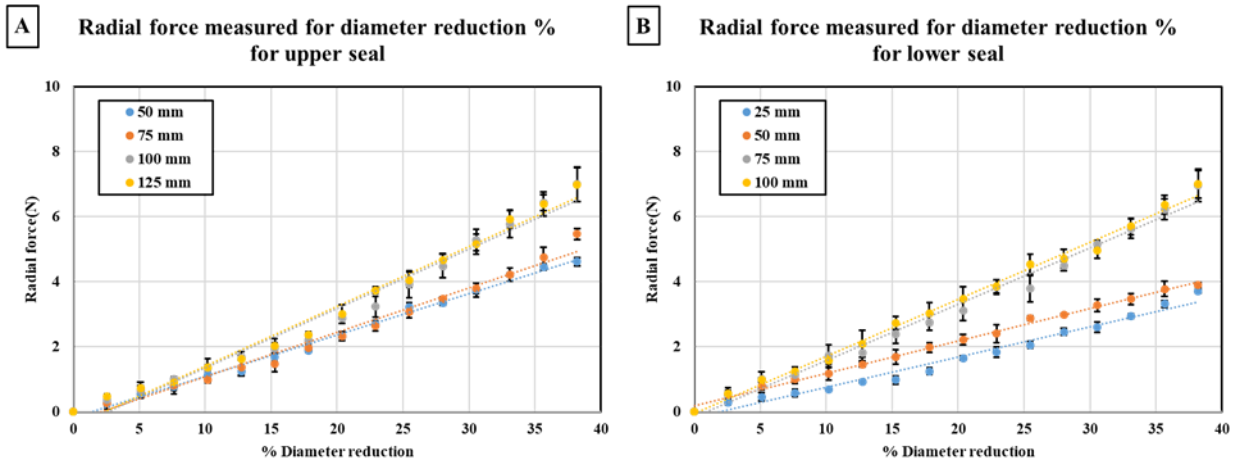

Figure 34 Experimental results of the radial force. A) The radial force versus diameter reduction % for upper seal. B) The radial force versus diameter reduction % for lower seal.

5.2.2 In vitro flow dynamics study

The main purpose of the organ perfusion stent (OPS) is to deliver well-oxygenated blood to the abdominal organs. To quantify the device performance, an in vitro experimental model was fabricated to show the functionality of the device and characterize the factors affecting the amount of blood delivered to the main abdominal organs. A pulsatile pump (Harvard Apparatus, Holliston, MA) with a controllable flow rate, was connected to the model input to circulate a flow mixture of water and glycerin (58.5:41.5% v/v; density, 1.16 g cm^{-3}; dynamic viscosity μ, 4.0 cP) to simulate the viscosity of the blood. A schematic for the experimental setup is shown in Figure 35.

A pressure sensor (PendoTech, Princeton, NJ), was connected to the model input, to measure the flow pressure. CT scans were acquired from the clinical collaborators in order to build a 3D model for the aorta with the main outlets. This model was printed using a 3D printer (MakerBot Replicator, Brooklyn, NY), then was inserted in a plastic container, where silicone elastomer (182 SIL ELAST KIT, Dow Sylgard, DOW, Midland, MI) was poured to cover the 3D printed aortic model. The silicone was left to cure for 4 hours, then the 3D artery model was removed to create the hollow space inside the silicone with similar dimensions of the aorta artery. The aorta silicone model has one input and six outputs, 2 iliac arteries, celiac trunk, superior mesenteric artery (SMA), and left and right renal arteries. Every abdominal output was connected to a jar to calculate the average flow rate, which was measured by recording the volume change after 1 minute.

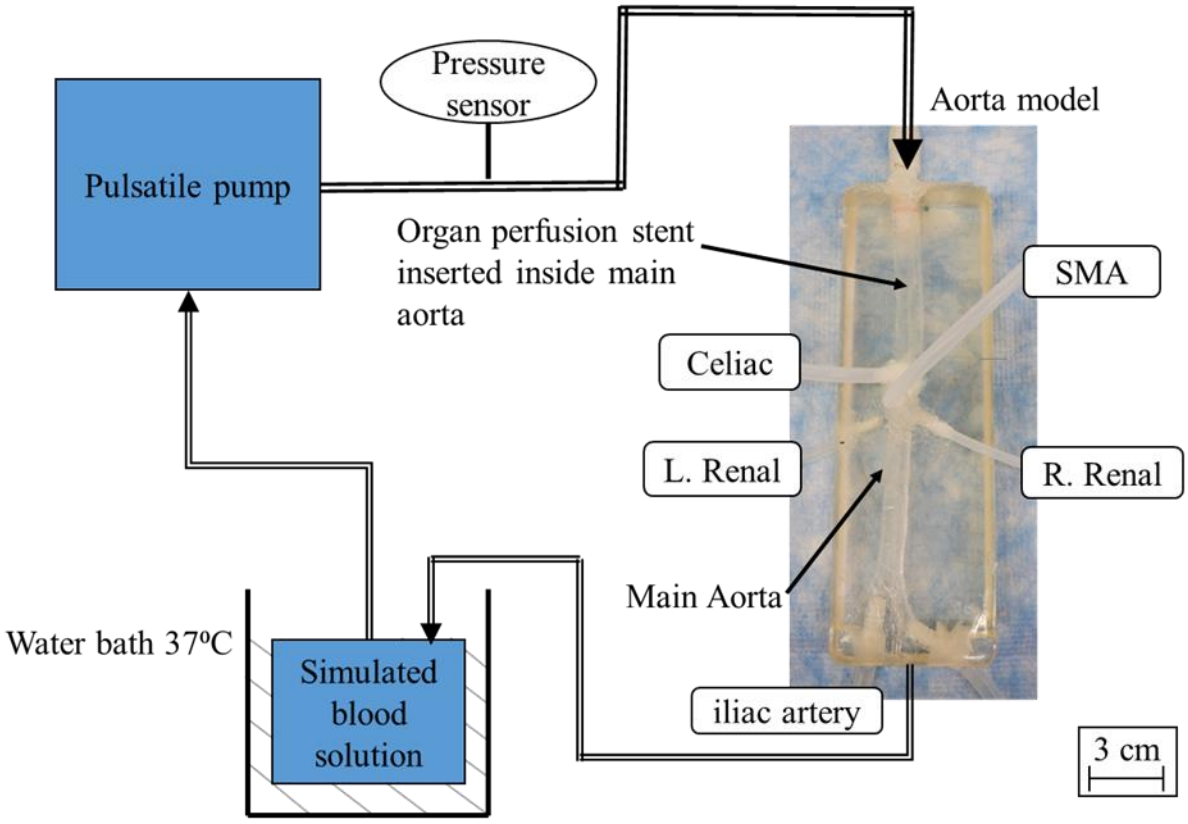

Figure 35 Schematic drawing for the experimental setup for flow rate measurements. The Aortic model used for in vitro flow rate measurements. The flow is injected from the left using a pulsatile pump. The model has six outputs, SMA, two renal arteries, and two iliac arteries.

5.2.2.1 Effect of perfusion length on cardiac flow rate

The stent graft reduced the lumen of the aorta model affecting the cardiac flow rate through the anatomical model. To quantify this effect, the cardiac flow rate was measured without any stent graft, and with different lengths of perfusion. The pulsatile was controlled to give a range of pressures from 40 mmHg, to 120 mmHg. The flow rate was measured for perfusion lengths 50, 75, 100, and 125 mm. The results were plotted as the cardiac flow rate with respect to the flow pressure, without stent, and for different perfusion lengths. The experimental setup for flow rate measurement was used to characterize the effect of the OPS dimensions on the blood flow rates through the device and to the abdominal organs. Figure 36 shows the cardiac flow rate inside the

artery, with and without the stent graft. The cardiac flow rate without inserting OPS is demonstrated at Figure 36A, where the flow rate increased with increasing the fluid pressure. The maximum flow rate was 2500±40 ml/min at 120 mmHg fluid pressure, which is like the physiological ranges of the blood inside the human body. After inserting OPS, the cardiac flow is reduced between 30-40% depending on the length of perfusion as shown in figure 36B. The longer perfusion length, the lower cardiac flow rate was, to be minimum at 125 mm perfusion length with 1560 ml/min.

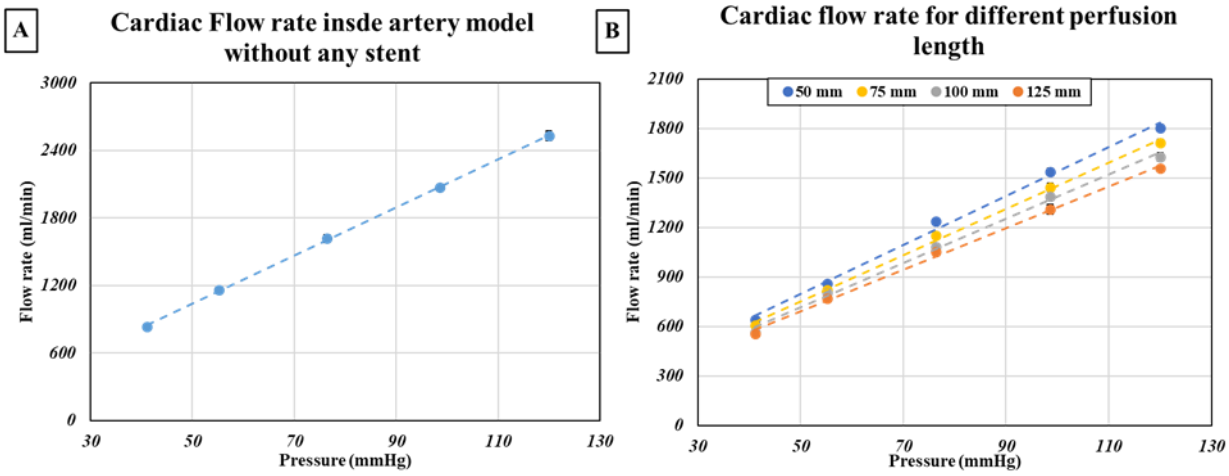

Figure 36 Cardiac flow effect after inserting the OPS inside the aorta model. A) Cardiac flow rate without OPS. B) Cardiac flow rate after OPS placement with different perfusion lengths.

5.2.2.2 Flow rate measurements of perfusion to the abdominal organs

Keeping enough flow to abdominal organs is essential to protect them from ischemic injuries, which will make the organs unsuitable for transplanting. The impact perfusion length, perfusion output, perfusion sheath size and perfusion sheath length was measured on the amount of flow, delivered to celiac, SMA, left and right renal arteries. The effect of perfusion length was measured for 50, 75, 100, and 125 mm lengths with fixing the sheath size 10 Fr, the location of

perfusion is in the middle, and the perfusion length was 600 mm. The impact of perfusion locations, proximal, middle, and distal to the heart, was measured on the flow rate delivered to the organs, where the perfusion length was 125 mm, sheath size and length were 10Fr. and 600 mm, respectively. For the perfusion sheath parameters, the effect of the sheath sizes, 7Fr., 8Fr., 9Fr., and 10Fr., was measured where the sheaths sizes were 600 mm. The perfusion length was 125 mm, and the perfusion location was in the middle. Finally, the impact of the perfusion sheath lengths, 300, 400, 500, and 600 mm was investigated for the 10 Fr. sheath, 125 mm perfusion length, and the sheaths outputs were in the middle of the perfusion region. The flow rate result was recorded for every artery output for different perfusion conditions. The fluid perfusion to the abdominal organs is the most crucial performance parameter to evaluate the organ perfusion stent. The perfusion was achieved via sheaths with different sizes and lengths. The maximum flow rate reached the celiac artery, while the minimum flow rates were delivered to the renal arteries. Figure 37A displayed the effect of the sheath sizes, 7, 8, 9, and 10 Fr. on the perfusion to the abdominal organs. The flow rate for 7Fr. sheath was minimum for all arteries, while the maximum flow rate was attained by 9 and 10 Fr. sheath. The maximum total flow rate was 750 ml/min, where the flow rate for left renal artery was 125 ml/min, right renal artery was 160 ml/min, SMA was 175 ml/min, and celiac artery was 290 ml/min. The impact of the perfusion sheath length was studied as shown in Figure 37B. The shorter the perfusion sheath, the more flow rate can reach to the abdominal organs with maximum total flow rate 815 ml/min for 400 mm sheath length. Using the shorter sheath, the left renal flow was 140 ml/min, right renal flow rate was 180 ml/min, SMA was 185, and celiac artery flow rate was 310 ml/min.

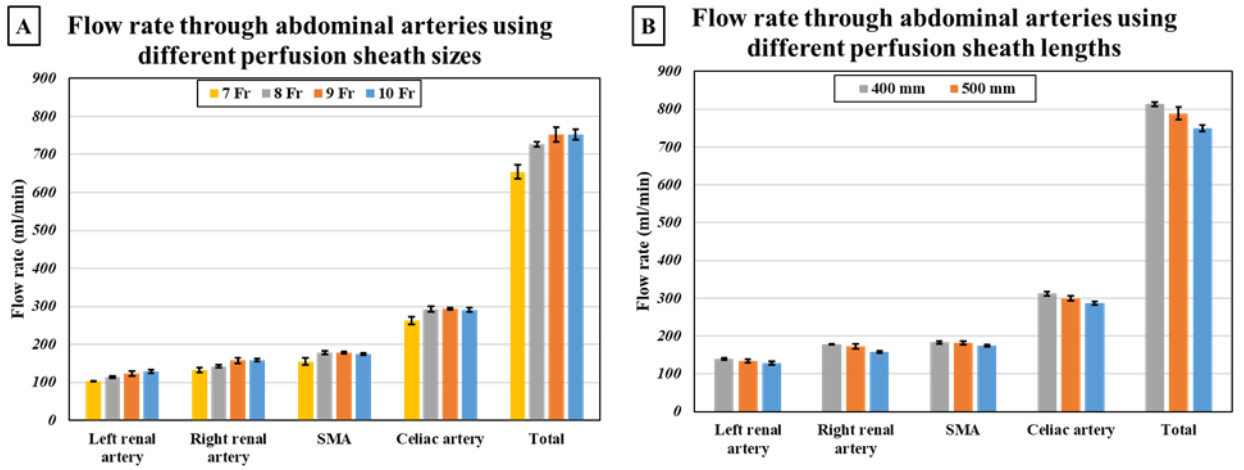

Figure 37 Effect of perfusion sheath on the perfusion flow rate to the abdominal organs. A) Flow rate through abdominal arteries for different perfusion sheath sizes. B) Flow rate through abdominal arteries for different lengths of perfusion sheath.

Also, the effect of the perfusion length on perfusion to the abdominal organs was investigated. Four perfusion lengths 50, 75, 100, and 125 mm, were studied to show the role of perfusion length. Figure 38A showed that the shorter the perfusion length, the more flow rate achieved to the abdominal organs. The maximum total flow rate was 820 ml /min, which was acquired from 50 mm perfusion length. The flow rates through left renal, right renal, SMA, and celiac arteries were 140, 180, 190, and 310 respectively. The perfusion output location effect was examined on the perfusion. The maximum perfusion was achieved from the distal to the heart location, with total 770 ml/min, left renal 120 ml/min, right renal 155 ml/min, SMA 195, and 300 ml/min for the celiac artery as shown in Figure 38B.

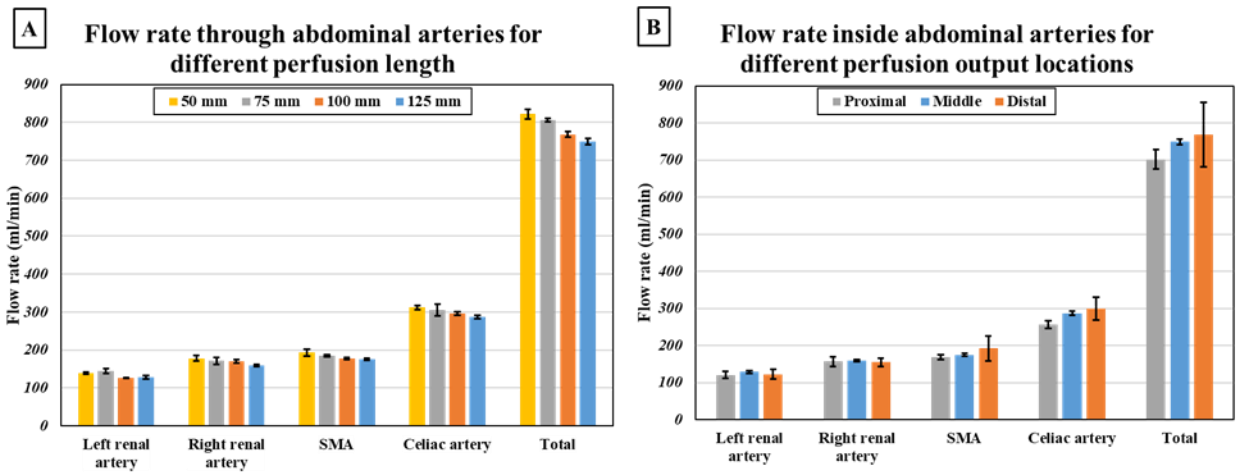

Figure 38 Effect of perfusion region parameters on the perfusion flow rate to the abdominal organs. A) Flow rate through abdominal arteries for different perfusion length. B) Flow rate through abdominal arteries for different locations of perfusion output.

5.2.2.3 Leakage of perfusion fluid to the cardiac flow

The stent graft should isolate the perfusion flow from the cardiac flow, not to disrupt the patient agonal period. To ensure that, simulated leakage tests were performed to quantify the effect of the stent graft design parameters on the amount of leaked flow from the perfusion region to the cardiac cycle. Different sealing lengths 50, 75, 100, and 125 mm, were used to measure the leakage. Several perfusion rates were examined, and the leakage was recorded for flow rates, 350, 500, 650, and 800 ml/min. The results were plotted as leakage flow rate for different perfusion lengths, using several perfusion flows rates. For ethical issues, the external oxygenated blood should not be mixed with the cardiac blood, not to interrupt the cardiac death [106]. To ensure that, the leakage from the perfusion region to the cardiac flow was investigated. The effect of the sealing lengths 50, 75, 100, and 125 mm was studied on the leakage rate for different perfusion rates. Figure 39A showed that the sealing length impacted significantly the leakage rate, where the minimum leakage rate was achieved for 125 mm sealing length. Also, the results displayed that

the leakage rate increased with higher perfusion flow rates. The leakage rate revealed an exponential relationship with the sealing length as shown in Figure 39B.

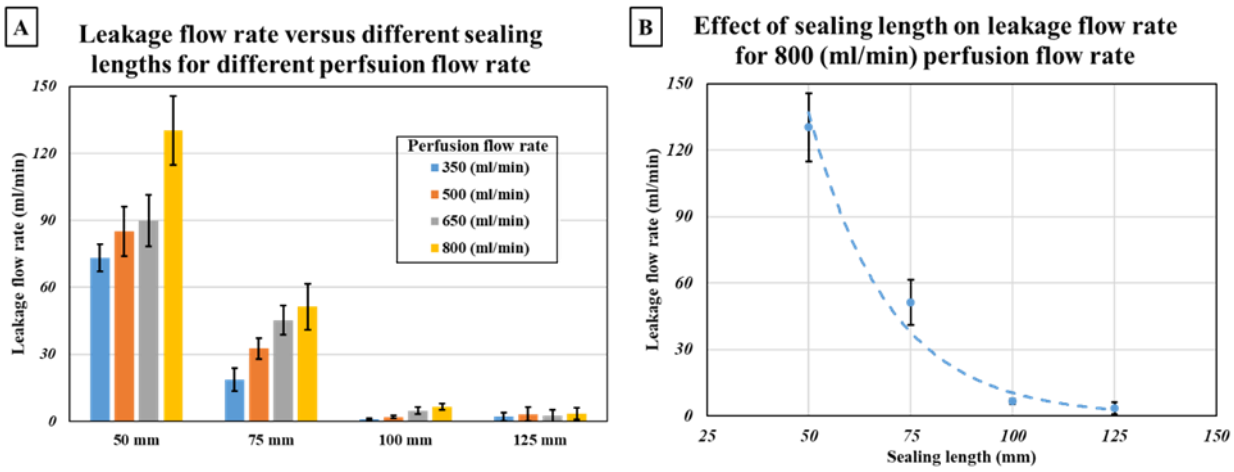

Figure 39 Leakage flow rate from the perfusion region to cardiac region. A) Leakage flow rate versus different sealing length for different perfusion flow rates. B) Effect of the sealing length on leakage flow rate for 800 (ml/min) perfusion flow rate.

5.3 Device Development

Using the results from the optimization process for the laser welding parameters, different prototypes were manufactured to be used in vivo inside the swine model. The device consists of three regions, 1) upper seal proximal to the heart, 2) middle region, and 3) lower seal proximal to the groin. The device has an upper and lower seal in order to divide the artery lumen into a dual chamber, one for normal cardiac flow, and the other for perfusion flow. Due to the complexity of the device, a precise micro-laser welding technique can be one of the best fabrication methods for creating the metallic backbone.

5.3.1 First Prototype

The device's main objective is to generate two isolated zones inside the aorta artery. To achieve this purpose, 16 Nitinol wires were used to generate two adjacent lumens, then merge the two lumens in the upper and lower seal, as seen in Figure 40A. The device has a unique design by changing the number of lumens through its length. Figure 40B shows metallic rods to show the number of lumens on each section of the device, where one lumen exists in the upper and lower seal, but two lumens in the middle perfusion section. Separated backbone is shown in the middle section, shown in Figure 40C, to allow the cardiac flow in one lumen, and the other lumen for the oxygenated blood perfusion. The first prototype was successful in generating two separate lumens, however, it was quite bulky, and it wasn't easily collapsed in smaller sheaths. Also, there was no smooth transition from different sections of the stent backbone.

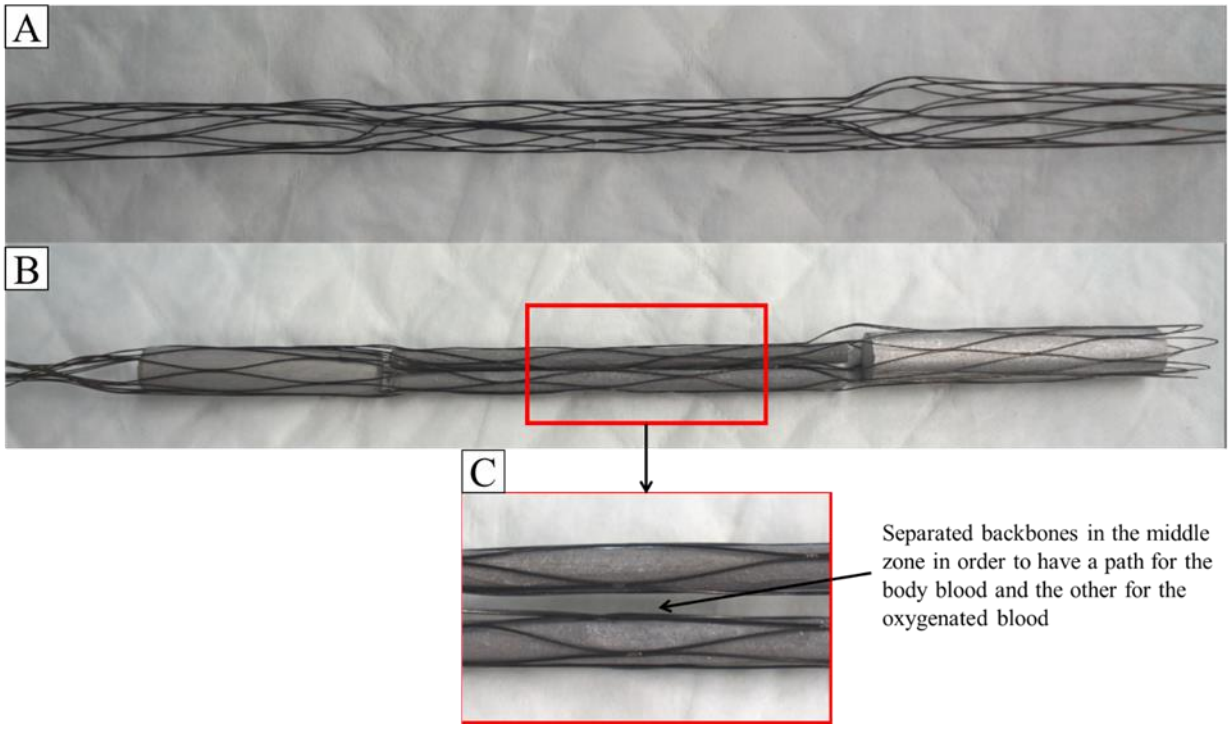

Figure 40 First prototype of dual chamber. (A) Using laser-welding, Nitinol wires were used to fabricate stent, with dual chambers in the middle. (B) Metallic rods used to show the lumens inside the stent. One lumen exists at both upper and lower sections of the stent, but two lumens in the middle section. (C) Magnified image to the middle regions, showing separated lumens.

5.3.2 Second Prototype

A new prototype was fabricated by welding a tapered tube shape for perfusion sheath docking, to a stent with smaller diameter in the middle, as shown in Figure 41A. Radiopaque markers were added on the stent top, perfusion region start, perfusion outlet location, perfusion region end, stent bottom. The metallic backbone was covered with ePTFE as shown in Figure 41B. The tapered welded tube showed high resistance during deploying and retrieval of the device, which was solved using a modified prototype.

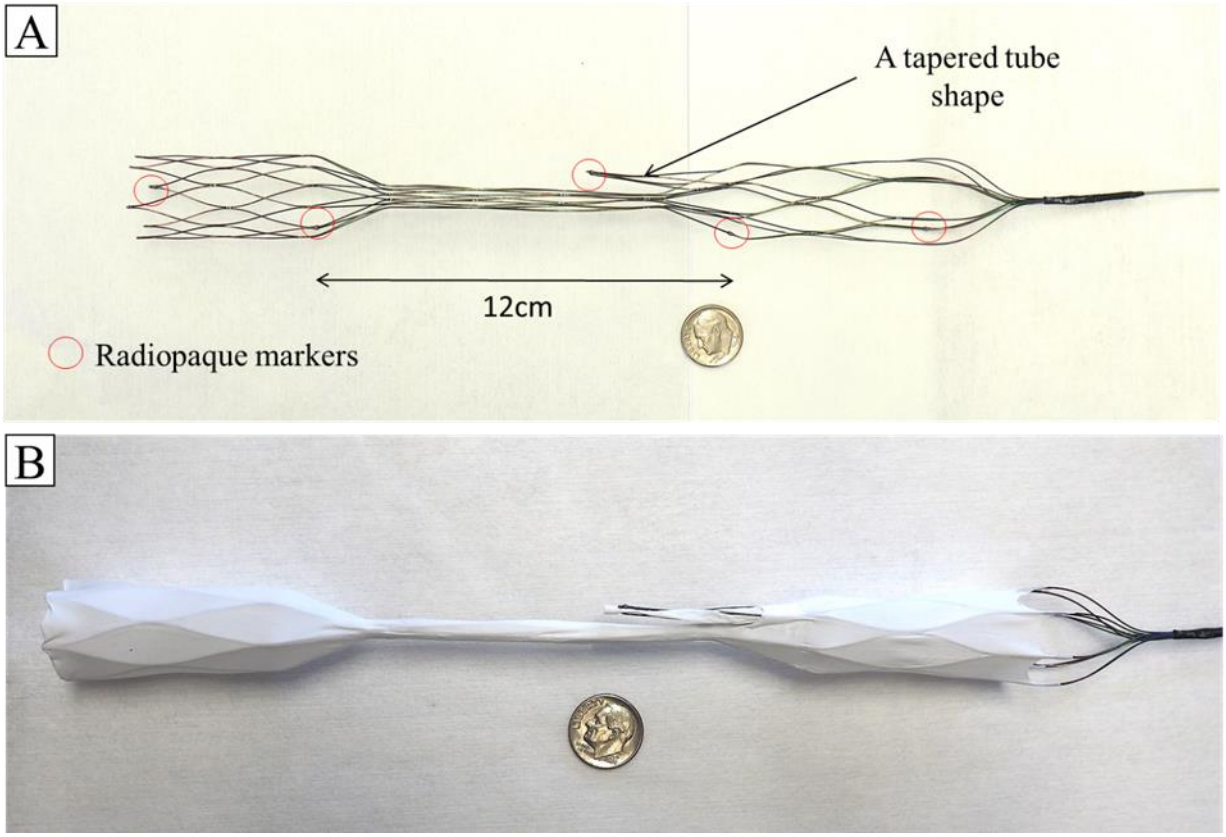

Figure 41 Second prototype of organ perfusion stent. (A) The metallic backbone is depicted with a welded tapered tube, for perfusion sheath docking. (B) The stent graft is covered with ePTFE, ready for in-vivo experiment.

5.3.3 Final Prototype

For the final prototype, the tapered tube was removed, and the docking system for perfusion sheath became a small ePTFE tube, glued to the backbone externally. Figure 42A shows the deployed device and completely collapsed with a 10 Fr delivery sheath in Figure 42B. The nosecone that has floppy tip, is used to help the sheath navigate inside the swine's vasculature. The middle region has a narrow conduit with the perfusion outlet as shown in Figure 42C, where the perfused oxygenated blood is supplied to the abdominal organs. The lower seal is connected

to extension wire that enables the surgeon to manipulate the device for delivery and retrieval processes.

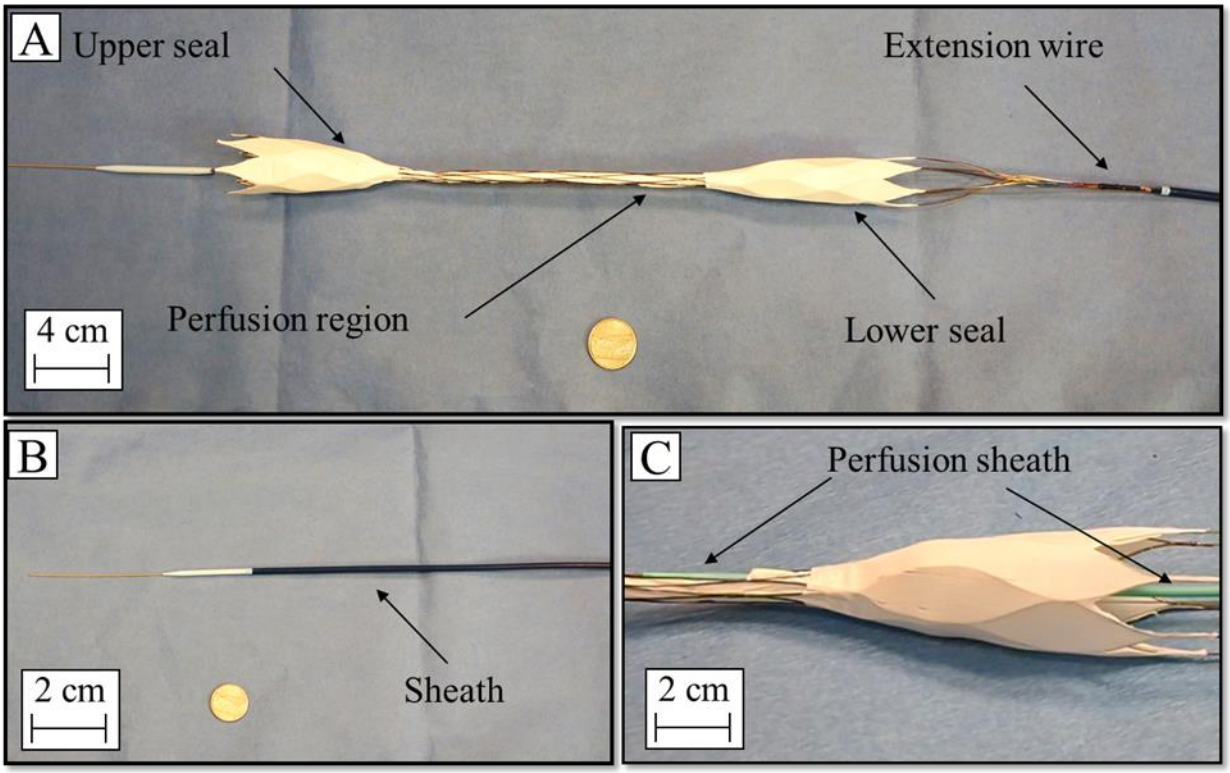

Figure 42 (A) Schematic drawing showing the functionality of OPS inside the aorta artery, (A) fully deployed device showing three sections with a nosecone and extension wire, (B) collapsed device into a 10Fr delivery sheath, and (C) magnified perfusion region.

5.4 In Vivo Test

Yorkshire pigs (around 80 kg), obtained from Archer Farms, Inc. (Darlington, MD), were used as in vivo models for the dual chambered organ perfusion stent (OPS). The animals were put under endotracheal anesthesia, upon approved IACUC protocol as part of University of Pittsburgh via isoflurane inhalation. The device was delivered from a femoral artery access, deployed and

assessed for separation of the abdominal organs from the systemic circulation using a conventional contrasted angiogram. Oxygenated blood flow was pumped using ECMO and delivered to the abdominal organs through an 8 Fr. perfusion catheter.

Performance of the organ perfusion stent (OPS) was evaluated using a swine model as shown in Figure 43. Figure 43A shows the baseline angiography of a branched segment of aorta without the device placement. Once the OPS is placed in this region (Figure 43B), the center lumen of the device excludes the branches only allowing cardiac flow to downward. Figure 43C illustrates the complete isolation of the blood flow from ECMO delivered via an 8Fr perfusion catheter with the outer chamber in the device. The arrowhead in Figure 43C indicates a perfusion lumen extending outside the body connected to ECMO.

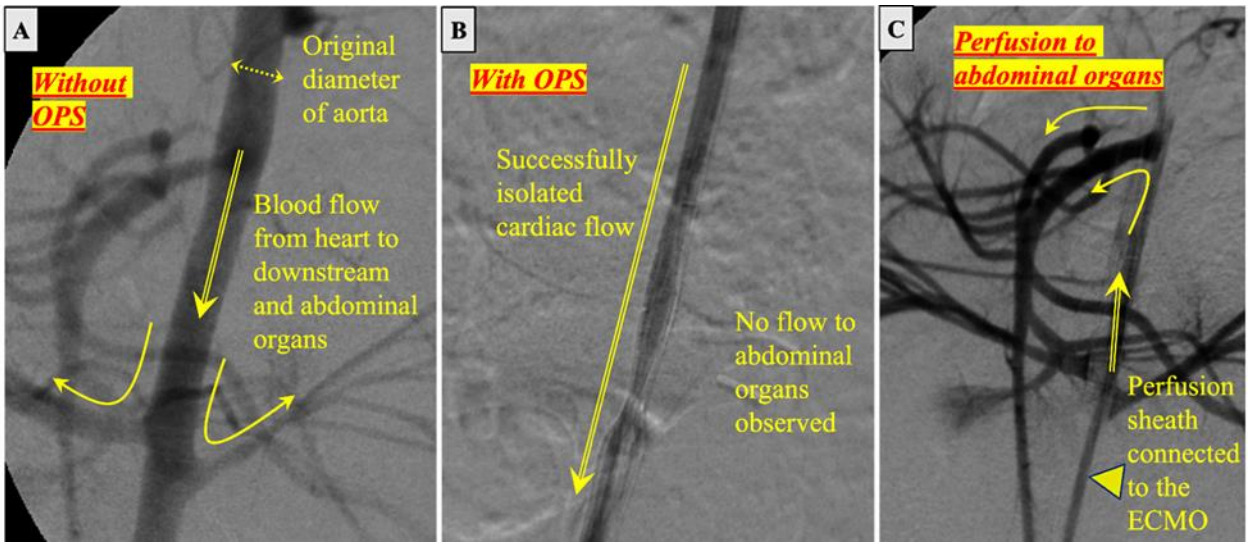

Figure 43 (A) Baseline angiography of a branched segment of aorta. Following placement of the dual chamber stent, the center lumen excludes the branches (B), whereas the outer chamber (C) isolates perfusion of the branches from a perfusion lumen extending outside the body (Arrowhead).

5.5 Discussion

Ischemic injury raised during the agonal phase, is considered the main obstacle for organ donations, despite the growing potential of donation after cardiac death (DCD) donors. This problem should be addressed to minimize the shortage of donor organs for transplant, because of the insufficient availability of donation of brain death (DBD) and living donation (LD). Since the ischemic organ damage is irreversible, and the organs are discarded, ensuring the oxygenated blood delivery to the abdominal organs during the agonal phase keeps them vital for donation.

The main ethical constraint of operating on a donor patient, before the official death, is the fear of shifting the donor death. A retrievable stent graft is proposed to reduce ischemic organ injury, with minimum patient intervention for ethical consideration. The main concept of the device is to divide the aortic artery into two chambers, one for cardiac cycle, and the other for oxygenated blood perfusion. In addition, sufficient oxygenated blood should be delivered to the perfusion region, to keep the organs sufficiently healthy for donation even though cardiac function is not appropriate.

To achieve the device functionality requirements, both radial force and flow rate measurements were studied to characterize and to optimize the best geometry and dimension of the OPS. At first, a computational analysis was carried out to investigate the effect of the seal length on the radial force, which is essential for attaining cardiac isolation, as well as preventing leakage between the perfusion and cardiac flow. Through applying radial force on the middle of the stent structure, the deformation pattern changed depending on the stent length. For shorter stent length, the whole length crimped, however with increasing the stent length, the deformation becomes more local. The deformation configuration affects the radial force to be minimum at 50 mm length and increased to reach maximum at 125 mm length. The minimum Von-Mises stress

was at 50 mm length, as the whole stent deformed, however, for longer stents, the deformation was locally, which induced higher stress values.

The effect of the device length on the radial force was also investigated experimentally. The effect of geometric parameters, such as a distance between joining regions and wire diameter, was investigated at previous work [68], and the optimized conditions were used in manufacturing the prototypes. The radial forces both in upper and lower seal were measured using the mechanical test system specifically designed for medical devices. Generally, the lower seal showed higher radial force in comparison to the upper seal for the same length, which can be explained due to upper and lower seal ends. For the upper seal case, one end is free and the other is connected to the perfusion structure, while in the lower seal case, one end is connected to the perfusion structure, and the other end has an extension wire. The free end in the upper seal decreases the total radial force, compared to the lower seal. The computational radial force from finite element analysis is in a good agreement with the radial force in the upper seal, since the CAD used for FEA modeled the stent free in both ends, which is the closest case to the upper seal.

An in vitro model was built to measure the cardiac and perfusion flow rates inside the aortic model. Figure 7A showed that the cardiac average flow was 2.5 liter/min at 120 mmHg. Once the stent graft is deployed inside the aorta, the cardiac flow rate dropped significantly, since the narrower diameter of the perfusion region increased the resistance against the flow. Vessel resistance [107] can be explained as follows,

$$\frac{R = 8\eta L}{\pi r^4}$$

Where, R is the resistance, η is the fluid viscosity, L is the vessel length, and r is the vessel diameter. As shown from the equation, the resistance of the vessel is inversely proportional to vessel diameter, which explains the flow drop. Also, from the resistance equation, the flow

resistance increased with longer vessels, which explained the results in Figure 7B, where the shorter perfusion length tended to have higher flow rates.

The main objective of the OPS is to keep the abdominal organs healthy for donation, which is significantly dependent on the oxygenated flow to the organs. The effect of some parameters of perfusion was examined for design optimization of the device. The perfusion sheath size impact was shown in figure 8A, and the measurements concluded that the larger sheath size can deliver more perfusion fluid. This can be explained by the resistance vessel formula, where the resistance decreases with vessel diameter increase. There was no perfusion difference between 9Fr. and 10Fr. sheaths, which can be understood as the resistance of the perfusion region, prevented any further increase in perfusion, and the 9Fr. sheath perfusion becomes the maximum perfusion flow can be achieved in this aortic model. The length of sheath length was tested, and the shorter the perfusion was, the higher perfusion delivered to the arteries. However, the perfusion length is constrained by the distance between the perfusion machine output and the abdominal arteries input through the body.

Also, the perfusion region length effect was investigated, and the smaller perfusion yielded more perfusion delivered to the abdominal organs. The main challenge with shortening the perfusion region, is the risk of occluding important branches by the seal zones, which will prevent the blood from reaching the organ, and causing organ ischemic injury. The minimum perfusion distance should be the length between the proximal and the distal (to the heart) openings of the main abdominal arteries. An extra length should be added to ensure proper flow to all the branch arteries, as well as, to overcome any issues from improper allocating the device inside the aorta. Finally, the effect of perfusion output location was examined with respect to the perfusion flow rate to the organs, and it was found that the distal perfusion output delivered the highest amount

of fluid to the abdominal arteries. When the perfusion output is in distal location, all the arteries' openings are in the way of fluid flow, however, in middle location, the renal arteries openings are in the opposite direction of the fluid flow, which means that the fluid needed to change direction to reach the kidney, which caused less perfusion delivery. Similarly, at the proximal location, all the arteries' openings are in the opposite directions, which was the reason that the minimum perfusion flow rate was in the proximal case.

One of the main functions of organ perfusion stent (OPS) is to isolate the abdominal organs from the cardiac flow, and to prevent the perfusion blood from reaching the cardiac flow, not to affect the agonal phase of the dying donor. The effect of sealing length was examined, and the results demonstrated that the minimum sealing length is 100 mm. The smaller seal length caused higher leakage, since the radial force is lower, as well as the contact surface area between the seal and the artery inner wall is smaller. To summarize the outcomes of this research, Table 5.1 mentions the main results for the optimized parameters, and the approach used to achieve the results.

Table 2 Summary of outcomes of the research conducted.

Parameters	Approach	Optimized results
Radial Force	Experimental and FEA for different seal length	Upper seal length = 125 mm Lower seal length = 100 mm
Perfusion length and output	Flow rate quantification using different perfusion length and outputs	Perfusion length = 100 mm Perfusion output, distal to heart.
Perfusion sheath size and length	Flow rate quantification using different sheaths sizes and lengths	Sheath size, 9Fr. Sheath length 500 mm
Leakage control	Leakage measurement	Seal length = 100 mm

In vivo swine models were used to validate the perfusion concept and as proof of concept for the organ perfusion stent (OPS) functionality. The device dimensions were tailored from the swine model anatomy. There were no significant device failure or fracture during the deployment and retrieval process with a 10Fr delivery sheath in vivo. In vivo test results with a swine model have demonstrated that a newly developed OPS via the optimized laser welding process can successfully isolate aortic flow into two different chambers.

5.6 Conclusion

A new organ perfusion stent has been successfully manufactured and tested in vivo demonstrating its feasibility. The device can maintain the necessary perfusion for organs from DCD (donation after cardiac death), until the time of cardiac death and formal organ recovery. The effect of seal length on the radial force was examined and 125 mm seal length exerted the highest radial force. A comprehensive study was exploited for the effect of perfusion region dimensions on both the cardiac and perfusion flow. The cardiac flow dropped by at least 30% after the device deployment. The perfusion sheath impacted the perfusion flow rate, to be maximum at 9Fr. sheath, in addition the shortest perfusion sheath is recommended to deliver the maximum amount of blood. The perfusion flow rate was maximum at 50 mm perfusion length, when the perfusion output was distal to the heart. The new stent graft fabricated, could be successfully delivered through a typical transcatheter procedure, and successfully isolated the cardiac flow from the branches to major abdominal organs. This new stent graft could substantially increase the number of available organs from the cardiac death donors minimizing potential organ ischemic complications.

6.0 Scientific Contributions

During the development of the two stent grafts, many challenges and barriers were met by this group, which were solved through, design analysis, parameter optimization, in vitro and in vivo experimentation of the device components. Through the finished research investigation, many contributions have been achieved in the area of endovascular devices. The engineering and clinical challenges that were solved during the research, helped in achieving new milestones in stent graft manufacturing. The challenges and associated contributions can be summarized as follows,

1. *Extremely long stent graft.*

In order to cover the internal wall of the long aorta artery, a novel extremely long stent graft was needed. Through the optimization process of Nitinol welding and annealing, this group was able to fabricate the longest available endovascular device. The stent graft produced, was up to 500 mm length, and maximum diameter 35 mm at the top section. In addition, the device was deployed and almost retrieved in a low profile 10 Fr. sheath inside a swine model.

Another engineering challenge was heat treatment of the long stent graft. The stent backbone was 500 mm; however, the tube furnace was limited to 300 mm heating length. A sequence of steps was developed for annealing the stent backbone in parts without affecting the superelasticity properties of Nitinol.

2. *Stent deployment and retrieval*

One of the main aspects of the stent grafts is to be deployed and retrieved rapidly and inside a small catheter. However, the deployed resistance was very high, beyond the force capability of human power.

The results showed how to design the configuration of the polymeric cover with respect to the metallic backbone, in order to maintain the deployment pushing force of the device, within the limits of surgeon force. Also, the results presented some insights on how to design temporary endovascular devices, which can be retrieved after achieving their purpose.

The resistance of deployment was found to be related to the radial force of the stent backbone. The in-vitro measurements showed the capability of manipulating the radial force of self-expanding Nitinol stents through geometric parameters of the stent structure, i.e. stent thickness, and distance between joints. Radial force control capability is crucial as unsuitable radial force can comprise the performance of endovascular devices. The less force causes leakage between stent graft and the inner wall of arteries, on the other hand, the more force induces injuries in the arteries tissues, which results in inflammatory response to the device.

Also, manufacturing challenges occurred during the manual fabrication of the stent backbone. The efficiency and quality of the backbone fabrication affected the stent graft resistance during deployment and retrieval. This challenge was addressed through ensuring that the distance between welds is the same in the whole device, to avoid buckled wires during stent graft retrieval. Also, the ePTFE covering was ensured to be homogenous through the stent graft.

3. Rapid hemorrhage control

The desired feature was a rapid delivery of a new long stent graft, to be used for massive traumatic hemorrhage of the great vessels with limited experience and limited imaging.

Design simplicity becomes an issue in designing the stent graft for delivery. Through developing processes and feedback from the clinical collaborators, the nosecone was integrated through welding a thin wire to the backbone bottom section. The new design of nosecone integration to the device and connecting an extension wire to the stent graft simplified the

endovascular process. The steps for stent graft positioning inside the body have been downsized into just one simple step, compared to the current sequences of steps, performed by the surgeon to insert a stent graft inside aorta artery.

Through this work, a new stent graft was fabricated to be used for life-threatening conditions of traumatic hemorrhage. The device is designed to be deployed via low experienced health workers, and imperfect imaging capability. In addition, the device should be delivered as fast as possible, and rapidly removed to allow permanent repair, once the patient reaches the hands of an experienced surgeon.

4. Expanding donation pool

Patients with malfunction abdominal organs are facing a significant problem due to the shortage of healthy organs for transplantation. The novel device (OPS) showed the potential to increase the available organs for transplanting. This would impact the people on the waiting list for organs transplanting and give them life and hope to have a normal life. Also, the healthcare costs will be saved from one donor (4 organs) by getting two patients off dialysis (kidneys), one patient off insulin (pancreas), and one patient out of the hospital for liver failure. The medical system is estimated to save up to 1.2 million dollars, just from one donor.

5. Devices for new applications

The novel features of trauma stent and organ perfusion stent like, ultra-long, and flow isolation, have broader impact on current and future endovascular devices. New devices can be developed using these features such as:

I. Local treatment of artery section: Using the capability of flow isolation, with access to the isolated part, new devices can be used to deliver special treatment without reaching the rest of the body.

II. Hemorrhage control during surgery: The device can be used during the surgery, if temporary bleeding control is needed, while curing another part of the body.

III. Long stent instead of multiple stents: Investigating the ability of manufacturing long stents, could change the procedure of deploying multiple stents, when needed, into a simpler one long stent.

7.0 Conclusions

Two novel stent grafts that have extremely long dimension and complex geometry have been successfully developed through the optimized manufacturing processes. In vitro mechanical test outcomes have demonstrated the mechanical performance of the trauma stent graft and some part of the organ perfusion stent. In vivo swine study results have demonstrated the devices' feasibility showing a successful hemorrhaging prevention in a trauma stent graft and a complete isolation of blood flow for organ transplant, respectively. As a result of this research study, few scientific contributions, as a first author, were published,

- Elsisy, M., Tillman, B. W., Go, C., Kuhn, J., Cho, S. K., Clark, W. W., Park, J., and Chun, Y., 2020, "Comprehensive Assessment of Mechanical Behavior of an Extremely Long Stent Graft to Control Hemorrhage in Torso," J. Biomed. Mater. Res. Part B Appl. Biomater., 108(5), pp. 2192–2203.
- Elsisy, M., and Chun, Y., 2020, "Materials Properties and Manufacturing Processes of Nitinol Endovascular Devices," Bio-Materials and Prototyping Applications in Medicine, P.J. Bártolo, and B. Bidanda, eds., Springer International Publishing, Cham, pp. 59–79.
- Elsisy, M., Herbert, R., Yeo, W.H., Pacella, J.J., and Chun, Y. "Development of a nanosensor-integrated stent for wireless, continuous monitoring of restenosis progression", Proc. SPIE 11590, Nano-, Bio-, Info-Tech Sensors and Wearable Systems, 1159006 (22 March 2021);
- Elsisy M., Shayan M., Chen Y., Tillman B.W., Go, C., Chun Y., "Assessment of mechanical and biocompatible performance of ultra-large Nitinol endovascular devices

fabricated via a low-energy laser joining process". Journal of Biomaterials Applications. 2021; 36(2):332-345.

- Elsisy, M., Tillman, B. W., Chou, L., Go, C., Cho, S. K., and Chun, Y., "Design Validation of a Novel Organ Perfusion Stent (OPS) for Successful Flow Separation in Donation after Cardiac Death," J. Biomed. Mater. Res. Part B Appl. Biomater., SUBMITTED.

This work was collaboration with other engineering and clinical groups, as a results, more journal paper were published as co-author,

- Shayan M, Gildener-Leapman N, Elsisy M, Hastings JT, Kwon S, Yeo W-H, Kim J-H, Shridhar P, Salazar G, Chun Y. "Use of Superelastic Nitinol and Highly-Stretchable Latex to Develop a Tongue Prosthetic Assist Device and Facilitate Swallowing for Dysphagia Patients". Materials. 2019; 12(21):3555.
- Chun, Y., Chen, Y., Elsisy, M., Sukinik, J., Shridhar, P., Park, J., Kim, Y., Hong, C., Chung, J., 2019, "In vitro and in vivo experiments of a novel intra-arterial neurovascular decompressor for treating neurovascular compression syndromes: a brief report," Neurological Research, 41(7), pp. 665-670.
- Go, C., Elsisy, M., Chun, Y., Thirumala, P., Clark, W., Cho, S., Demetris, A., Tillman, B., 2020, "A three-tier Rescue stent improves outcomes over balloon occlusion in a porcine model of noncompressible hemorrhage," Journal of Trauma and Acute Care Surgery, 89(2), pp. 320-328.
- Go, C, Kuhn, J, Elsisy, M, et al. "Rescue stent improves outcomes compared with resuscitative endovascular balloon occlusion of the aorta in noncompressible hemorrhage." J Am Coll Surg 2019; 229: S308–S309.

This Group has applied to 2020 Michael G. Wells Student Healthcare Competition, and the group was awarded $5,000 to be used for further development and investigation of the commercial capability. After the progress in device development, an additional $15,000 was awarded, to continue device performance characterization.

More work is needed in order to have the two devices commercialized for human usage. Still, there is an issue with complete retrieval of both devices inside 10 Fr. sheath. During in vivo studies, around 90% of the devices were captured. Also, the devices are required to be captured inside 8 Fr. sheath or less, so more resistance minimizing is essential to achieve this goal. The work was focused on animal trials, future devices should target human cases, with different dimensions and performance requirements.

Bibliography

[1] Ölander, A., 1932, "AN ELECTROCHEMICAL INVESTIGATION OF SOLID CADMIUM-GOLD ALLOYS," J. Am. Chem. Soc., **54**(10), pp. 3819–3833.

[2] Wayman, C. M., and Harrison, J. D., 1989, "The Origins of the Shape Memory Effect," JOM, **41**(9), pp. 26–28.

[3] Buehler, W. J., Gilfrich, J. V, and Wiley, R. C., 1963, "Effect of Low-Temperature Phase Changes on the Mechanical Properties of Alloys near Composition TiNi," J. Appl. Phys., **34**(5), pp. 1475–1477.

[4] Wang, F. E., Buehler, W. J., and Pickart, S. J., 1965, "Crystal Structure and a Unique ``Martensitic'' Transition of TiNi," J. Appl. Phys., **36**(10), pp. 3232–3239.

[5] Rabkin, D. J., Lang, E. V, and Brophy, D. P., 2000, "Nitinol Properties Affecting Uses in Interventional Radiology," J. Vasc. Interv. Radiol., **11**(3), pp. 343–350.

[6] Yamamoto, S., Wilczek, H. E., Iwata, T., Larsson, M., Gjertsen, H., Söderdahl, G., Solders, G., and Ericzon, B.-G., 2007, "Long-Term Consequences of Domino Liver Transplantation Using Familial Amyloidotic Polyneuropathy Grafts.," Transpl. Int. Off. J. Eur. Soc. Organ Transplant., **20**(11), pp. 926–933.

[7] Barras, C. D. J., and Myers, K. A., 2000, "Nitinol – Its Use in Vascular Surgery and Other Applications," Eur. J. Vasc. Endovasc. Surg., **19**(6), pp. 564–569.

[8] Stoeckel, D., Pelton, A., and Duerig, T., 2004, "Self-Expanding Nitinol Stents: Material and Design Considerations," Eur. Radiol., **14**(2), pp. 292–301.

[9] Pelton, A., Stöckel, D., and Duerig, T., 2000, "Medical Uses of Nitinol," Mater. Sci. Forum - MATER SCI FORUM, **327**, pp. 63–70.

[10] Hallab, N. J., Bundy, K. J., O'Connor, K., Moses, R. L., and Jacobs, J. J., 2001, "Evaluation of Metallic and Polymeric Biomaterial Surface Energy and Surface Roughness Characteristics for Directed Cell Adhesion.," Tissue Eng., **7**(1), pp. 55–71.

[11] Ponsonnet, L., Comte, V., Othmane, A., Lagneau, C., Charbonnier, M., Lissac, M., and Jaffrezic, N., 2002, "Effect of Surface Topography and Chemistry on Adhesion, Orientation and Growth of Fibroblasts on Nickel–Titanium Substrates," Mater. Sci. Eng. C, **21**(1), pp. 157–165.

[12] Shabalovskaya, S. A., 2002, "Surface, Corrosion and Biocompatibility Aspects of Nitinol as an Implant Material," Biomed. Mater. Eng., **12**(1), pp. 69–109.

[13] Ponsonnet, L., Comte, V., Othmane, A., Lagneau, C., Charbonnier, M., Lissac, M., and Jaffrezic, N., 2002, "Effect of Surface Topography and Chemistry on Adhesion, Orientation and Growth of Fibroblasts on Nickel-Titanium Substrates," Mater. Sci. Eng. C, **21**(1–2), pp. 157–165.

[14] Sapatnekar, S., Kieswetter, K. M., Merritt, K., Anderson, J. M., Cahalan, L., Verhoeven, M., Hendriks, M., Fouache, B., and Cahalan, P., 1995, "Blood-Biomaterial Interactions in a Flow System in the Presence of Bacteria: Effect of Protein Adsorption." J. Biomed. Mater. Res., **29**(2), pp. 247–256.

[15] Shabalovskaya, S. A., 2002, "Surface, Corrosion and Biocompatibility Aspects of Nitinol as an Implant Material," Biomed. Mater. Eng., **12**(1), pp. 69–109.

[16] Sapatnekar, S., Kieswetter, K. M., Merritt, K., Anderson, J. M., Cahalan, L., Verhoeven, M., Hendriks, M., Fouache, B., and Cahalan, P., 1995, "Blood–Biomaterial Interactions in a Flow System in the Presence of Bacteria: Effect of Protein Adsorption," J. Biomed. Mater. Res., **29**(2), pp. 247–256.

[17] Duerig, T. W., Melton, K. N., Stöckel, D., and Wayman, C. M., eds., 1990, "Introduction," *Engineering Aspects of Shape Memory Alloys*, Butterworth-Heinemann, pp. v–vi.

[18] Schetky, L. M., and Wu, M. H., 2003, "Issues in the Further Development of Nitinol Properties and Processing for Medical Device Applications," pp. 271–276.

[19] Shabalovskaya, S., Anderegg, J., and Humbeeck, J. Van, 2008, "Critical Overview of Nitinol Surfaces and Their Modifications for Medical Applications," Acta Biomater., **4**, pp. 447–467.

[20] Palmaz, J. C., 1988, "Balloon-Expandable Intravascular Stent," Am. J. Roentgenol., **150**(6), pp. 1263–1269.

[21] Pfeifer, R., Herzog, D., Hustedt, M., and Barcikowski, S., 2010, "Pulsed Nd: YAG Laser Cutting of NiTi Shape Memory Alloys—Influence of Process Parameters," J. Mater. Process. Technol., **210**(14), pp. 1918–1925.

[22] Biffi, C. A., and Tuissi, A., 2017, "Nitinol Laser Cutting: Microstructure and Functional Properties of Femtosecond and Continuous Wave Laser Processing," Smart Mater. Struct., **26**(3), p. 35006.

[23] Liu, L., Li, D. B., Tong, Y. F., and Zhu, Y. F., 2016, "Fiber Laser Micromachining of Thin NiTi Tubes for Shape Memory Vascular Stents," Appl. Phys. A, **122**(7), p. 638.

[24] Muhammad, N., Whitehead, D., Boor, A., Oppenlander, W., Liu, Z., and Li, L., 2012, "Picosecond Laser Micromachining of Nitinol and Platinum–Iridium Alloy for Coronary Stent Applications," Appl. Phys. A, **106**(3), pp. 607–617.

[25] Chen, L., 2008, "Laser Cutting for Medical Device (STENT) - Yesterday, Today and Tomorrow," pp. 320–324.

[26] Quintino, L., and Miranda, R. M., 2012, "Welding Shape Memory Alloys with NdYAG Lasers," Soldag. InspeÃ§Ã\poundso, **17**, pp. 210–217.

[27] Mirshekari, G. R., Saatchi, A., Kermanpur, A., and Sadrnezhaad, S. K., 2013, "Laser Welding of NiTi Shape Memory Alloy: Comparison of the Similar and Dissimilar Joints to AISI 304 Stainless Steel," Opt. Laser Technol., **54**, pp. 151–158.

[28] Hsu, Y. T., Wang, Y. R., Wu, S., and Chen, C., 2001, "Effect of CO2 Laser Welding on the Shape-Memory and Corrosion Characteristics of TiNi Alloys," Metall. Mater. Trans. A, **32**, pp. 569–576.

[29] Oliveira, J. P., Barbosa, D., Fernandes, F. M. B., and Miranda, R. M., 2016, "Tungsten Inert Gas ({TIG}) Welding of Ni-Rich {NiTi} Plates: Functional Behavior," Smart Mater. Struct., **25**(3), p. 03LT01.

[30] Wu, M., 2002, "Fabrication of Nitinol Materials and Components," Mater. Sci. Forum, **394**, pp. 285–292.

[31] Li, H. M., Sun, D.-Q., Cai, X. L., Dong, P., and Wang, W. Q., 2012, "Laser Welding of TiNi Shape Memory Alloy and Stainless Steel Using Ni Interlayer," Mater. Des., **39**, pp. 285–293.

[32] Drexel, M., Selvaduray, G., and Pelton, A., 2007, "The Effects of Cold Work and Heat Treatment on the Properties of Nitinol Wire," *Proceedings of the 2nd Frontiers in Biomedical Devices Conference 2007*.

[33] Lei, X., Rui, W., and Yong, L., 2011, "The Optimization of Annealing and Cold-Drawing in the Manufacture of the Ni–Ti Shape Memory Alloy Ultra-Thin Wire," Int. J. Adv. Manuf. Technol., **55**(9), pp. 905–910.

[34] Vojtech, D., 2010, "Influence of Heat Treatment of Shape Memory Niti Alloy on Its Mechanical Properties," Met. 2010 - 19th Int. Conf. Metall. Mater. Conf. Proc., pp. 867–871.

[35] Simka, W., Kaczmarek, M., Baron-Wiecheć, A., Nawrat, G., Marciniak, J., and Żak, J., 2010, "Electropolishing and Passivation of NiTi Shape Memory Alloy," Electrochim. Acta, **55**(7), pp. 2437–2441.

[36] Venugopalan, R., and Trépanier, C., 2000, "Assessing the Corrosion Behavior of Nitinol for Minimally-Invasive Device Design," Minim. Invasive Ther. Allied Technol. - MINIM INVASIVE THER ALLIED T, **9**, pp. 67–73.

[37] Thierry, B., Tabrizian, M., Savadogo, O., and Yahia, L., 2000, "Effects of Sterilization Processes on NiTi Alloy: Surface Characterization," J. Biomed. Mater. Res., **49**(1), pp. 88–98.

[38] Michiardi, A., Aparicio, C., Planell, J. A., and Gil, F. J., 2006, "New Oxidation Treatment of NiTi Shape Memory Alloys to Obtain Ni-Free Surfaces and to Improve Biocompatibility.," J. Biomed. Mater. Res. B. Appl. Biomater., **77**(2), pp. 249–256.

[39] Chun, Y., Levi, D. S., Mohanchandra, K. P., Vinuela, F., Vinuela Jr., F., and Carman, G. P., 2009, "Thin Film Nitinol Microstent for Aneurysm Occlusion," J. Biomech. Eng., **131**(5).

[40] Sun, Z., 2009, "Endovascular Stent Graft Repair of Abdominal Aortic Aneurysms: Current Status and Future Directions," World J. Radiol., **1**(1), pp. 63–71.

[41] Buck, D. B., van Herwaarden, J. A., Schermerhorn, M. L., and Moll, F. L., 2014, "Endovascular Treatment of Abdominal Aortic Aneurysms," Nat. Rev. Cardiol., **11**(2), pp. 112–123.

[42] Dotter, C. T., 1969, "Transluminally-Placed Coilspring Endarterial Tube Grafts. Long-Term Patency in Canine Popliteal Artery." Invest. Radiol. **4**(5), pp. 329–332.

[43] Palmaz, J. C., 1992, "Intravascular Stenting: From Basic Research to Clinical Application.," Cardiovasc. Intervent. Radiol. **15**(5), pp. 279–284.

[44] Schatz, R. A., Palmaz, J. C., Tio, F. O., Garcia, F., Garcia, O., and Reuter, S. R., 1987, "Balloon-Expandable Intracoronary Stents in the Adult Dog.," Circulation, **76**(2), pp. 450–457.

[45] Buchwald, A., Unterberg, C., Werner, G., Voth, E., Kreuzer, H., and Wiegand, V., 1991, "Initial Clinical Results with the Wiktor Stent: A New Balloon-Expandable Coronary Stent." Clin. Cardiol., **14**(5), pp. 374–379.

[46] Kurre, W., Brassel, F., Brüning, R., Buhk, J., Eckert, B., Horner, S., Knauth, M., Liebig, T., Maskova, J., Mucha, D., Sychra, V., Sitzer, M., Sonnberger, M., Tietke, M., Trenkler, J., Turowski, B., and Berkefeld, J., 2012, "Complication Rates Using Balloon-Expandable and Self-Expanding Stents for the Treatment of Intracranial Atherosclerotic Stenoses : Analysis of the INTRASTENT Multicentric Registry.," Neuroradiology, **54**(1), pp. 43–50.

[47] Beyar, R., Shofti, R., Grenedier, E., Henry, M., Globerman, O., and Beyar, M., 1994, "Self-Expandable Nitinol Stent for Cardiovascular Applications: Canine and Human Experience," Cathet. Cardiovasc. Diagn., **32**(2), pp. 162–170.

[48] Greenberg, R. K., West, K., Pfaff, K., Foster, J., Skender, D., Haulon, S., Sereika, J., Geiger, L., Lyden, S. P., Clair, D., Svensson, L., and Lytle, B., 2006, "Beyond the Aortic Bifurcation: Branched Endovascular Grafts for Thoracoabdominal and Aortoiliac Aneurysms.," J. Vasc. Surg., **43**(5), pp. 877–879.

[49] Grabenwöger, M., Hutschala, D., Ehrlich, M. P., Cartes-Zumelzu, F., Thurnher, S., Lammer, J., Wolner, E., and Havel, M., 2000, "Thoracic Aortic Aneurysms: Treatment with Endovascular Self-Expandable Stent Grafts.," Ann. Thorac. Surg., **69**(2), pp. 441–445.

[50] Duerig, T., Pelton, A., and Stöckel, D., 1999, "An Overview of Nitinol Medical Applications," Mater. Sci. Eng. A, **273**–**275**, pp. 149–160.

[51] Zajarias, A., and Cribier, A. G., 2009, "Outcomes and Safety of Percutaneous Aortic Valve Replacement." J. Am. Coll. Cardiol., **53**(20), pp. 1829–1836.

[52] Baan, J., Yong, Z. Y., Koch, K. T., Henriques, J. P. S., Bouma, B. J., de Hert, S. G., van der Meulen, J., Tijssen, J. G. P., Piek, J. J., and de Mol, B. A. J. M., 2010, "Percutaneous Implantation of the CoreValve Aortic Valve Prosthesis in Patients at High Risk or Rejected for Surgical Valve Replacement: Clinical Evaluation and Feasibility of the Procedure in the First 30 Patients in the AMC-UvA.," Netherlands Hear. J. Mon. J. Netherlands Soc. Cardiol. Netherlands Hear. Found., **18**(1), pp. 18–24.

[53] Grube, E., Laborde, J. C., Zickmann, B., Gerckens, U., Felderhoff, T., Sauren, B., Bootsveld, A., Buellesfeld, L., and Iversen, S., 2005, "First Report on a Human Percutaneous Transluminal Implantation of a Self-Expanding Valve Prosthesis for Interventional Treatment of Aortic Valve Stenosis." Catheter. Cardiovasc. Interv. Off. J. Soc. Card. Angiogr. Interv., **66**(4), pp. 465–469.

[54] Boudjemline, Y., and Bonhoeffer, P., 2002, "Steps Toward Percutaneous Aortic Valve Replacement," Circulation, **105**(6), pp. 775–778.

[55] Leon, M. B., Kodali, S., Williams, M., Oz, M., Smith, C., Stewart, A., Schwartz, A., Collins, M., and Moses, J. W., 2006, "Transcatheter Aortic Valve Replacement in Patients with Critical Aortic Stenosis: Rationale, Device Descriptions, Early Clinical Experiences, and Perspectives.," Semin. Thorac. Cardiovasc. Surg., **18**(2), pp. 165–174.

[56] Simon, M., Kaplow, R., Salzman, E., and Freiman, D., 1977, "A Vena Cava Filter Using Thermal Shape Memory Alloy. Experimental Aspects." Radiology, **125**(1), pp. 87–94.

[57] Bruckheimer, E., Judelman, A. G., Bruckheimer, S. D., Tavori, I., Naor, G., and Katzen, B. T., 2003, "In Vitro Evaluation of a Retrievable Low-Profile Nitinol Vena Cava Filter.," J. Vasc. Interv. Radiol., **14**(4), pp. 469–474.

[58] Simon, M., Kaplow, R., Salzman, E., and Freiman, D., 1977, "A Vena Cava Filter Using Thermal Shape Memory Alloy Experimental Aspects," Radiology, **125**(1), pp. 89–94.

[59] Engmann, E., and Asch, M. R., 1998, "Clinical Experience with the Antecubital Simon Nitinol IVC Filter," J. Vasc. Interv. Radiol., **9**(5), pp. 774–778.

[60] Murphy, J. G., Gersh, B. J., McGoon, M. D., Mair, D. D., Porter, C. J., Ilstrup, D. M., McGoon, D. C., Puga, F. J., Kirklin, J. W., and Danielson, G. K., 1990, "Long-Term Outcome after Surgical Repair of Isolated Atrial Septal Defect," N. Engl. J. Med., **323**(24), pp. 1645–1650.

[61] Thanopoulos, B. D., Laskari, C. V, Tsaousis, G. S., Zarayelyan, A., Vekiou, A., and Papadopoulos, G. S., 1998, "Closure of Atrial Septal Defects with the Amplatzer Occlusion Device: Preliminary Results.," J. Am. Coll. Cardiol., **31**(5), pp. 1110–1116.

[62] Sharafuddin, M. J. A., Gu, X., Titus, J. L., Urness, M., Cervera-Ceballos, J. J., and Amplatz, K., 1997, "Transvenous Closure of Secundum Atrial Septal Defects," Circulation, **95**(8), pp. 2162–2168.

[63] Sahn, D. J., 2001, "Moss and Adams 2019; Heart Disease in Infants, Children, and Adolescents, Including the Fetus and Young Adult, 6th Ed," Circulation, **104**(24), pp. e139–e140.

[64] Toro, A., Geertruyden, W., Misiolek, W., Han, X. D., and Wu, M. H., 2008, "Microstructural Characterization of Nitinol Stents," SMST-2006 - Proc. Int. Conf. Shape Mem. Superelastic Technol., pp. 693–702.

[65] Elsisy, M., and Chun, Y., 2021, "Materials Properties and Manufacturing Processes of Nitinol Endovascular Devices," *Bio-Materials and Prototyping Applications in Medicine*, P.J. Bártolo, and B. Bidanda, eds., Springer International Publishing, Cham, pp. 59–79.

[66] Khan, M. I., Panda, S. K., and Zhou, Y., 2008, "Effects of Welding Parameters on the Mechanical Performance of Laser Welded Nitinol," Mater. Trans., **49**(11), pp. 2702–2708.

[67] Go, C., Elsisy, M., Chun, Y., Thirumala, P. D., Clark, W. W., Cho, S. K., Demetris, A. J., and Tillman, B. W., 2020, "A Three-Tier Rescue Stent Improves Outcomes over Balloon Occlusion in a Porcine Model of Noncompressible Hemorrhage," J. Trauma Acute Care Surg., **89**(2), p. 320—328.

[68] Elsisy, M., Tillman, B. W., Go, C., Kuhn, J., Cho, S. K., Clark, W. W., Park, J., and Chun, Y., 2020, "Comprehensive Assessment of Mechanical Behavior of an Extremely Long Stent Graft to Control Hemorrhage in Torso," J. Biomed. Mater. Res. Part B Appl. Biomater., **108**(5), pp. 2192–2203.

[69] Andersen, H. R., Knudsen, L. L., and Hasenkam, J. M., 1992, "Transluminal Implantation of Artificial Heart Valves. Description of a New Expandable Aortic Valve and Initial Results with Implantation by Catheter Technique in Closed Chest Pigs.," Eur. Heart J., **13**(5), pp. 704–708.

[70] King, T. D., Thompson, S. L., Steiner, C., and Mills, N. L., 1976, "Secundum Atrial Septal Defect. Nonoperative Closure during Cardiac Catheterization." JAMA, **235**(23), pp. 2506–2509.

[71] Palmaz, J. C., 1992, "Intravascular Stenting: From Basic Research to Clinical Application," Cardiovasc. Intervent. Radiol. **15**(5), pp. 279–284.

[72] Parodi, J. C., Palmaz, J. C., and Barone, H. D., 1991, "Transfemoral Intraluminal Graft Implantation for Abdominal Aortic Aneurysms." Ann. Vasc. Surg., **5**(6), pp. 491–499.

[73] Tzifa, A., Ewert, P., Brzezinska-Rajszys, G., Peters, B., Zubrzycka, M., Rosenthal, E., Berger, F., and Qureshi, S. A., 2006, "Covered Cheatham-Platinum Stents for Aortic Coarctation: Early and Intermediate-Term Results.," J. Am. Coll. Cardiol., **47**(7), pp. 1457–1463.

[74] Thalhammer, C., Kirchherr, A. S., Uhlich, F., Waigand, J., and Gross, C. M., 2000, "Postcatheterization Pseudoaneurysms and Arteriovenous Fistulas: Repair with Percutaneous Implantation of Endovascular Covered Stents," Radiology, **214**(1), pp. 127–131.

[75] Maras, D., Lioupis, C., Magoufis, G., Tsamopoulos, N., Moulakakis, K., and Andrikopoulos, V., 2006, "Covered Stent-Graft Treatment of Traumatic Internal Carotid Artery Pseudoaneurysms: A Review." Cardiovasc. Intervent. Radiol., **29**(6), pp. 958–968.

[76] Chen, Y., Tillman, B., Go, C., Cho, S. K., Clark, W. W., Hur, T. B., Ding, Y., and Chun, Y., 2019, "A Novel Customizable Stent Graft That Contains a Stretchable EPTFE with a Laser-Welded Nitinol Stent.," J. Biomed. Mater. Res. B. Appl. Biomater., **107**(4), pp. 911–923.

[77] Serruys, P. W., de Jaegere, P., Kiemeneij, F., Macaya, C., Rutsch, W., Heyndrickx, G., Emanuelsson, H., Marco, J., Legrand, V., Materne, P., Belardi, J., Sigwart, U., Colombo, A., Goy, J. J., van den Heuvel, P., Delcan, J., and Morel, M., 1994, "A Comparison of Balloon-Expandable-Stent Implantation with Balloon Angioplasty in Patients with Coronary Artery Disease," N. Engl. J. Med., **331**(8), pp. 489–495.

[78] Suárez de Lezo, J., Pan, M., Romero, M., Medina, A., Segura, J., Pavlovic, D., Martinez, C., Tejero, I., Perez Navero, J., and Torres, F., 1995, "Balloon-Expandable Stent Repair of Severe Coarctation of Aorta.," Am. Heart J., **129**(5), pp. 1002–1008.

[79] Palma, J. H., Marcondes de Souza, J. A., Rodrigues Alves, C. M., Carvalho, A. C., and Buffolo, E., 2002, "Self-Expandable Aortic Stent-Grafts for Treatment of Descending Aortic Dissections," Ann. Thorac. Surg., **73**(4), pp. 1138–1141.

[80] LILIP, L. A. U., THOMAS, M. C., M, H. W., WOONZA, R., and A, M. K., 1995, "Self-Expandable Helical Intravascular Stent and Stent-Graft."

[81] Dake, M. D., Miller, D. C., Semba, C. P., Mitchell, R. S., Walker, P. J., and Liddell, R. P., 1994, "Transluminal Placement of Endovascular Stent-Grafts for the Treatment of Descending Thoracic Aortic Aneurysms," N. Engl. J. Med., **331**(26), pp. 1729–1734.

[82] Blum, U., Voshage, G., Lammer, J., Beyersdorf, F., Töllner, D., Kretschmer, G., Spillner, G., Polterauer, P., Nagel, G., Hölzenbein, T., Thurnher, S., and Langer, M., 1997, "Endoluminal Stent–Grafts for Infrarenal Abdominal Aortic Aneurysms," N. Engl. J. Med., **336**(1), pp. 13–20.

[83] Razavi, M. K., Dake, M. D., Semba, C. P., Nyman, U. R., and Liddell, R. P., 1995, "Percutaneous Endoluminal Placement of Stent-Grafts for the Treatment of Isolated Iliac Artery Aneurysms.," Radiology, **197**(3), pp. 801–804.

[84] Greenberg, R. K., West, K., Pfaff, K., Foster, J., Skender, D., Haulon, S., Sereika, J., Geiger, L., Lyden, S. P., Clair, D., Svensson, L., and Lytle, B., 2006, "Beyond the Aortic Bifurcation : Branched Endovascular Grafts for Thoracoabdominal and Aortoiliac Aneurysms," J. Vasc. Surg., **45**(5), pp. 879–86.

[85] Larson, R. A., Solomon, J., and Carpenter, J. P., 2002, "Stent Graft Repair of Visceral Artery Aneurysms.," J. Vasc. Surg., **36**(6), pp. 1260–1263.

[86]2020, "GORE® TAG® Thoracic Endoprosthesis" [Online]. Available: https://www.goremedical.com/products/ctag---specifications.

[87]"GORE® VIABAHN® Endoprosthesis," 2020 [Online]. Available: https://www.goremedical.com/products/viabahn---specifications-us.

[88] Grabenwöger, M., Hutschala, D., Ehrlich, M. P., Cartes-Zumelzu, F., Thurnher, S., Lammer, J., Wolner, E., and Havel, M., 2000, "Thoracic Aortic Aneurysms: Treatment with Endovascular Self-Expandable Stent Grafts," Ann. Thorac. Surg., **69**(2), pp. 441–445.

[89] Zhang, L., Yin, C., Li, H., Bao, J., Zhao, Z., Qu, L., Feng, X., Feng, R., Lu, Q., and Jing, Z., 2013, "Multiple Overlapping Bare Stents for Endovascular Visceral Aneurysm Repair: A Potential Alternative Endovascular Strategy to Multilayer Stents," Ann. Vasc. Surg., **27**(5), pp. 606–612.

[90] Mummert, J., Sirois, E., and Sun, W., 2013, "Quantification of Biomechanical Interaction of Transcatheter Aortic Valve Stent Deployed in Porcine and Ovine Hearts.," Ann. Biomed. Eng., **41**(3), pp. 577–586.

[91] Shabalovskaya, S., Anderegg, J., and Van Humbeeck, J., 2008, "Critical Overview of Nitinol Surfaces and Their Modifications for Medical Applications," Acta Biomater., **4**(3), pp. 447–467.

[92] Ragab, A.-R. A. F., and Bayoumi, S. E. A., 2018, *Engineering Solid Mechanics: Fundamentals and Applications*.

[93] Khalil-Allafi, J., Eggeler, G., Dlouhy, A., Schmahl, W. W., and Somsen, C., 2004, "On the Influence of Heterogeneous Precipitation on Martensitic Transformations in a Ni-Rich NiTi Shape Memory Alloy," Mater. Sci. Eng. A, **378**(1), pp. 148–151.

[94] Liu, X., Wang, Y., Yang, D., and Qi, M., 2008, "The Effect of Ageing Treatment on Shape-Setting and Superelasticity of a Nitinol Stent," Mater. Charact., **59**(4), pp. 402–406.

[95] Van Prehn, J., Schlösser, F. J. V., Muhs, B. E., Verhagen, H. J. M., Moll, F. L., and van Herwaarden, J. A., 2009, "Oversizing of Aortic Stent Grafts for Abdominal Aneurysm Repair: A Systematic Review of the Benefits and Risks," Eur. J. Vasc. Endovasc. Surg., **38**(1), pp. 42–53.

[96] "Organ Procurement and Transplantation Network (OPTN) and Scientific Registry of Transplant Recipients (SRTR). 2020 Annual Data Report, Rockville, MD: Department of Health and Human Services, Health Resources and Services Administrations."

[97] Scalea, J. R., Redfield, R. R., Rizzari, M. D., Bennett, R., Anderson, M. E., Anderson, J. E., Kaufman, D. B., Sollinger, H. W., Fernandez, L. A., D'Alessandro, A. M., and Mezrich,

J., 2016, “When Do DCD Donors Die?: Outcomes and Implications of DCD at a High-Volume, Single-Center OPO in the United States.,” Ann. Surg., **263**(2), pp. 211–216.

[98] Saidi, R. F., Bradley, J., Greer, D., Luskin, R., O’Connor, K., Delmonico, F., Kennealey, P., Pathan, F., Schuetz, C., Elias, N., Ko, D. S. C., Kawai, T., Hertl, M., Cosimi, A. B., and Markmann, J. F., 2010, “Changing Pattern of Organ Donation at a Single Center: Are Potential Brain Dead Donors Being Lost to Donation after Cardiac Death?,” Am. J. Transplant. Off. J. Am. Soc. Transplant. Am. Soc. Transpl. Surg., **10**(11), pp. 2536–2540.

[99] García-Valdecasas, J. C., 2011, “DCD Donors: A Unique Source to Significantly Increase Organ Donation,” J. Hepatol., **55**(4), pp. 745–746.

[100] Bernat, J. L., D’Alessandro, A. M., Port, F. K., Bleck, T. P., Heard, S. O., Medina, J., Rosenbaum, S. H., Devita, M. A., Gaston, R. S., Merion, R. M., Barr, M. L., Marks, W. H., Nathan, H., O’connor, K., Rudow, D. L., Leichtman, A. B., Schwab, P., Ascher, N. L., Metzger, R. A., Mc Bride, V., Graham, W., Wagner, D., Warren, J., and Delmonico, F. L., 2006, “Report of a National Conference on Donation after Cardiac Death.,” Am. J. Transplant. Off. J. Am. Soc. Transplant. Am. Soc. Transpl. Surg., **6**(2), pp. 281–291.

[101] Ali, A., White, P., Dhital, K., Ryan, M., Tsui, S., and Large, S., 2009, “Cardiac Recovery in a Human Non-Heart-Beating Donor after Extracorporeal Perfusion: Source for Human Heart Donation?,” J. Hear. lung Transplant. Off. Publ. Int. Soc. Hear. Transplant., **28**(3), pp. 290–293.

[102] Noormohamed, M. S., Kanwar, A., Ray, C., Wright, M. C., Cowie, D. E., Stamp, S., Talbot, D., Manas, D., and White, S. A., 2013, “Extracorporeal Membrane Oxygenation for Resuscitation of Deceased Cardiac Donor Livers for Hepatocyte Isolation.,” J. Surg. Res., **183**(2), pp. e39-48.

[103] Tillman, B. W., Chun, Y., Cho, S. K., Chen, Y., Liang, N., Maul, T., Demetris, A., Gu, X., Wagner, W. R., and Tevar, A. D., 2016, “Dual Chamber Stent Prevents Organ Malperfusion in a Model of Donation after Cardiac Death.,” Surgery, **160**(4), pp. 892–901.

[104] Chen, Y., Tillman, B. W., Cho, S. K., Richards, T. D., Tevar, A. D., Gu, X., Wagner, W. R., and Chun, Y., 2017, “A Novel Compartmentalised Stent Graft to Isolate the Perfusion of the Abdominal Organs,” J. Med. Eng. Technol., **41**(2), pp. 141–150.

[105] Wu, W., Qi, M., Liu, X.-P., Yang, D.-Z., and Wang, W.-Q., 2007, “Delivery and Release of Nitinol Stent in Carotid Artery and Their Interactions: A Finite Element Analysis.,” J. Biomech., **40**(13), pp. 3034–3040.

[106] Tillman, B. W., Chun, Y., Cho, S. K., Chen, Y., Liang, N., Maul, T., Demetris, A., Gu, X., Wagner, W. R., and Tevar, A. D., 2016, “Dual Chamber Stent Prevents Organ Malperfusion in a Model of Donation after Cardiac Death,” Surgery, **160**(4), pp. 892–901.

[107] Delong, C., and Sharma, S., 2020, *Physiology, Peripheral Vascular Resistance*, StatPearls Publishing, Treasure Island (FL).